NASA Contractor Report 4377

High Performance, Accelerometer-Based Control of the Mini-MAST Structure at Langley Research Center

Emmanuel G. Collins, Jr., James A. King,
Douglas J. Phillips, and David C. Hyland

CONTRACT NAS1-18872
MAY 1991

NASA Contractor Report 4377

High Performance, Accelerometer-Based Control of the Mini-MAST Structure at Langley Research Center

Emmanuel G. Collins, Jr., James A. King,
Douglas J. Phillips, and David C. Hyland
Harris Corporation
Government Aerospace Systems Division
Melbourne, Florida

Prepared for
Langley Research Center
under Contract NAS1-18872

National Aeronautics and
Space Administration
Office of Management
Scientific and Technical
Information Program
1991

Abstract

Many large space system concepts will require active vibration control to satisfy critical performance requirements such as line-of-sight pointing accuracy and constraints on root-mean-square (rms) surface roughness. In order for these concepts to become operational, it is imperative that the benefits of active vibration control be practically demonstrated in ground-based experiments. This report describes the second experiment conducted by Harris as part of the NASA Controls-Structures Interaction (CSI) Guest Investigator Program under contract NAS1-18872. The results of this experiment demonstrate the successful application of the Maximum Entropy/Optimal Projection control design methodology to active vibration control for a flexible structure. The testbed is the Mini-MAST structure at NASA Langley Research Center and has features dynamically traceable to future space systems. To maximize traceability to real flight systems the controllers were designed and implemented using sensors (four accelerometers and one rate gyro) that are actually mounted to the structure. Ground-mounted displacement sensors that could greatly ease the control design task were available but were used only for performance evaluation. The use of the accelerometers increased the potential of destabilizing the system due to spillover effects and motivated the use of a precompensation strategy to achieve sufficient compensator roll-off.

Table of Contents

List of Tables

List of Figures

1.0 INTRODUCTION

Many future space missions will require active vibration control to satisfy critical performance requirements such as line-of-sight pointing accuracy and constraints on root-mean-square (rms) surface roughness. An important step in the development of this technology is demonstration in ground-based experiments. This report discusses the second experiment conducted by Harris as part of the NASA Controls Structures Interaction (CSI) Guest Investigator Program. This experiment required control design and implementation for the Mini-MAST structure at NASA Langley Research Center and successfully demonstrated active structural control technology. The first experiment involved control design for the ACES structure at NASA Marshall Space Flight Center, Huntsville, AL and is described in [1–2].

The Mini-MAST structure, shown in Figure 1.1, is a beam-like truss structure. As demonstrated in Figure 1.2, this structure can be viewed as the secondary support tower of a precision optical structure. To achieve high accuracy line-of-sight pointing in the optical structure of Figure 1.2 it is important to minimize the relative displacement of the tip of the beam with respect to the base. Hence, the primary objective of this experiment was to design controllers that provide substantial reduction of the displacement of the tip of the Mini-MAST structure. Particular emphasis was also placed on controller simplicity (i.e., reduced-order and decentralized controller architectures). Complexity reduction in control law implementation is of paramount interest due to stringent limitations on throughput of even state-of-the-art space qualified processors.

The primary methodology chosen for control design in this experiment was the Maximum Entropy/Optimal Projection methodology [3–9], a subset of the Optimal Projection Approach for Uncertain Systems (OPUS) [10–11] which allows for the simultaneous trade-off of five fundamental issues in control design: actuator sizing, sensor accuracy, controller order, robustness, and system performance. The Maximum Entropy/Optimal Projection approach was developed particularly to enable the design of high performance, robust control laws for flexible structures. The design equations consist of four coupled matrix equations which specialize to the standard Linear-Quadratic-Gaussian (LQG) Riccati equations when the plant is known perfectly and a full order controller is desired.

To maximize traceability to real flight systems, only the (acceleration and rate) sensors that are mounted on the Mini-MAST structure were used. Five sensors were used: four accelerometers and one rate gyro. Ground-mounted displacement sensors were available but were used only for performance evaluation. Because of the two differentiators in the transfer functions from the control actuators to the accelerometers, the higher frequency modes were much more observable in the accelerometers than in the displacement sensors. Because the performance objective required control of the low frequency modes without destabilizing the higher frequency modes (a standard structural control problem), the use of accelerometers for control design significantly increased the spillover problem. Thus, in this case, it was much more challenging to achieve high performance design using accelerometers rather than displacement sensors.

Because of the use of accelerometers, it was very important to ensure that the control laws rolled off sufficiently to avoid destabilizing the higher frequency modes. In this experiment the roll-off was enforced by using a precompensation strategy. That is, practical roll-off filters were first designed and included as part of the plant. The reduced-order LQG and Maximum Entropy control laws were designed using the modified plant. The roll-off filters were then appended to the reduced-order LQG and Maximum Entropy control laws to obtain the control laws which were actually implemented. As will be seen in the subsequent results, this methodology proved to be very effective for achieving the control design objectives for the Mini-MAST.

The report is organized as follows. Section 2.0 provides a brief description of the Mini-MAST testbed while Section 3.0 describes the Mini-MAST models provided by NASA Langley. Section 4.0 reviews the Maximum Entropy/Optimal Projection approach to control design. Section 5.0 defines the basic control design problem and discusses the precompensation methodology used for control design. Section 6.0 describes the control design strategy used in this experiment and the reduced-order models that were used to develop the control laws. This section also discusses some of the key design details such as the dynamics of the precompensator filters and the weighting schemes that were used. Sections 7.0 and 8.0 describe respectively the decentralized and centralized designs that were implemented and the resultant performance improvement. Finally, Section 9.0 presents closing remarks and conclusions.

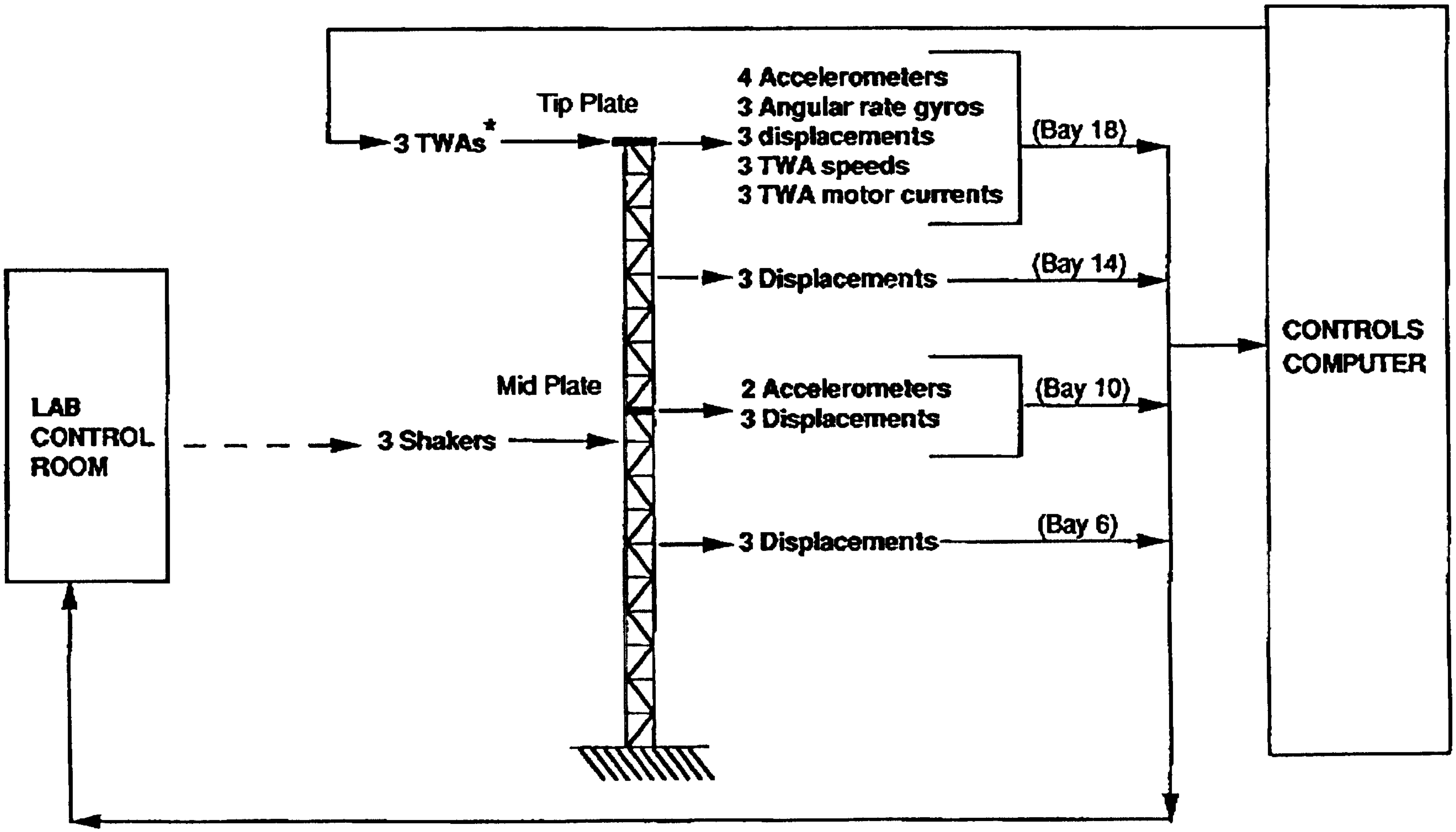

* TORQUE WHEEL ACTUATORS

Figure 1.1 The Mini-MAST Test Article

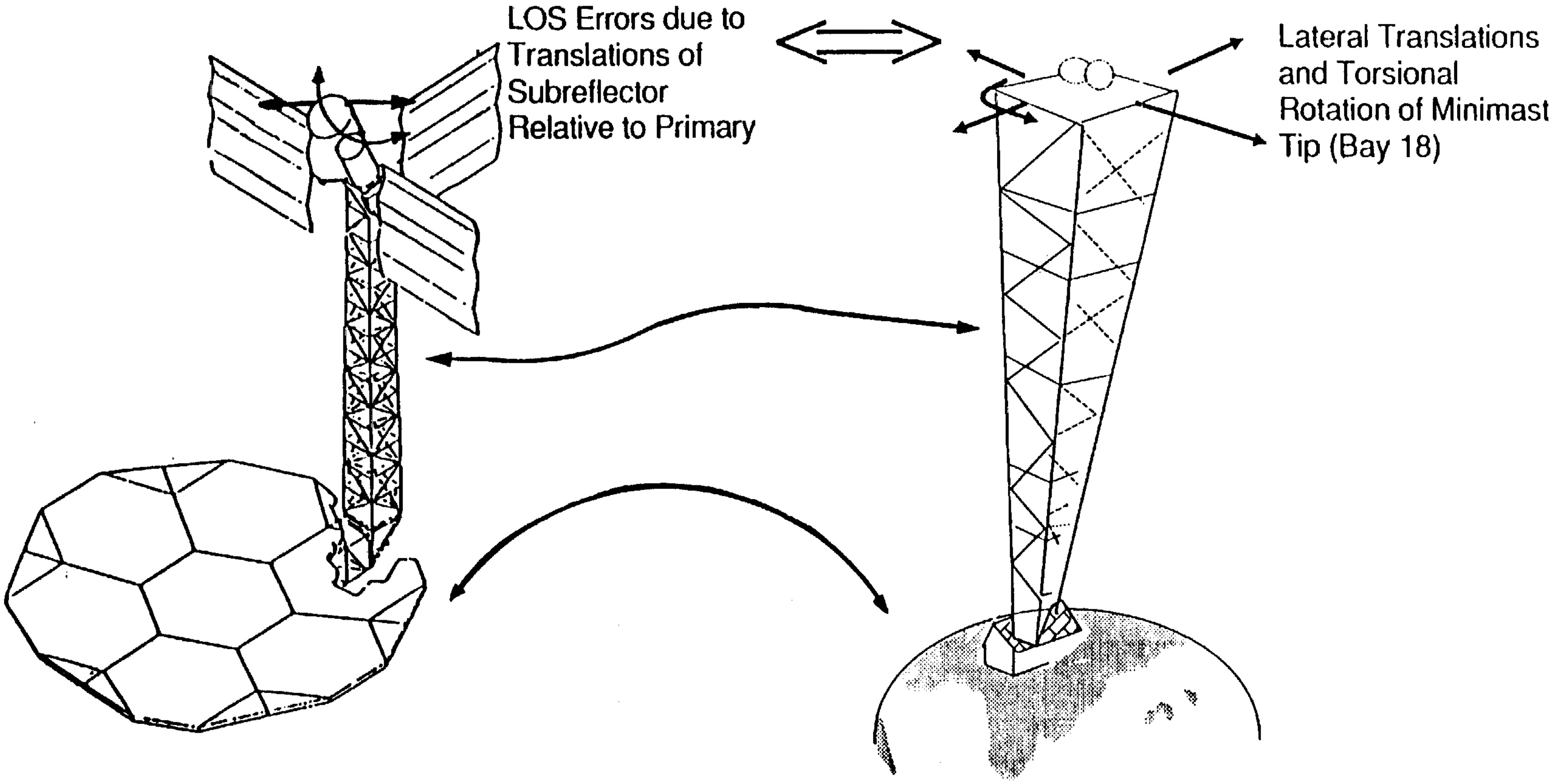

Figure 1.2 The Traceability of the Mini-MAST Structure to Future Space Missions

2.0 DESCRIPTION OF THE MINI-MAST TEST ARTICLE

This section provides a brief description of the Mini-MAST experimental testbed, located at NASA Langley Research Center, Hampton, VA. A more detailed description is provided in [12].

The basic Mini-MAST test article is a generic space truss designed and manufactured by Astro Aerospace Corporation. The tubing members of the truss are made of graphite/epoxy. The truss beam is deployable and retractable and has a triangular cross section. The total height of the truss is 20.16 meters and the truss consists of 18 bays, each of which is 1.12 meters in height.

The actuators and sensors available for control design implementation, disturbance generation, and performance evaluation are shown in Figure 1.1. The only actuators available for control are three torque wheel actuators that are mounted on the tip plate (top of Bay 18) parallel to the global x, y and z reference axes. The torque wheels provide both torsional and bending torque loads to the Mini-MAST. These DC permanent-magnet motors have a rated peak output of 50 ft-lbs at 50 volts and 9.6 amps.

The available control sensors are six Sundstrad QA-1400 servo accelerometers and three Watson angular rate gyros. Four accelerometers are located at the beam tip (Bay 18) and two are located on the mid platform (Bay 10). These sensors measure linear acceleration in the global x and y directions. The three rate sensors are located at the beam tip (Bay 18) and measure pitch (about the x-axis), roll (about the y-axis), and yaw (about the z-axis).

Fifty-one Kaman KD-2300 proximity probes (i.e, displacement sensors) are installed on the support structure along the Mini-MAST. These devices can be used for control but were primarily intended for structural dynamic testing and performance evaluation. In our experimentation used the three Kaman sensors at Bay 18 for performance evaluation. The Kaman sensors at each bay have the orientation shown in Figure 2.1.

Three Unholtz-Dickie 50-lb shakers are attached at Bay 9 for disturbance generation. These shakers are oriented normal to the faces of the truss at each of the three vertices as shown in Figure 2.2.

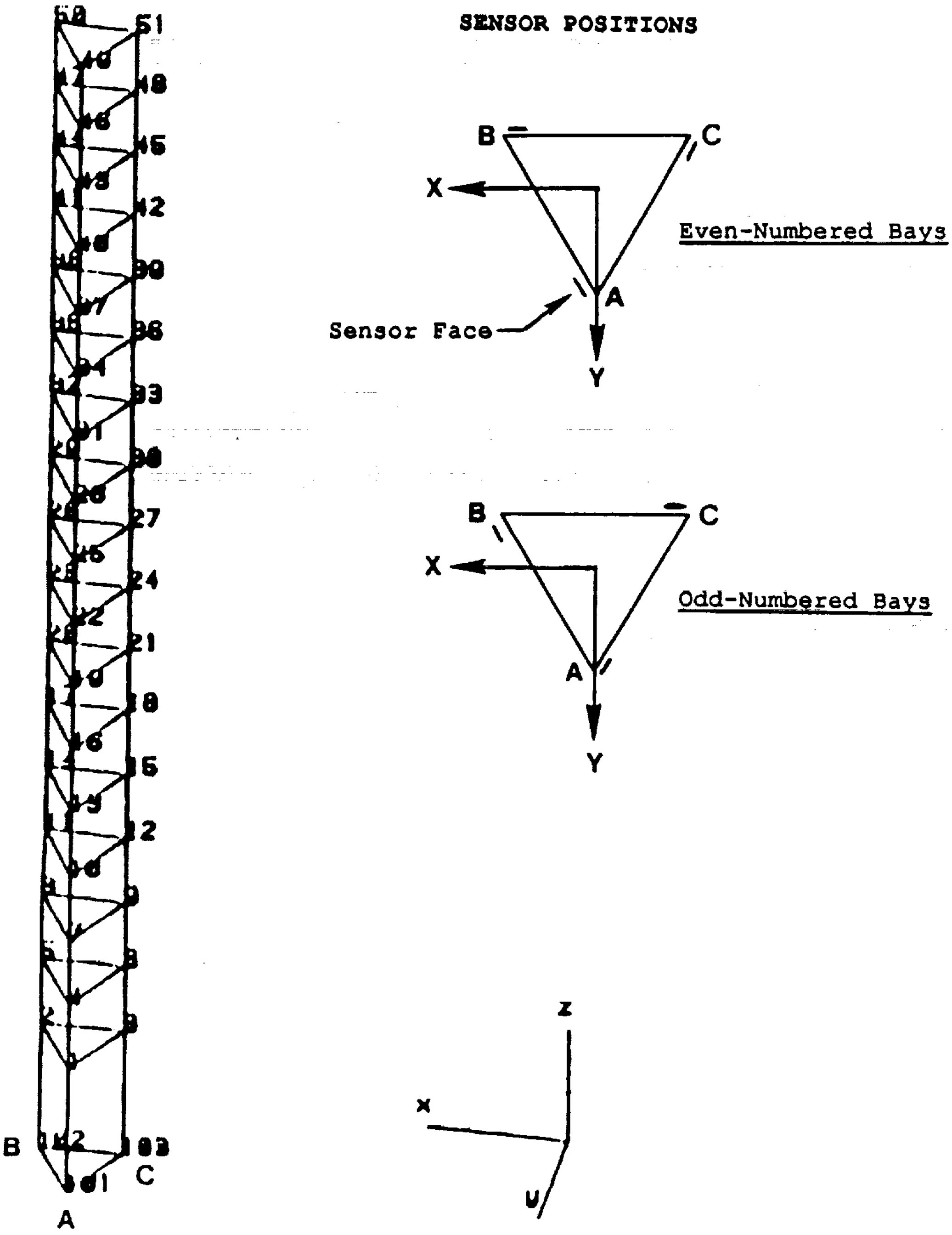

Figure 2.1 The Orientation of the Kaman Displacement Sensors

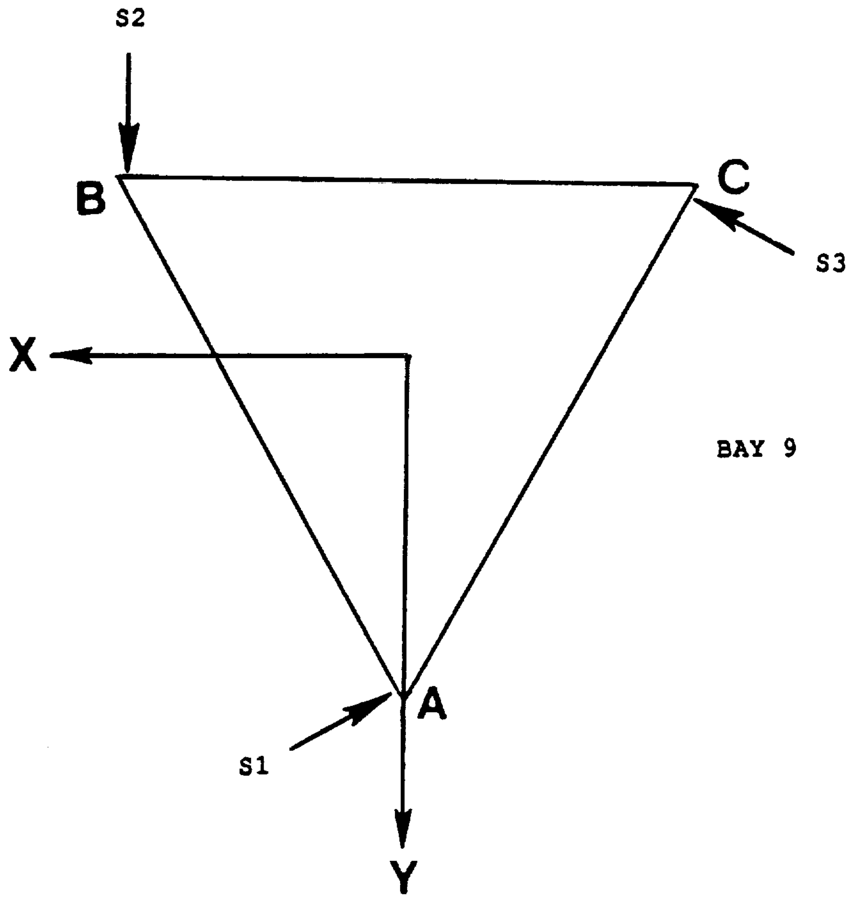

Figure 2.2 The Orientation of the Disturbance Shakers

3.0 DESCRIPTION OF THE MINI-MAST FINITE ELEMENT MODELS

Two models were provided by NASA Langley Research Center. The first model was used to generate the reduced order models that were used to design the decentralized controllers. A second model that had even better correspondence to experimental data was provided later in the program. This model was used to generate the reduced order models that were used to design the centralized controllers. The final evaluation model for each of the control designs was the full-order second model, discretized at 80 Hz, the sample frequency chosen for control law implementation. Delay states were included in the evaluation model to account for the computational delay.

As shown in Figure 3.1, both of the models consisted of essentially three parts: the torque wheel dynamics, the finite element generated structural dynamics, and the 20 Hz analog Bessel filters used to filter the sensor outputs. The 20 Hz Bessel filters were chosen instead of lower frequency Bessel filters to allow better control of the second bending modes which have frequencies of around 6 Hz. The outputs and inputs for both models are listed in Table 3.2. Only Shaker-A was used to disturb the structure and Displacements-A, B and C of Bay 18 were used for performance evaluation. The inputs used for control law implementation were Torque-X, Torque-Y and Torque-Z while the outputs used were Acceleration-1X, Acceleration-2Y, Acceleration-X, Acceleration-Y and Rate Gyro-Z.

3.1 Model 1

For this model the dynamics of the three torque wheels were given as follows.

$$\text{Torque Wheel X:} \quad \frac{\text{Torque}(Nm)}{\text{Input Voltage}} = \frac{34227.1s}{(s+22.8)(s+407.6)}$$

$$\text{Torque Wheel Y:} \quad \frac{\text{Torque}(Nm)}{\text{Input Voltage}} = \frac{38423.8s}{(s+24.3)(s+378.2)}$$

$$\text{Torque Wheel Z:} \quad \frac{\text{Torque}(Nm)}{\text{Input Voltage}} = \frac{34293.0s}{(s+24.6)(s+370.5)}$$

The dynamics of the three torque wheels were quite similar to one another and significantly contributed to the plant dynamics over a wide bandwidth. For example, consider the Bode plots shown in Figure 3.3 of the dynamics of Torque Wheel X. It is seen that these dynamics provide 75° of phase lead at 0.8 Hz, the frequency of the first bending modes, and provide a magnitude variation of over 50 dB from 1 Hz to 100 Hz.

The structural dynamics for this model were composed of 18 modes. The frequency, damping and description of each mode is given in Table 3.5. The dynamics of each of the 20 Hz analog bessel filters were given as follows.

$$\text{20 Hz Bessel Filter:} \quad \frac{\text{Output}}{\text{Input}} = \frac{4.5475 \times 10^{-13}(s^2 + 416.00s + 2.4275 \times 10^{19})}{(s + 208.23)(s^2 + 331.11s + 53012)}$$

NASA Langley was able to obtain good experimental data for the structure above .1 Hz and below 10 Hz. In this frequency regime Model 1 corresponded closely to experimental data. The most significant difference between this model and the actual system appeared to be due to inaccuracies in the dynamics of Torque Wheel X. The generally close correspondence is illustrated by Figures 3.25 and 3.26 which were provided by NASA and compare the frequency responses of Model 1 to the corresponding frequency responses derived directly from experimental data for two of the dominant transfer functions, Torque-X to Acceleration-2Y and Torque-Y to Acceleration-1X.

3.2 Model 2

The dynamics of the three torque wheels for this model differed somewhat from the dynamics provided as part of the first model and are given as follows.

$$\begin{aligned}
\text{Torque Wheel X:} \quad \frac{\text{Torque}(Nm)}{\text{Input Voltage}} &= \frac{34861.3s}{(s + 23.50)(s + 336.90)} \\
\text{Torque Wheel Y:} \quad \frac{\text{Torque}(Nm)}{\text{Input Voltage}} &= \frac{38508.9s}{(s + 23.56)(s + 401.31)} \\
\text{Torque Wheel Z:} \quad \frac{\text{Torque}(Nm)}{\text{Input Voltage}} &= \frac{36433.0s}{(s + 23.44)(s + 372.34)}
\end{aligned}$$

The dynamics of Torque Wheel X differed the most from the corresponding dynamics of the first model. This difference is illustrated by the Bode plot comparison of Figure 3.3 and may be the most significant difference between the first and second models. The close correspondence between the current Torque Wheel X dynamics and experimental data is shown in Figure 3.4, which was provided by NASA.

The structural dynamics for this model were composed of 28 modes. The frequency, damping and description of each mode is given in Table 3.6. The dynamics of the 20 Hz analog Bessel filters were identical to those given previously for the first model.

Figures 3.7 thru 3.24 show the frequency responses of the transfer functions of Model 2 from each of the three torque wheel inputs to each of the five sensor outputs used for control law implementation, as well as those from Shaker-A, used for disturbances, to the three tip displacements used for performance evaluation. Figures 3.8 and 3.12 also show that Model 2 is quite similar to Model 1.

Model 2 corresponded closely to experimental data. The close correspondence is illustrated by Figures 3.27 and 3.28, which were provided by NASA and compare the frequency responses of Model 2 to the corresponding frequency responses derived directly from experimental data for two of the dominant transfer functions, Torque-X to Acceleration-2Y and Torque-Y to Acceleration-1X.

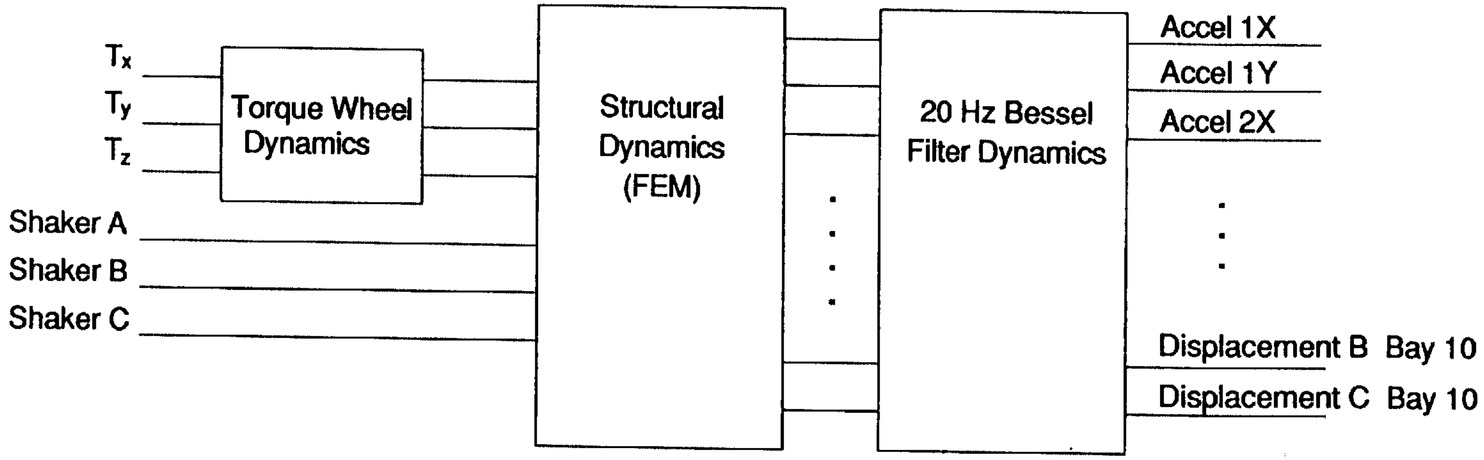

Figure 3.1 The Three Parts of the Provided Models

Inputs				Outputs			
1	Torque (Nm)	X	Bay 18	1	Accelerometer	1X	Bay 18
2	Torque (Nm)	Y	Bay 18	2	Accelerometer	1Y	Bay 18
3	Torque (Nm)	Z	Bay 18	3	Accelerometer	2X	Bay 18
4	Shaker (N)	A	Bay 9	4	Accelerometer	2Y	Bay 18
5	Shaker (N)	B	Bay 9	5	Accelerometer	X	Bay 10
6	Shaker (N)	C	Bay 9	6	Accelerometer	Y	Bay 10
				7	Rate Gyro	X	Bay 18
				8	Rate Gyro	Y	Bay 18
				9	Rate Gyro	Z	Bay 18
				10	Displacement	A	Bay 18
				11	Displacement	B	Bay 18
				12	Displacement	C	Bay 18
				13	Displacement	A	Bay 14
				14	Displacement	B	Bay 14
				15	Displacement	C	Bay 14
				16	Displacement	A	Bay 10
				17	Displacement	B	Bay 10
				18	Displacement	C	Bay 10
				19	Displacement	A	Bay 6
				20	Displacement	B	Bay 6
				21	Displacement	C	Bay 6

Table 3.2 The Outputs and Inputs of the Provided Models

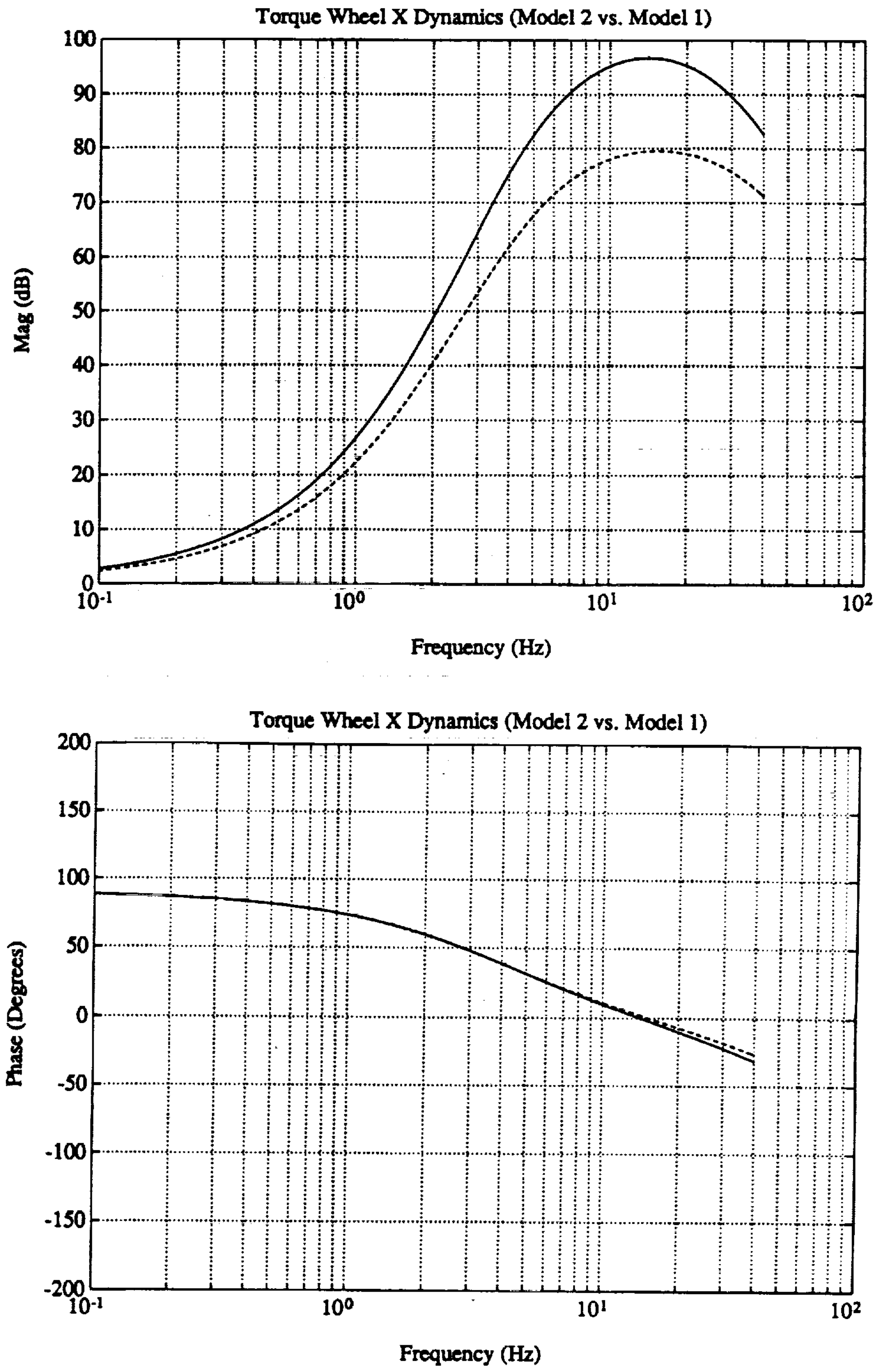
Torque Wheel X Dynamics (Model 2 vs. Model 1)

Torque Wheel X Dynamics (Model 2 vs. Model 1)

Figure 3.3 **Torque Wheel X Frequency Responses for Models 1 and 2 (Model 2 = Solid Line)**

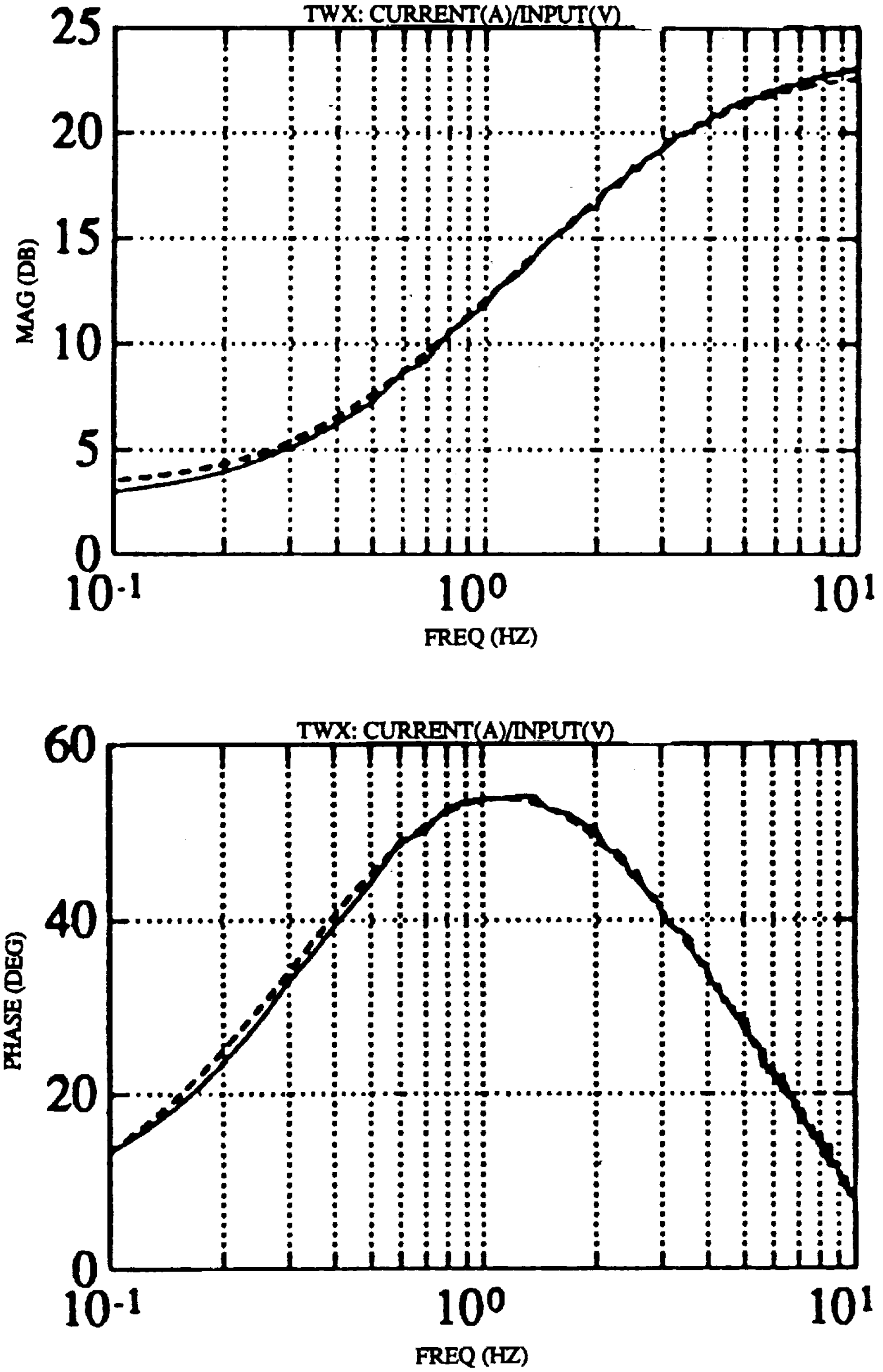

Figure 3.4 Torque Wheel X Frequency Responses: Model 2 vs. Experimental (Model 2 = Solid Line)

Mode Number	Predicted Frequency (Hz)	Predicted Damping	Description
1	.798	.018	1st Y Bending
2	.800	.018	1st X Bending
3	4.37	.012	1st Torsion
4	6.10	.010	2nd Y Bending
5	6.16	.010	2nd X Bending
117	20.3	.005	Tip Plate and Diagonals
118	21.6	.005	2nd Torsion
119	23.5	.005	Tip Plate, Bending and Diagonals
120	28.6	.005	Tip Plate, Bending and Diagonals
121	30.7	.005	3rd Y Bending
122	32.1	.005	3rd X Bending
123	37.3	.005	Mid Plate
124	38.3	.005	Mid Plate and Cable
127	39.0	.005	3rd Torsion
128	42.2	.005	4th Y Bending
129	44.9	.005	4th X Bending
130	54.3	.005	4th Torsion
131	56.1	.005	Tip Plate, Cable and Torsion

Table 3.5 The Structural Modes of Model 1

Mode Number	Predicted Frequency (Hz)	Predicted Damping	Description
1	0.83	.018	1st Y Bending
2	0.83	.018	1st X Bending
3	4.37	.012	1st Torsion
4	6.38	.010	2nd Y Bending
5	6.44	.010	2nd X Bending
6	14.72	.005	Tip Plate
7	14.83	.005	Diagonal
8	15.42	.005	1st Axial
9	15.57	.005	Tip Plate
10	15.60	.005	Tip Plate
33	17.17	.005	Diagonal
117	20.29	.005	Tip Plate
118	21.80	.005	Second Torsion
119	23.75	.005	Both Plates
120	25.83	.005	Both Plates
121	31.62	.005	3rd Y Bending
122	33.10	.005	3rd X Bending
123	39.14	.005	3rd Torsion
126	42.46	.005	4th Y Bending
127	45.95	.005	4th X Bending
128	54.14	.005	Tip Plate
129	57.25	.005	4th Torsion
132	60.85	.005	Mid Plate
133	62.68	.005	Tip Plate
134	66.04	.005	Tip Plate
135	72.18	.005	5th Y Bending
136	72.37	.005	5th X Bending
137	73.34	.005	5th Torsion

Table 3.6 The Structural Modes of Model 2

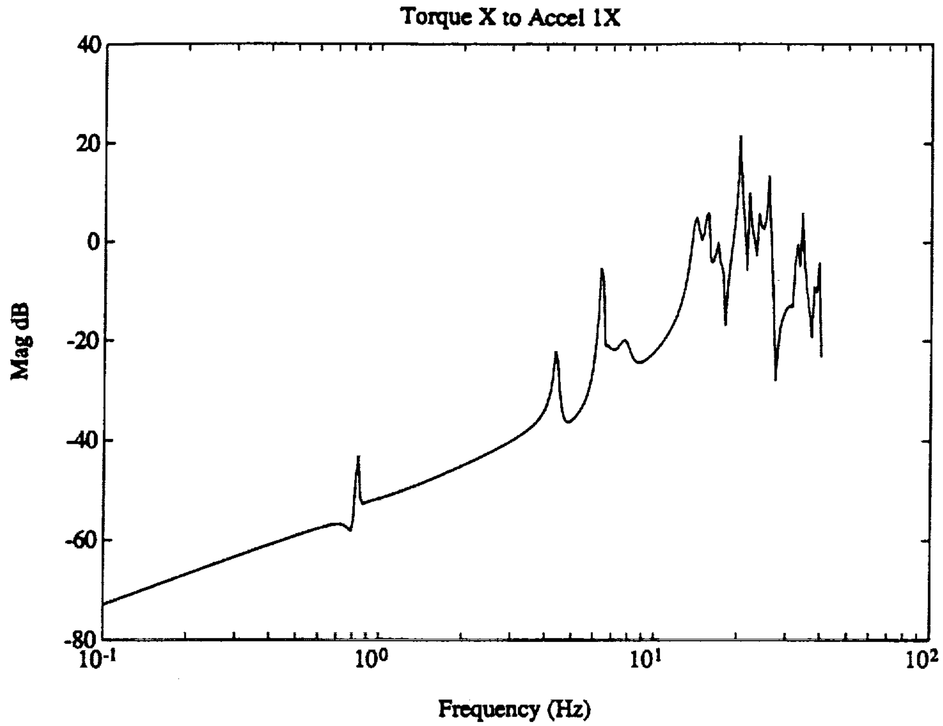

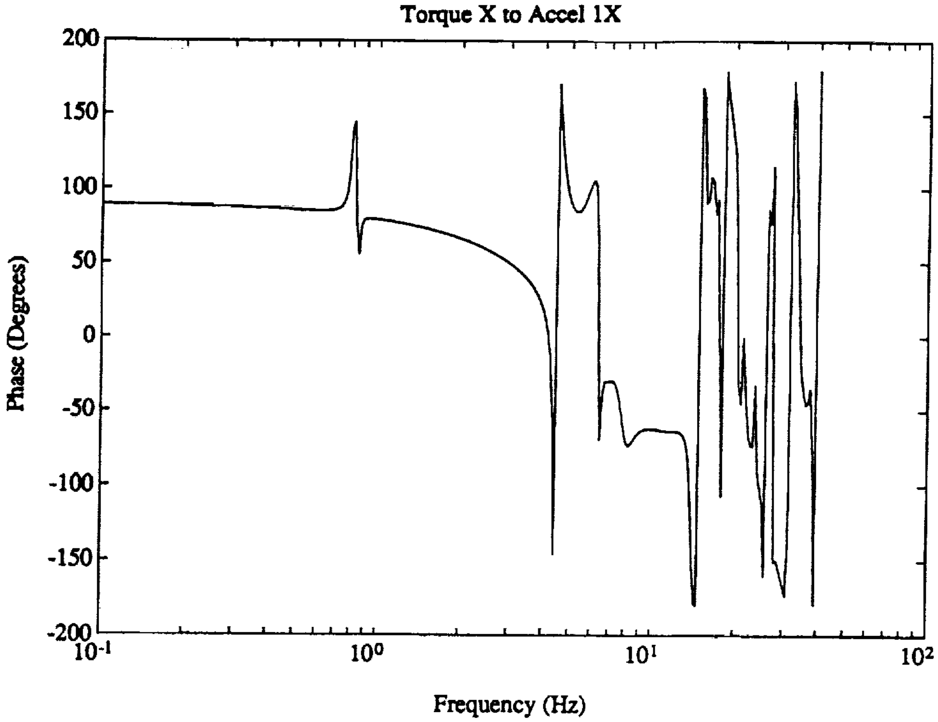

Figure 3.7 Bode Plots of Torque-X to Acceleration-1X for Model 2

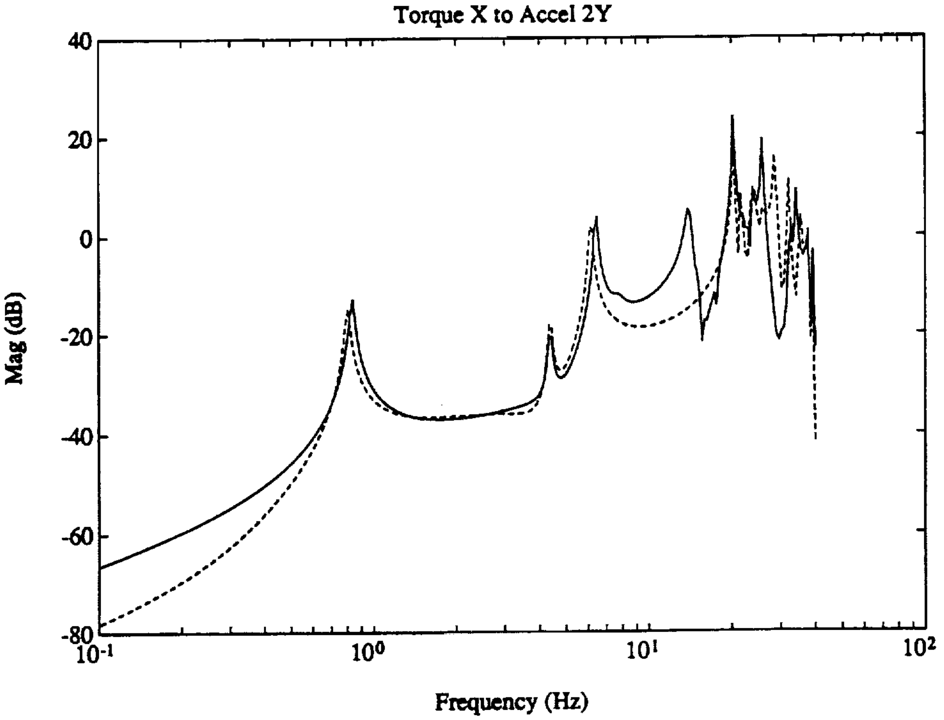

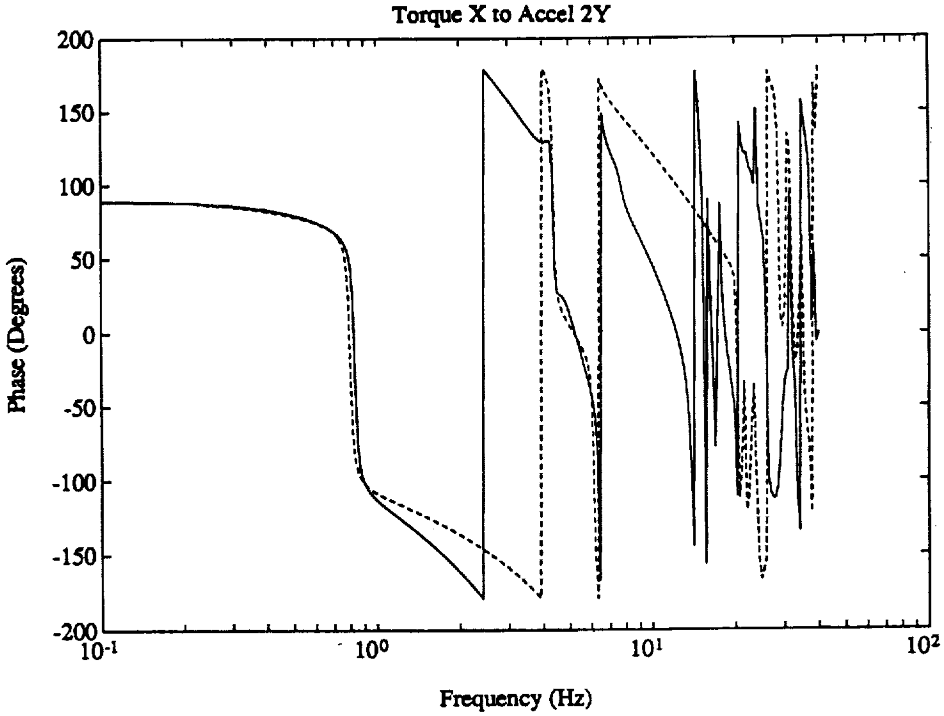

Figure 3.8 **Bode Plots of Torque-X to Acceleration-2Y for Models 1 and 2 (Model 2 = Solid, Model 1 = Dashed)**

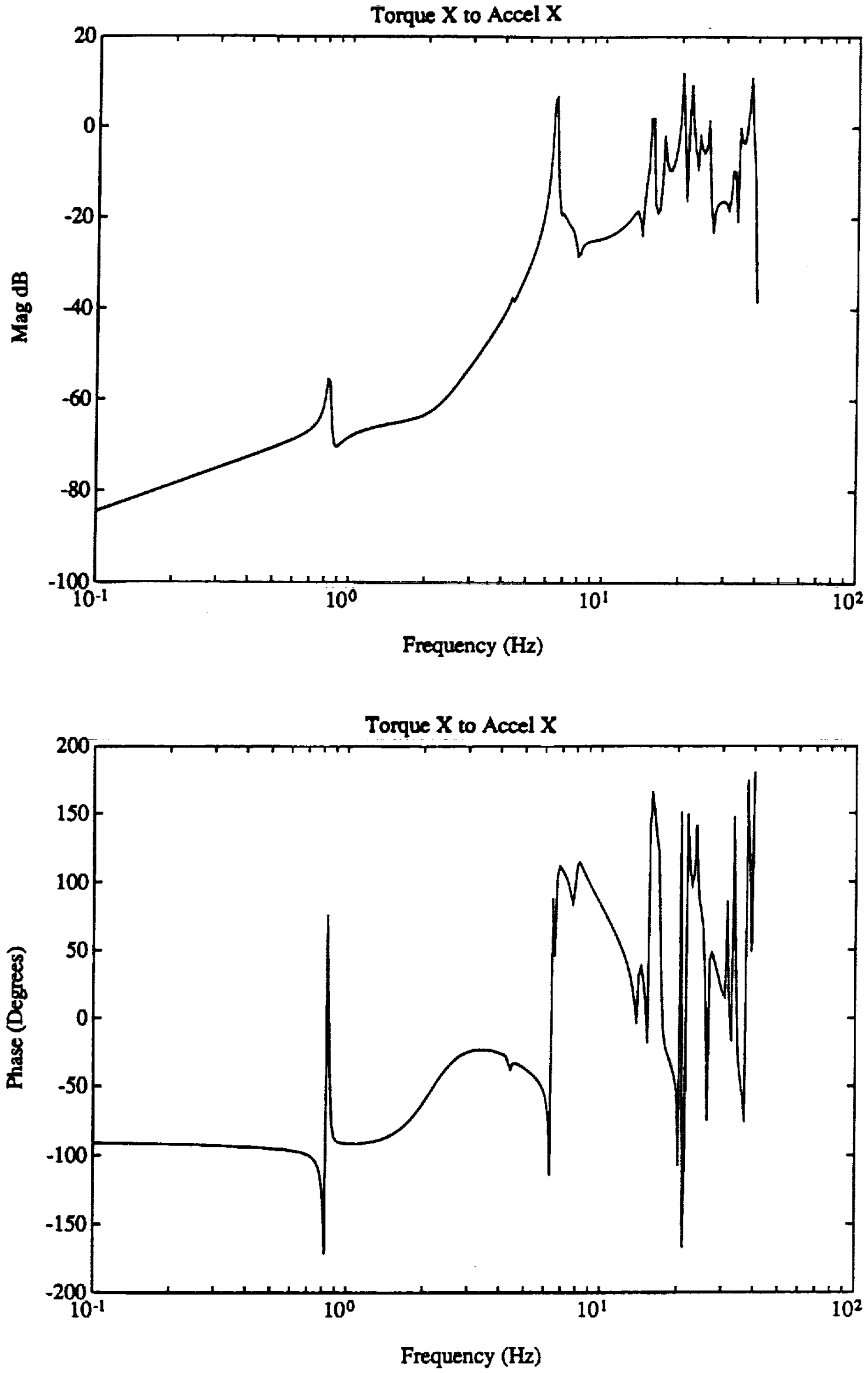

Figure 3.9 Bode Plots of Torque-X to Acceleration-X for Model 2

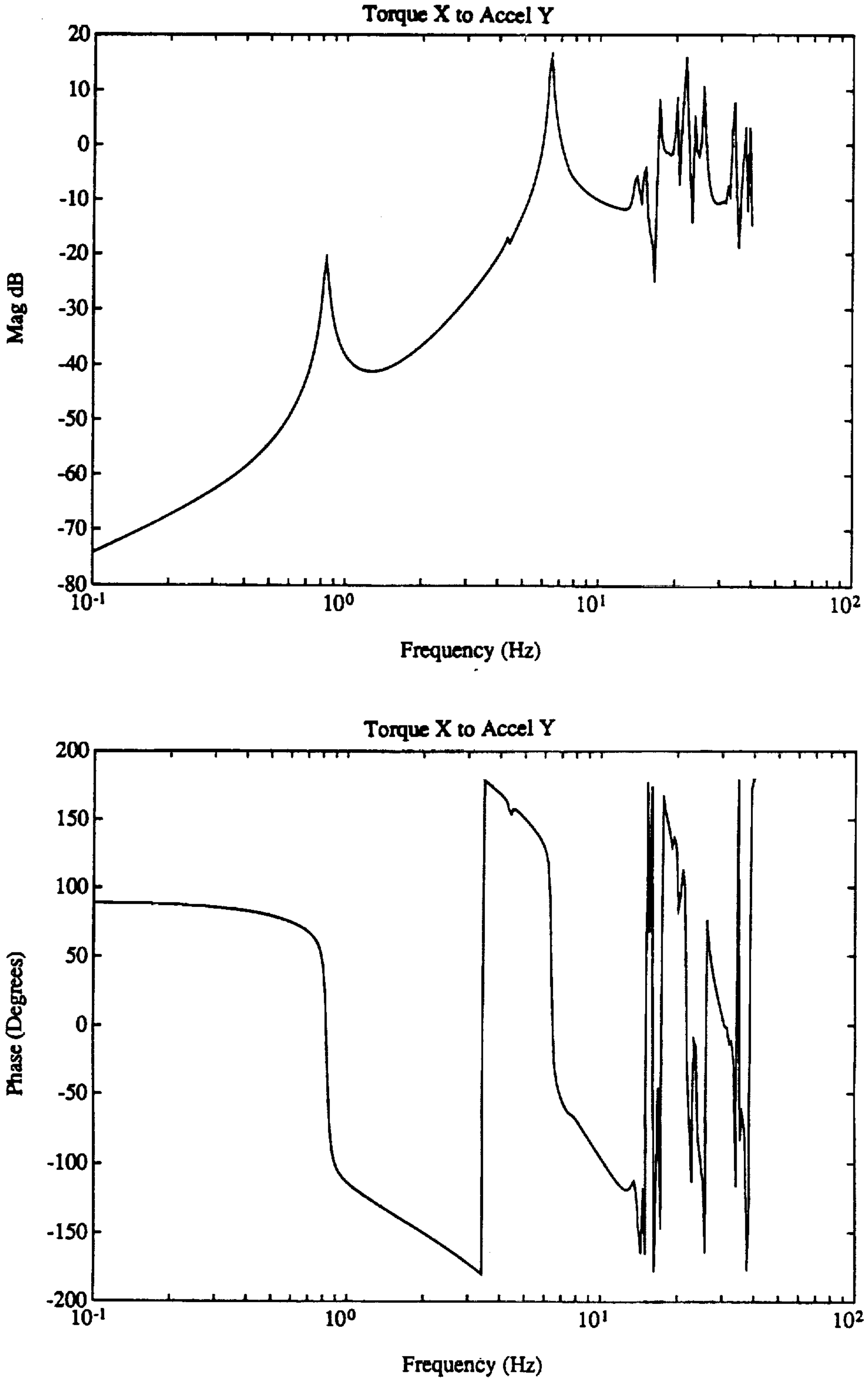

Figure 3.10 Bode Plots of Torque-X to Acceleration-Y for Model 2

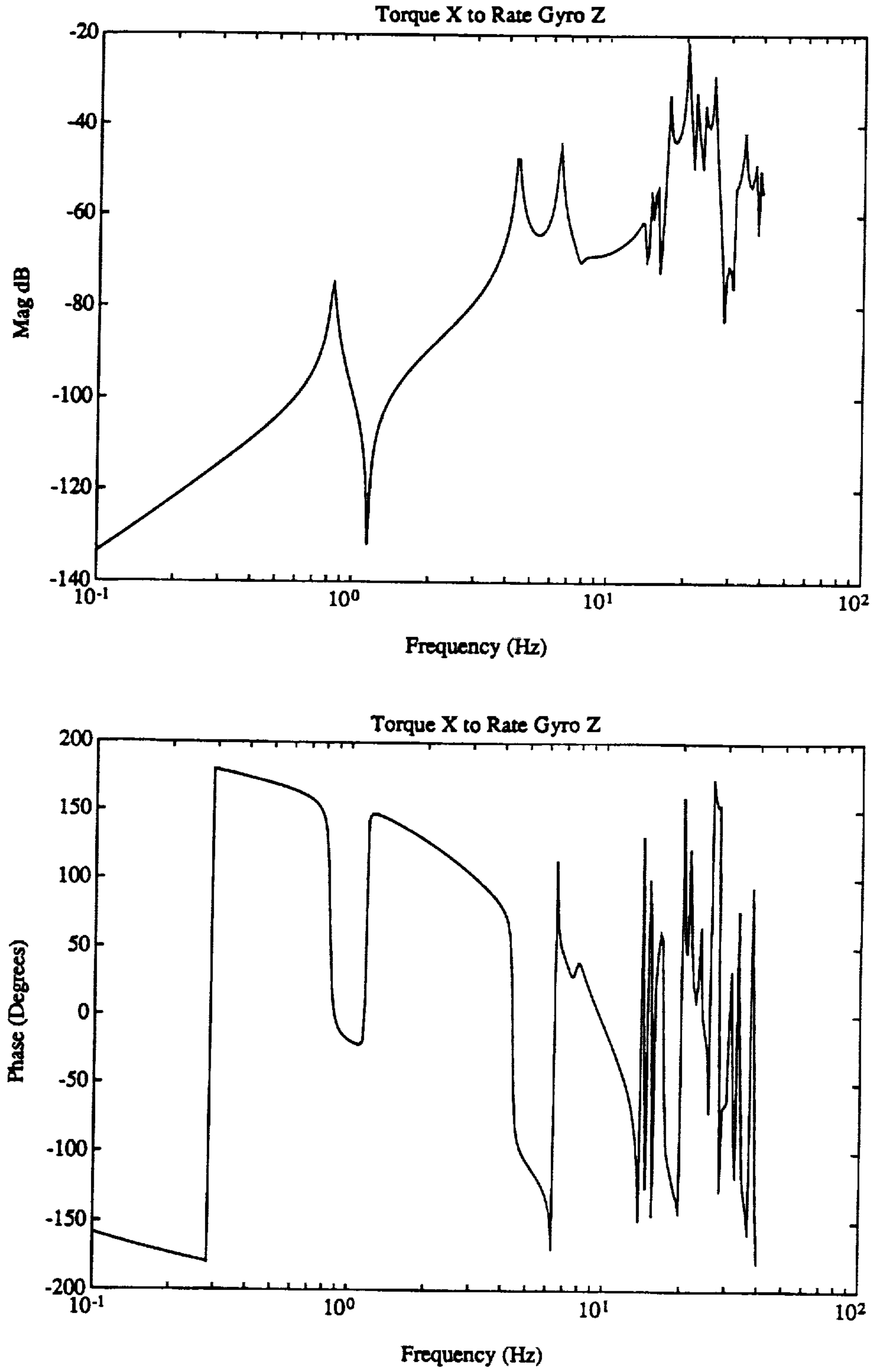

Figure 3.11 Bode Plots of Torque-X to Rate Gyro-Z for Model 2

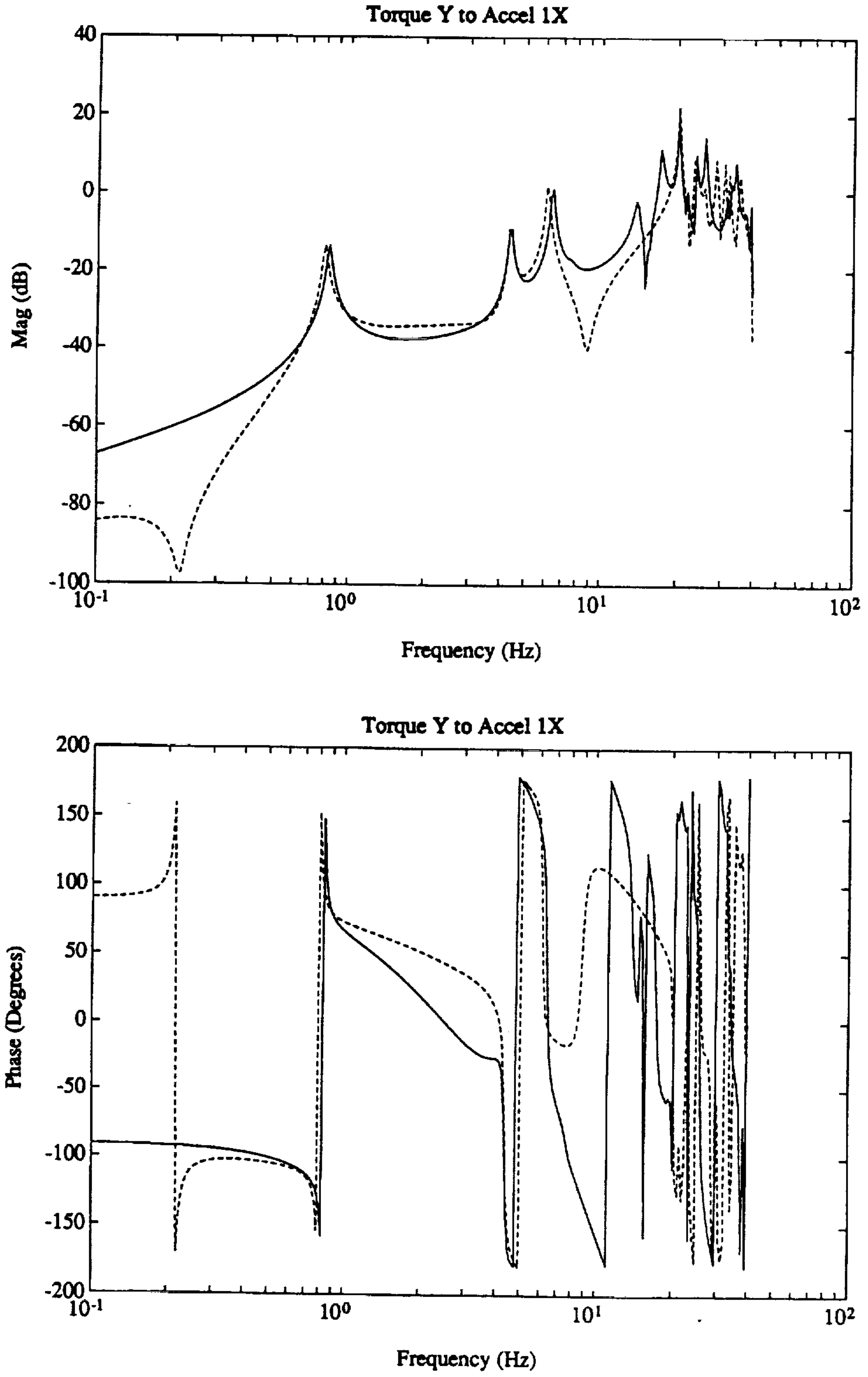

Figure 3.12 Bode Plots of Torque-Y to Acceleration-1X for Models 1 and 2 (Model 2 = Solid, Model 1 = Dashed)

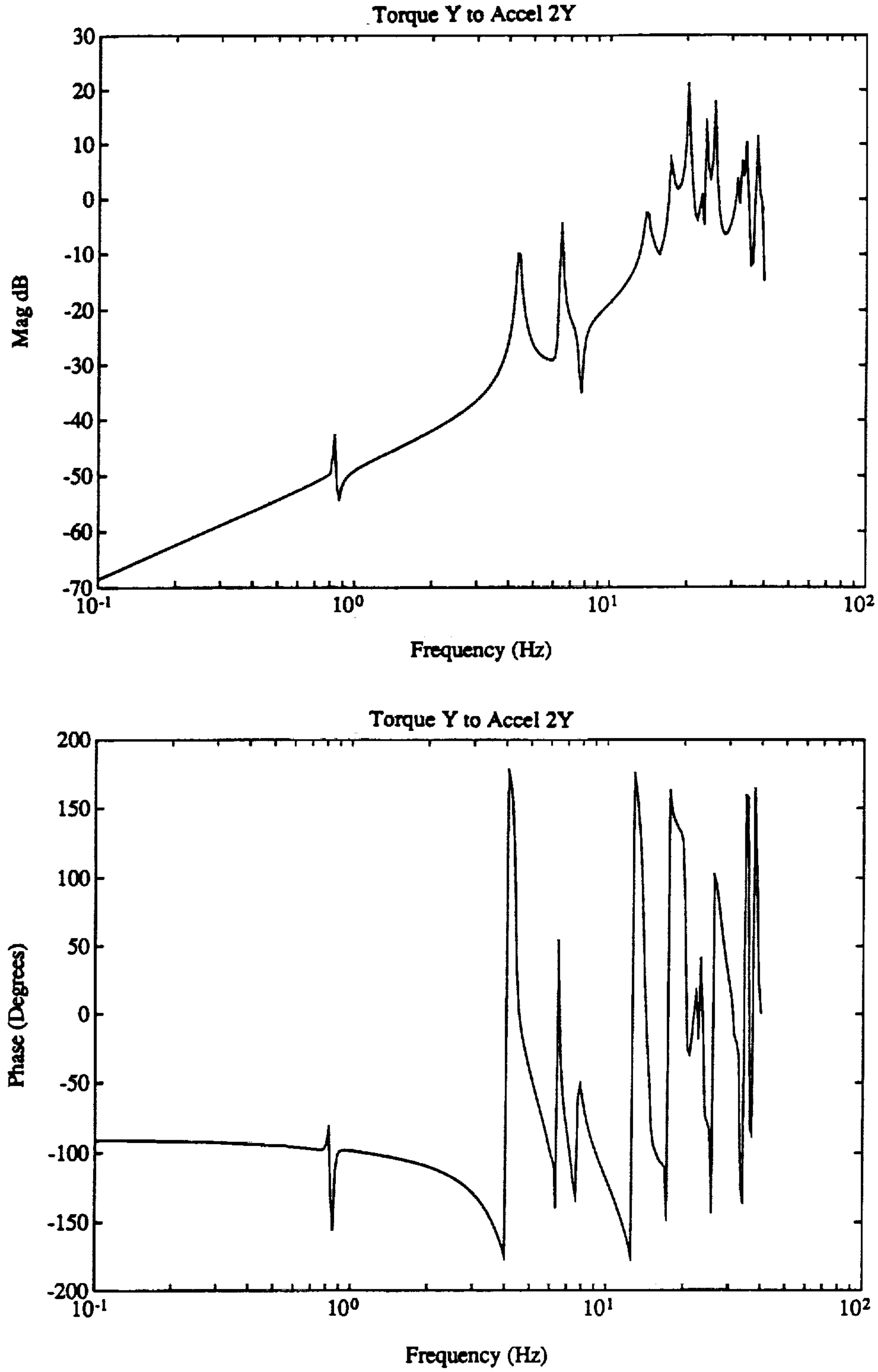

Figure 3.13 Bode Plots of Torque-Y to Acceleration-2Y for Model 2

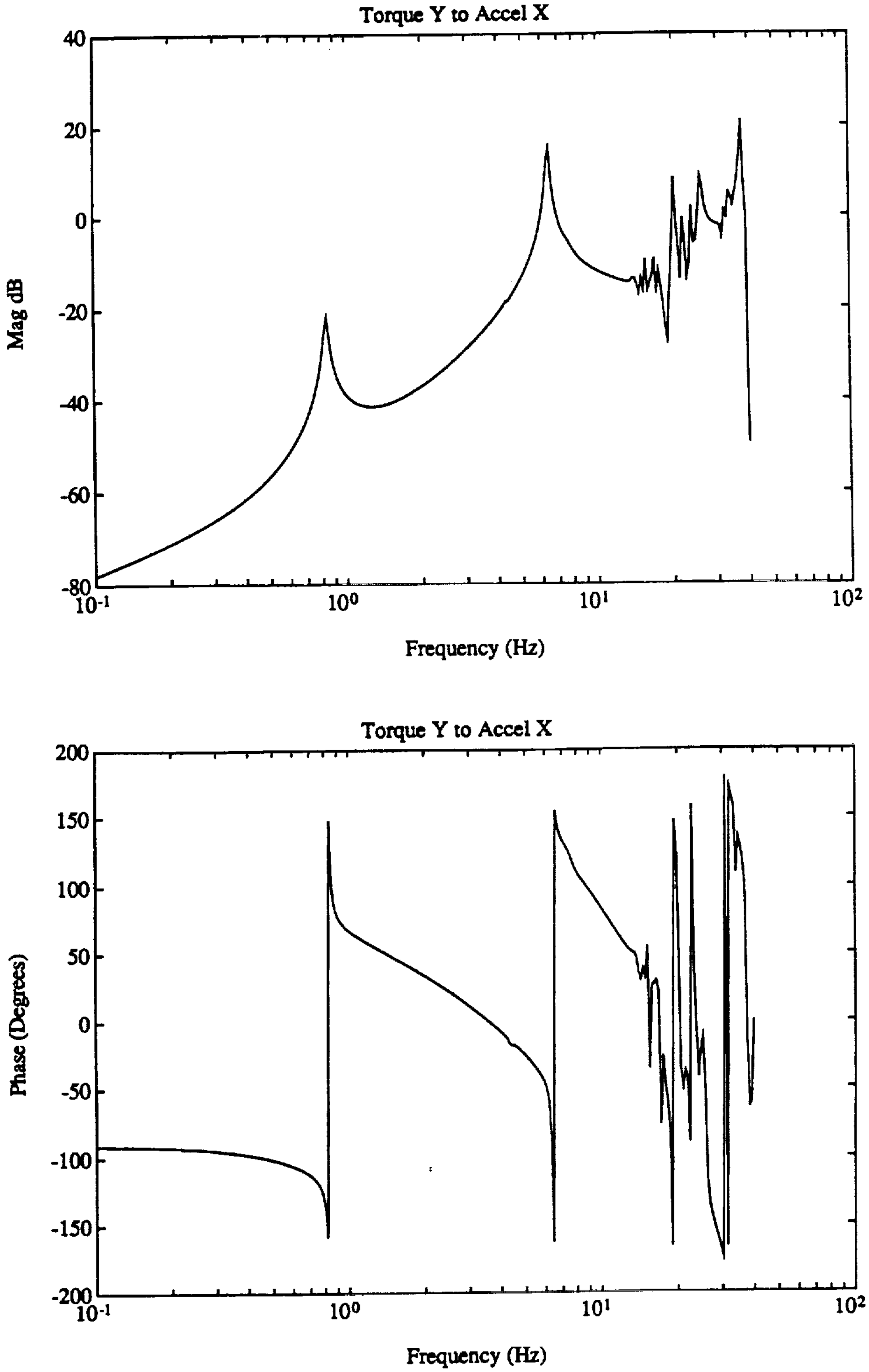

Figure 3.14 Bode Plots of Torque-Y to Acceleration-X for Model 2

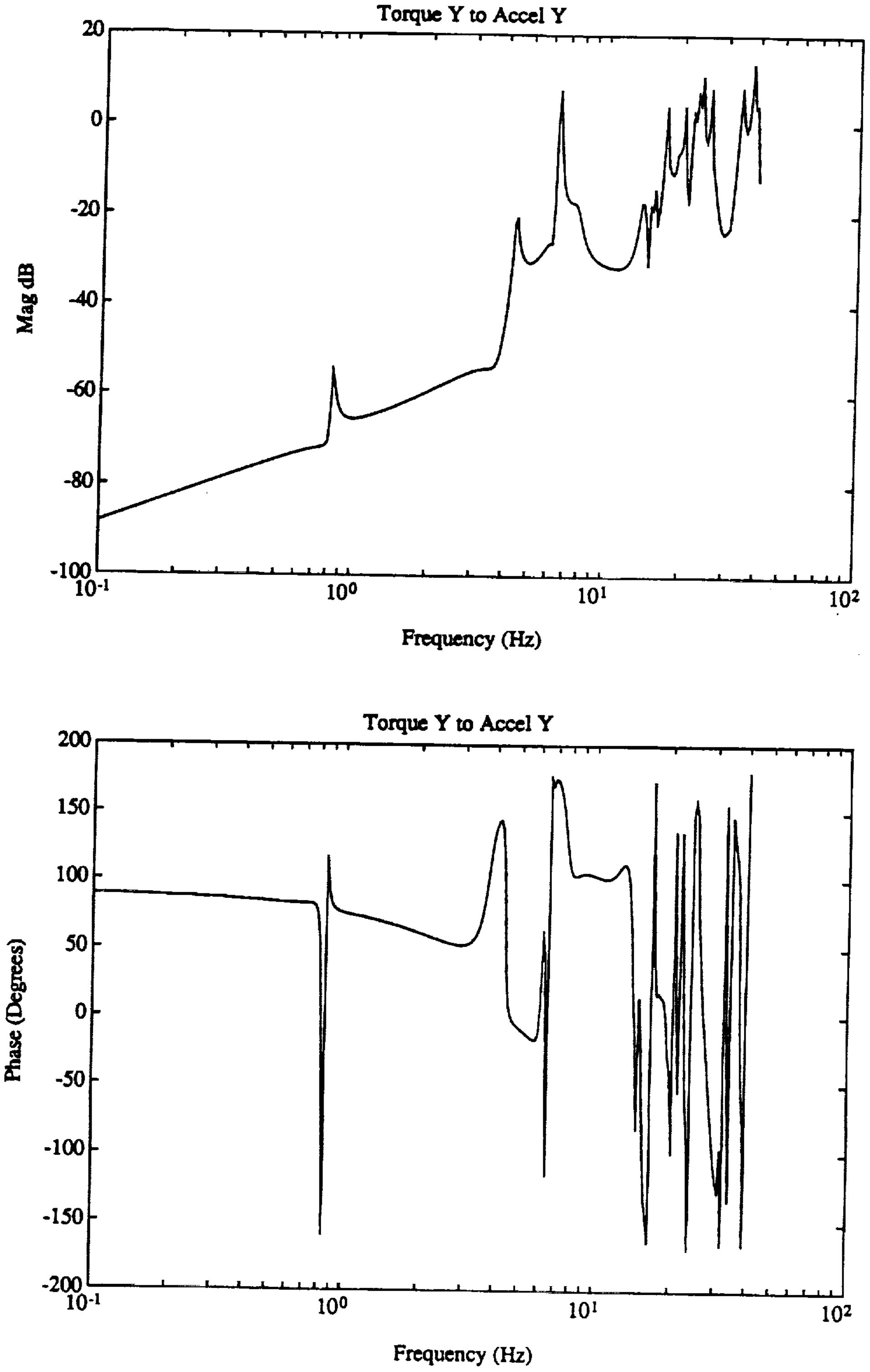

Figure 3.15 Bode Plots of Torque-Y to Acceleration-Y for Model 2

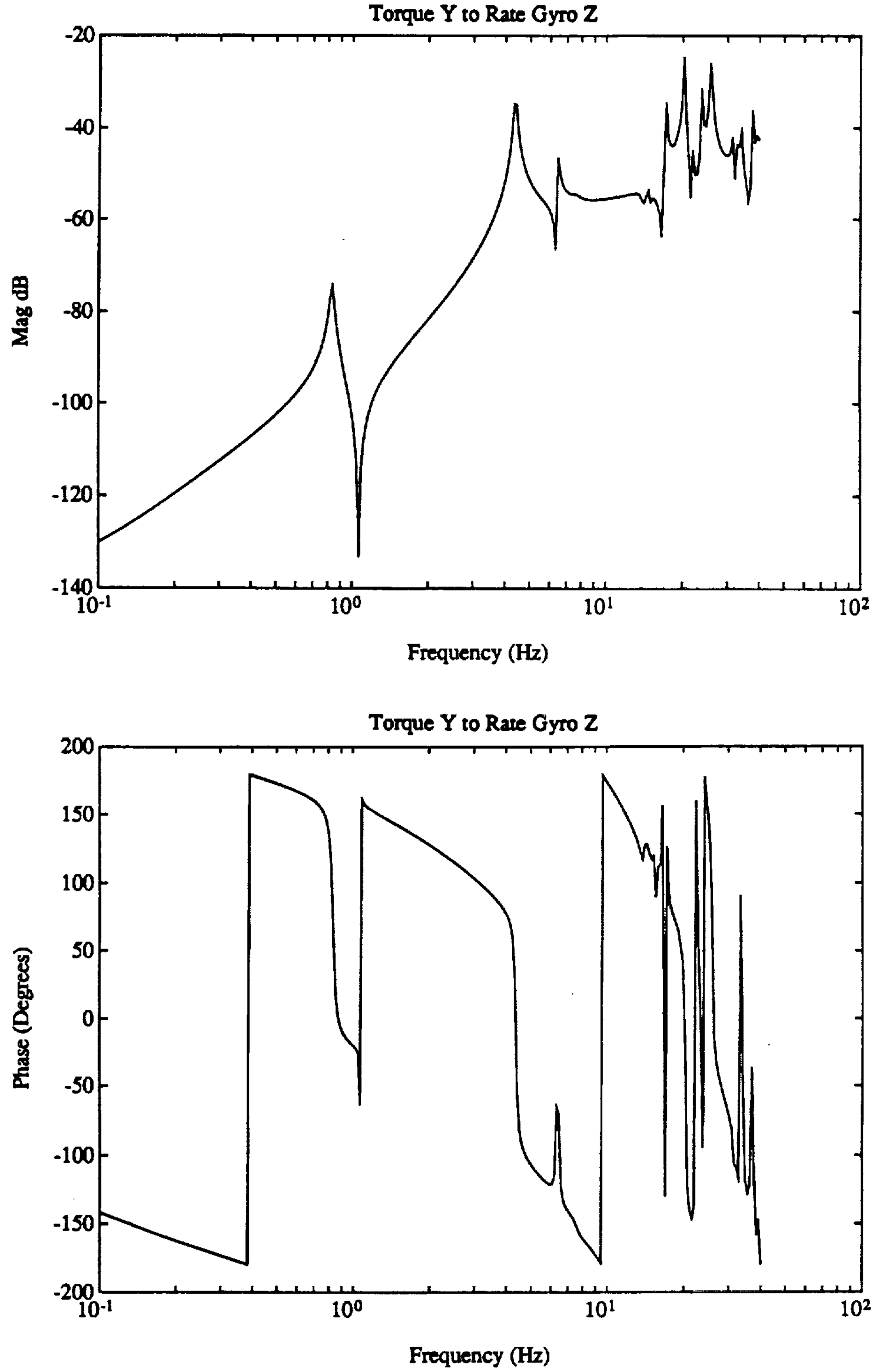

Figure 3.16 Bode Plots of Torque-Y to Rate Gyro-Z for Model 2

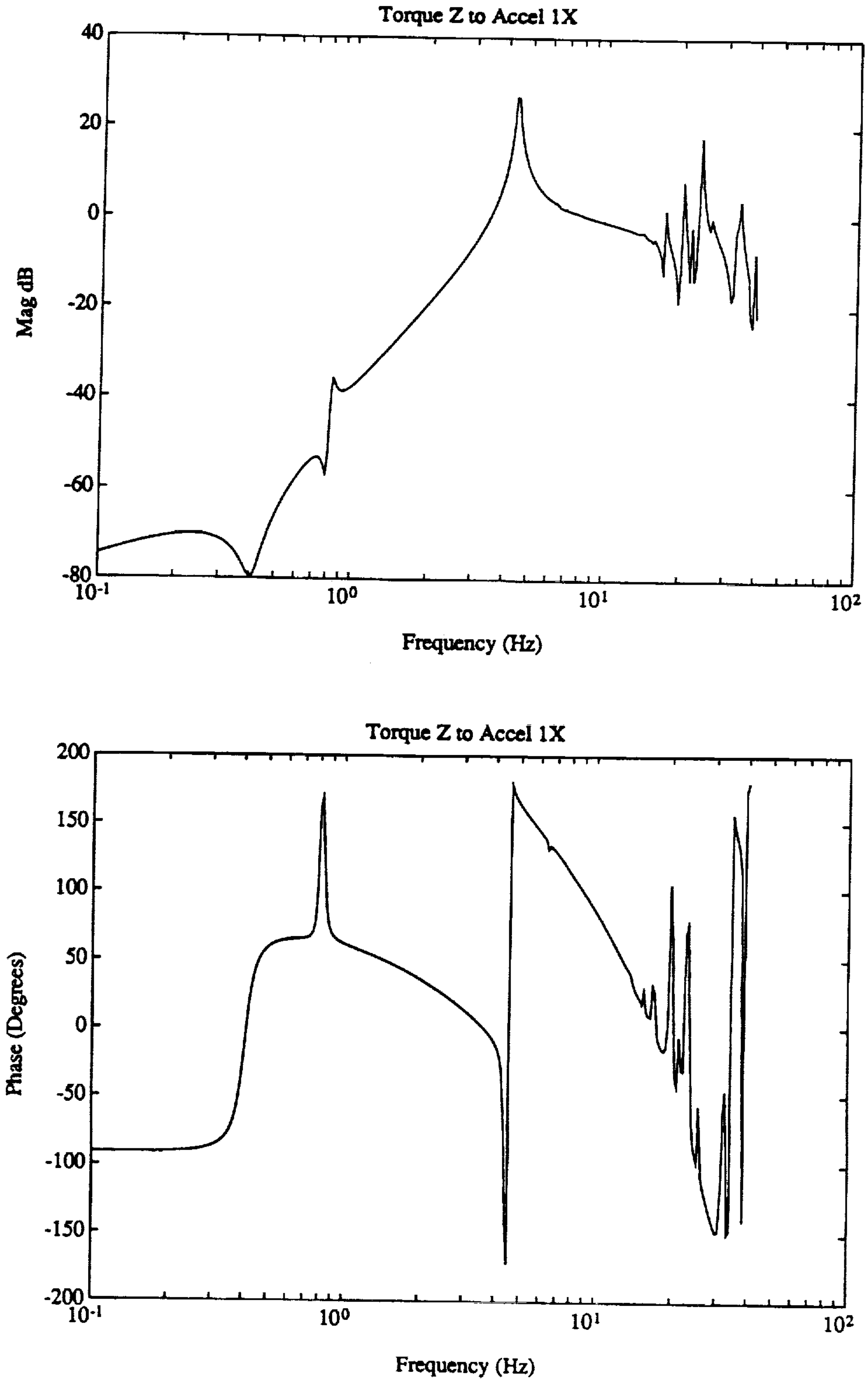

Figure 3.17 Bode Plots of Torque-Z to Acceleration-1X for Model 2

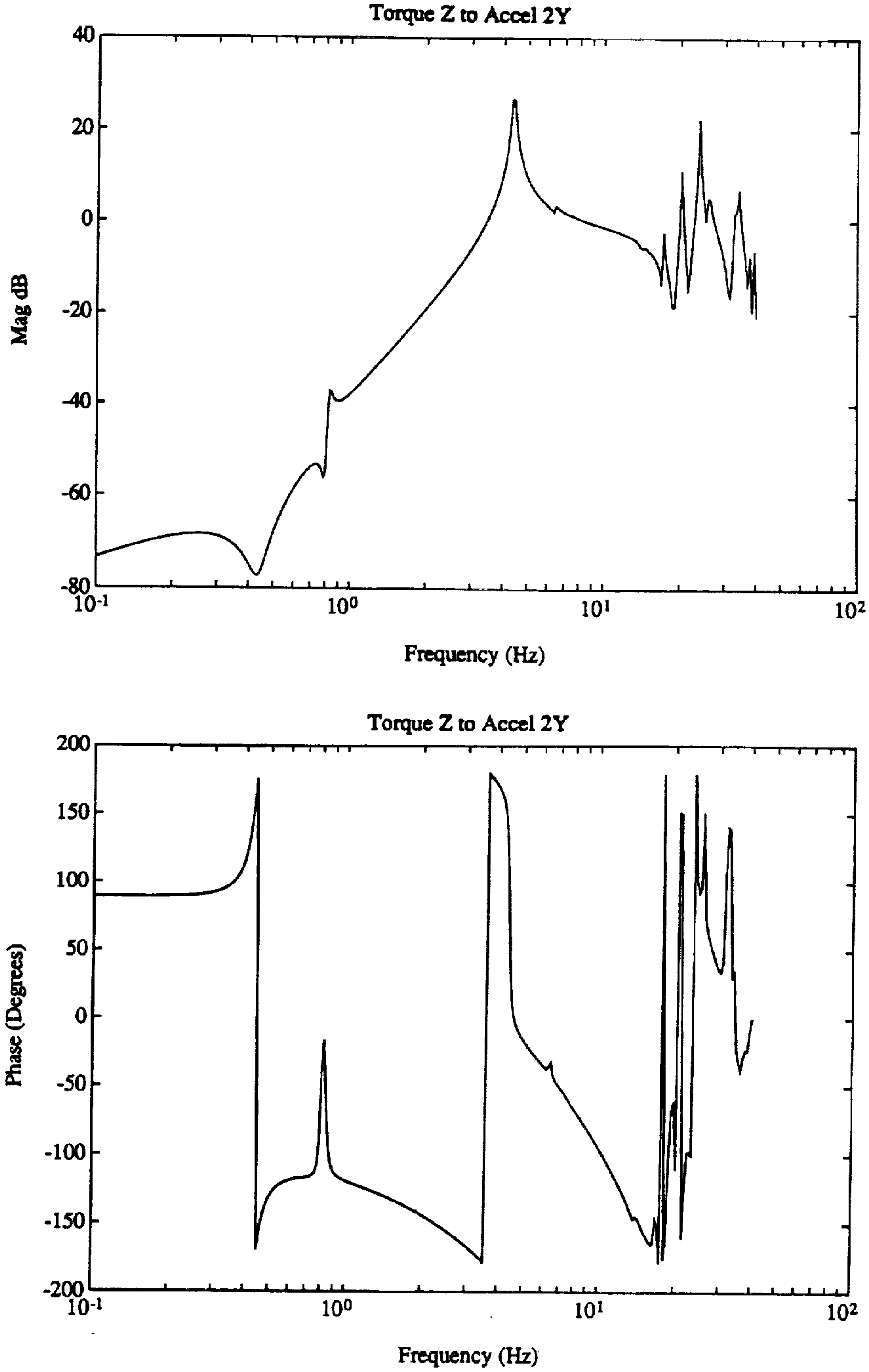

Figure 3.18 Bode Plots of Torque-Z to Acceleration-2Y for Model 2

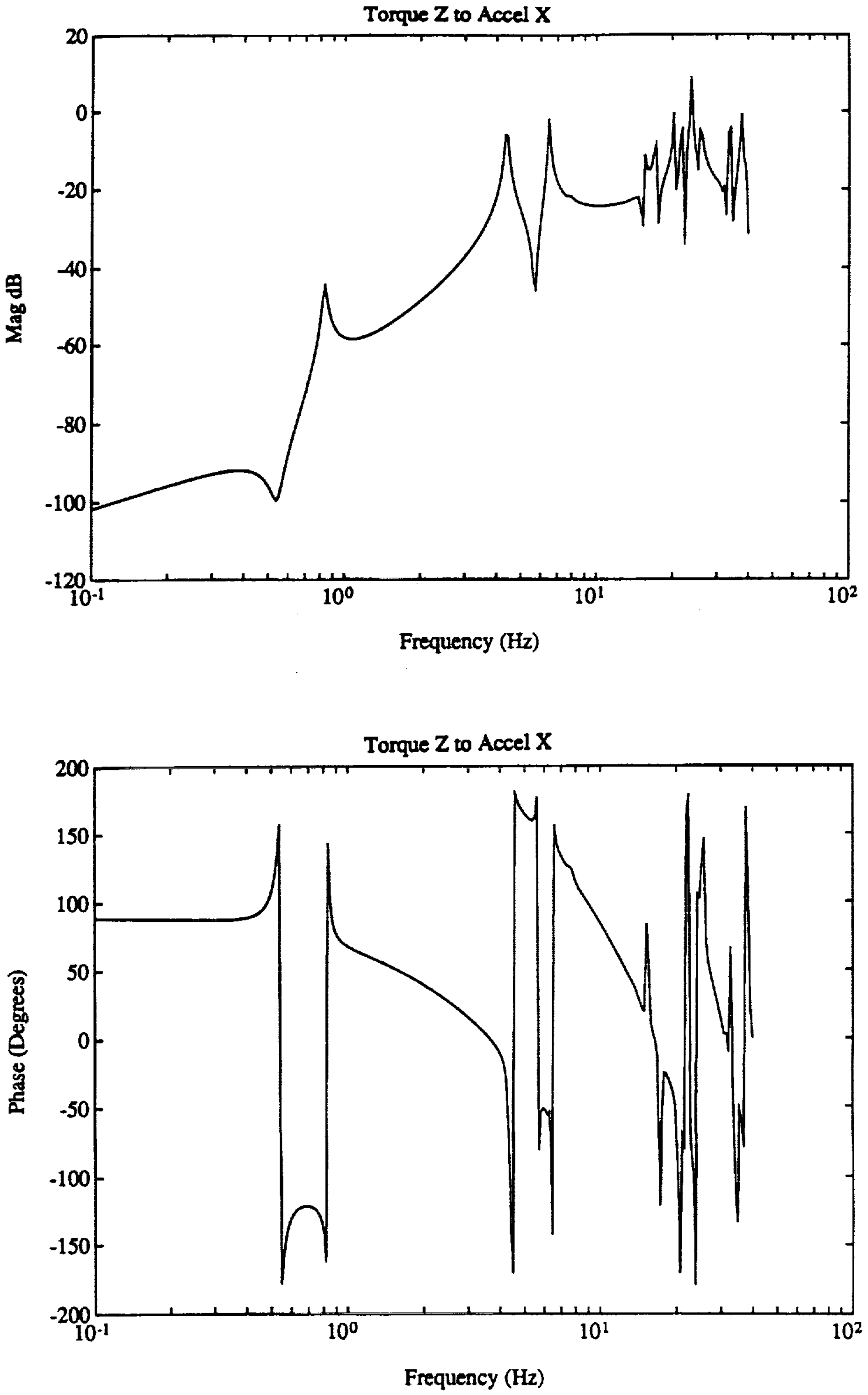

Figure 3.19 Bode Plots of Torque-Z to Acceleration-X for Model 2

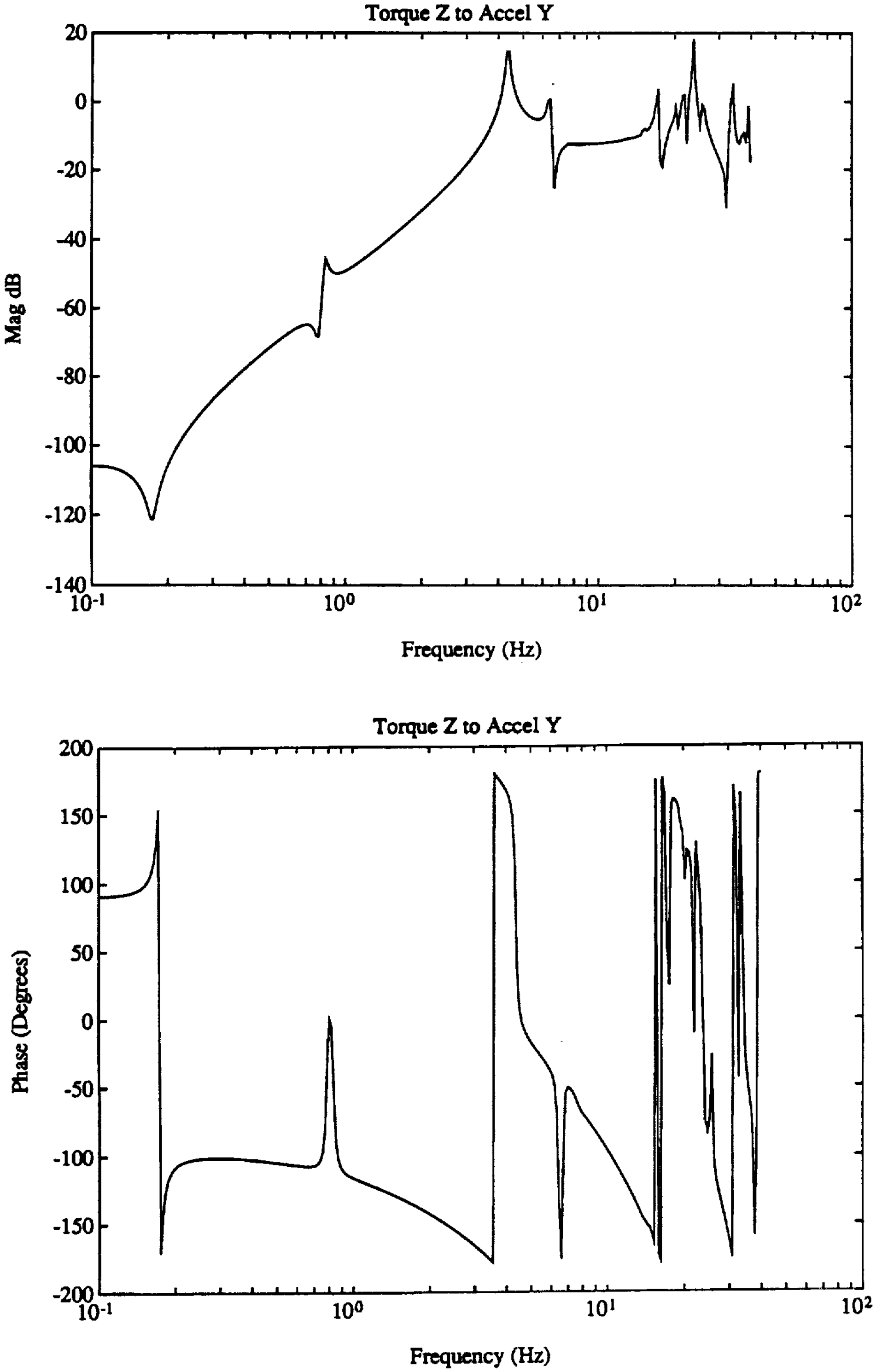

Figure 3.20 Bode Plots of Torque-Z to Acceleration-Y for Model 2

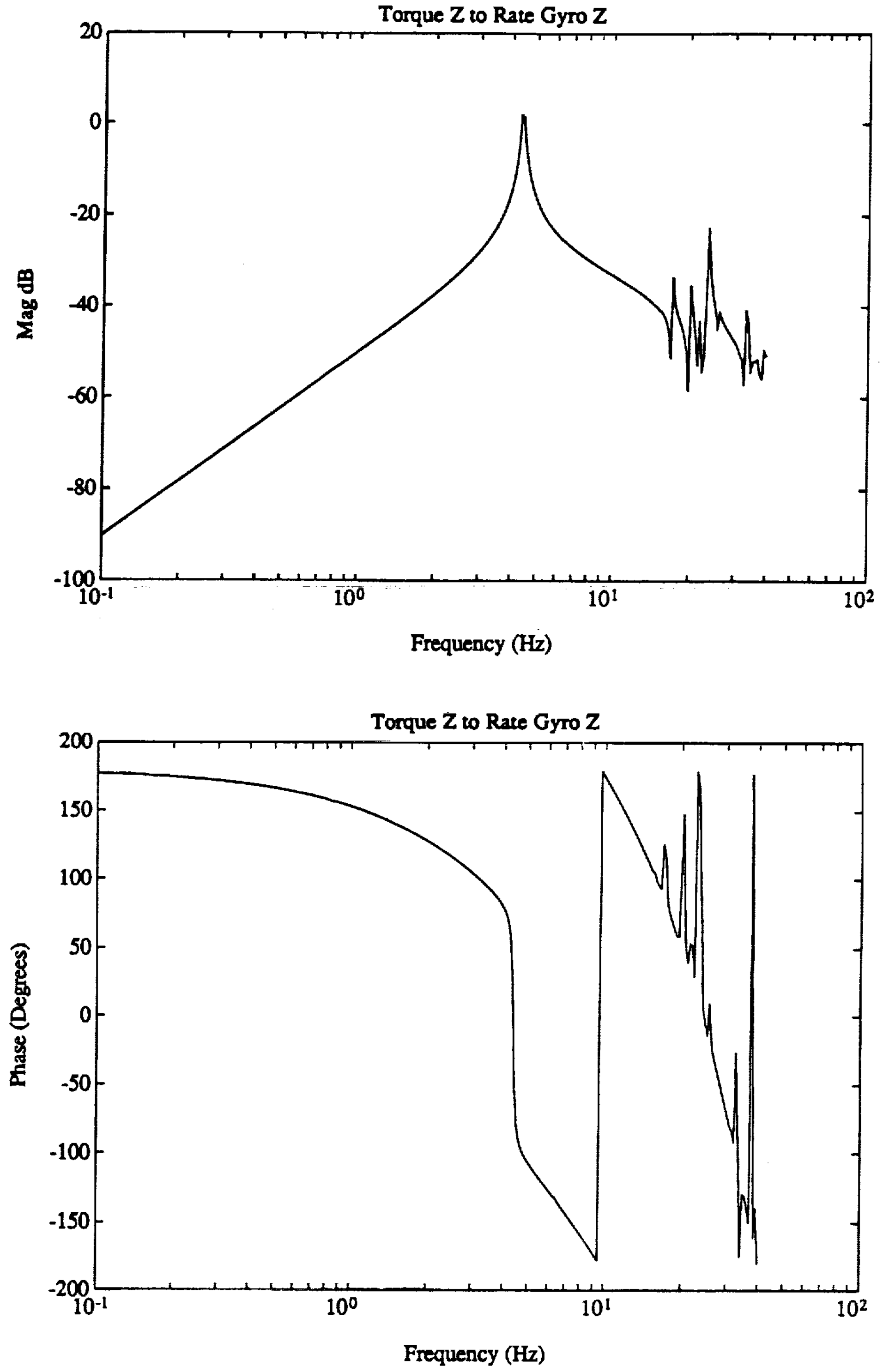

Figure 3.21 Bode Plots of Torque-Z to Rate Gyro-Z for Model 2

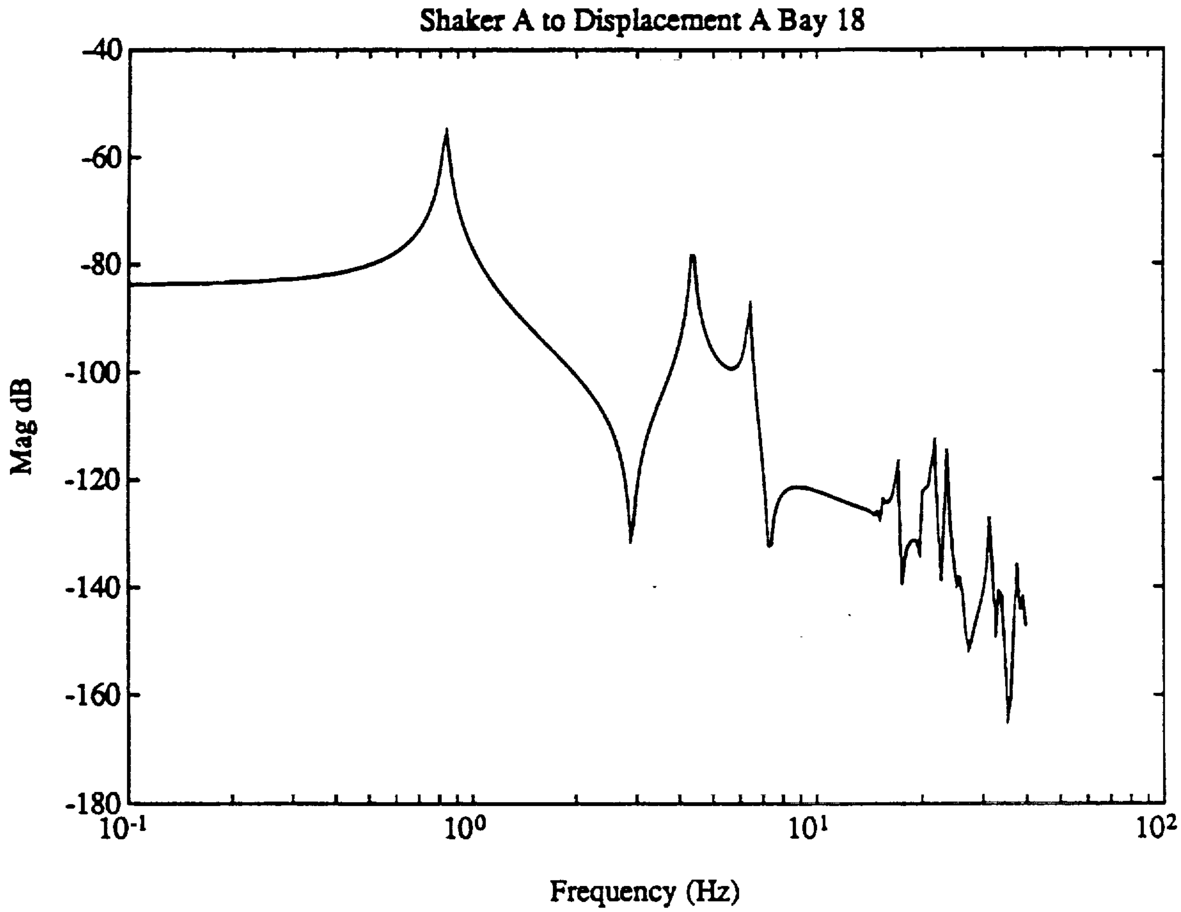

Figure 3.22 Bode Magnitude Plot of Shaker-A to Displacement-A of Bay 18 for Model 2

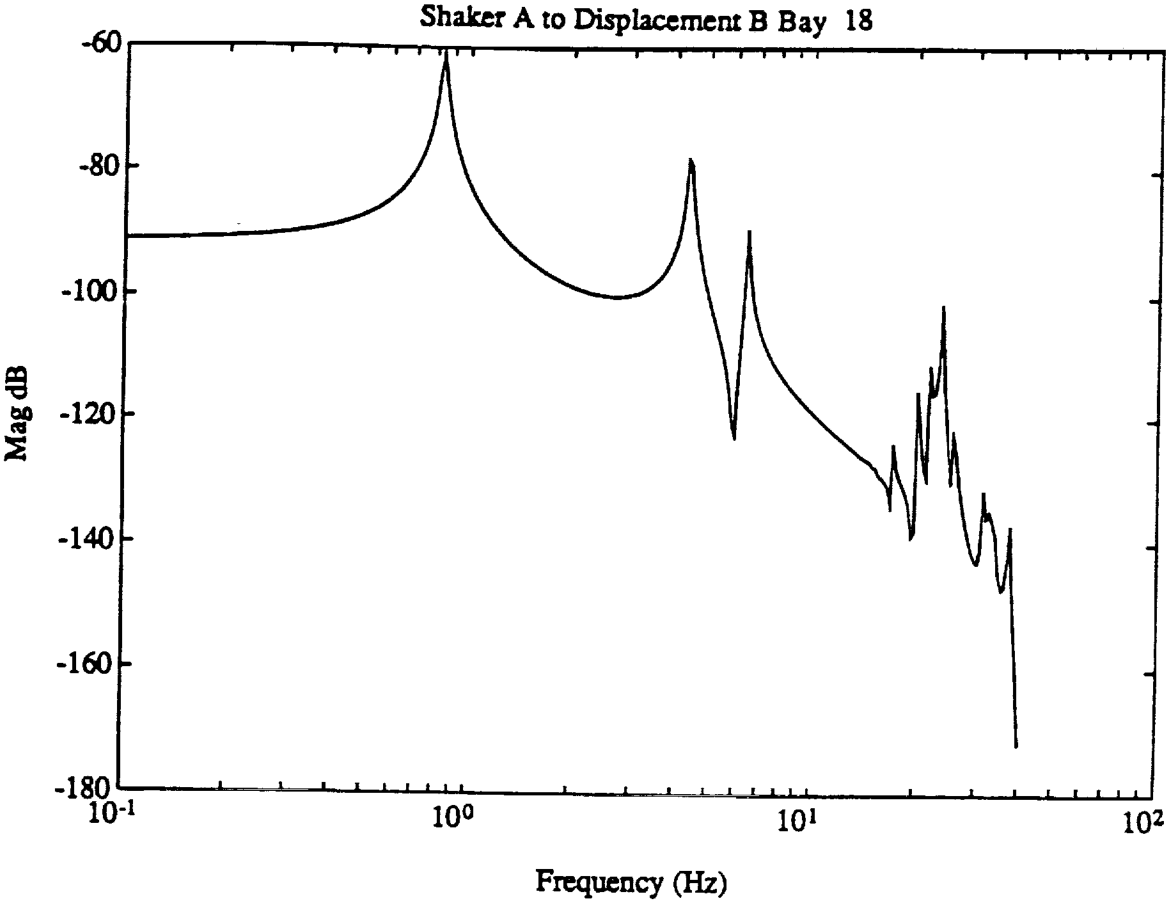

Figure 3.23 Bode Magnitude Plot of Shaker-A to Displacement-B of Bay 18 for Model 2

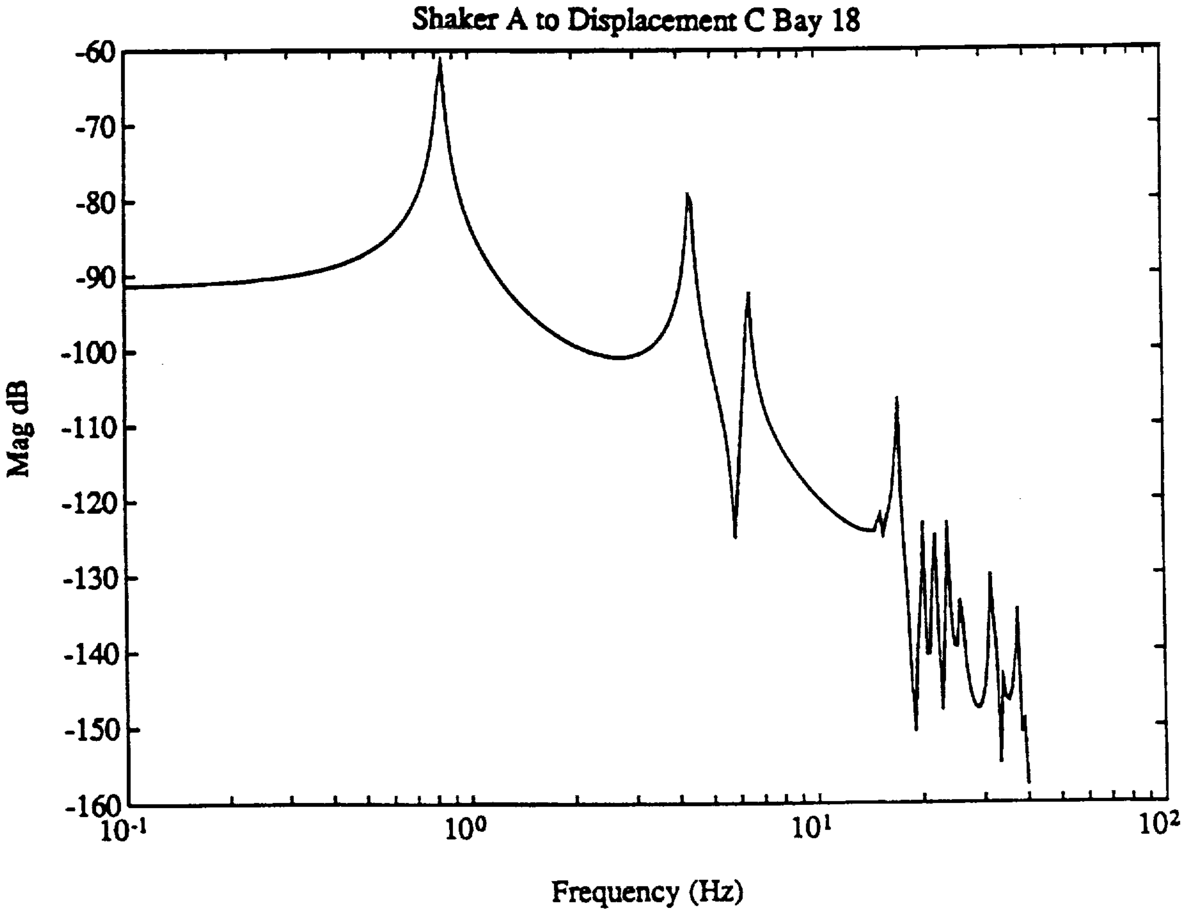

Figure 3.24 Bode Magnitude Plot of Shaker-A to Displacement-C of Bay 18 for Model 2

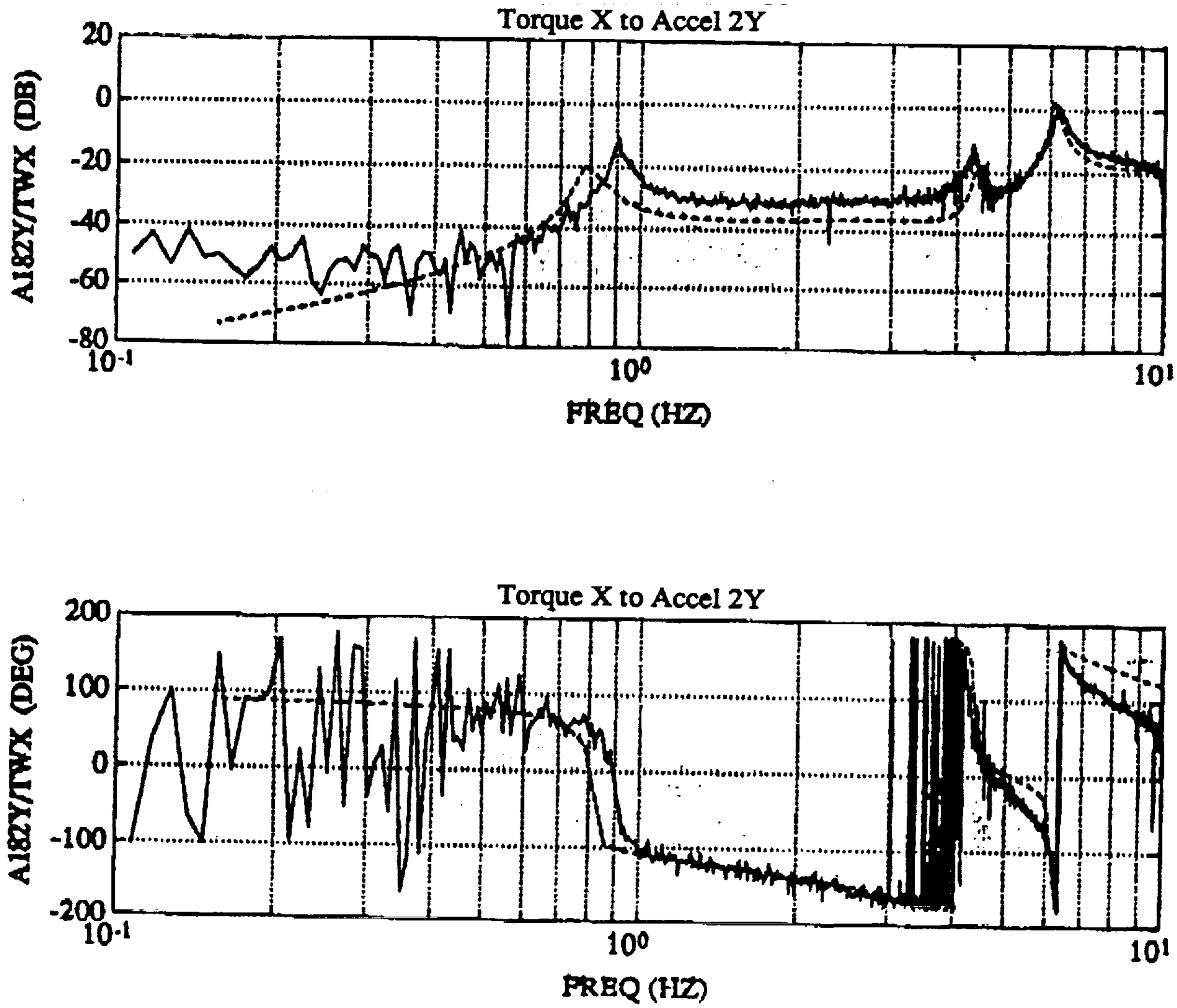

Figure 3.25 **Torque-X to Acceleration-2Y: Model 1 Bode Plots vs. Experimental Frequency Response Function (Experimental = Solid, Model 1 = Dashed)**

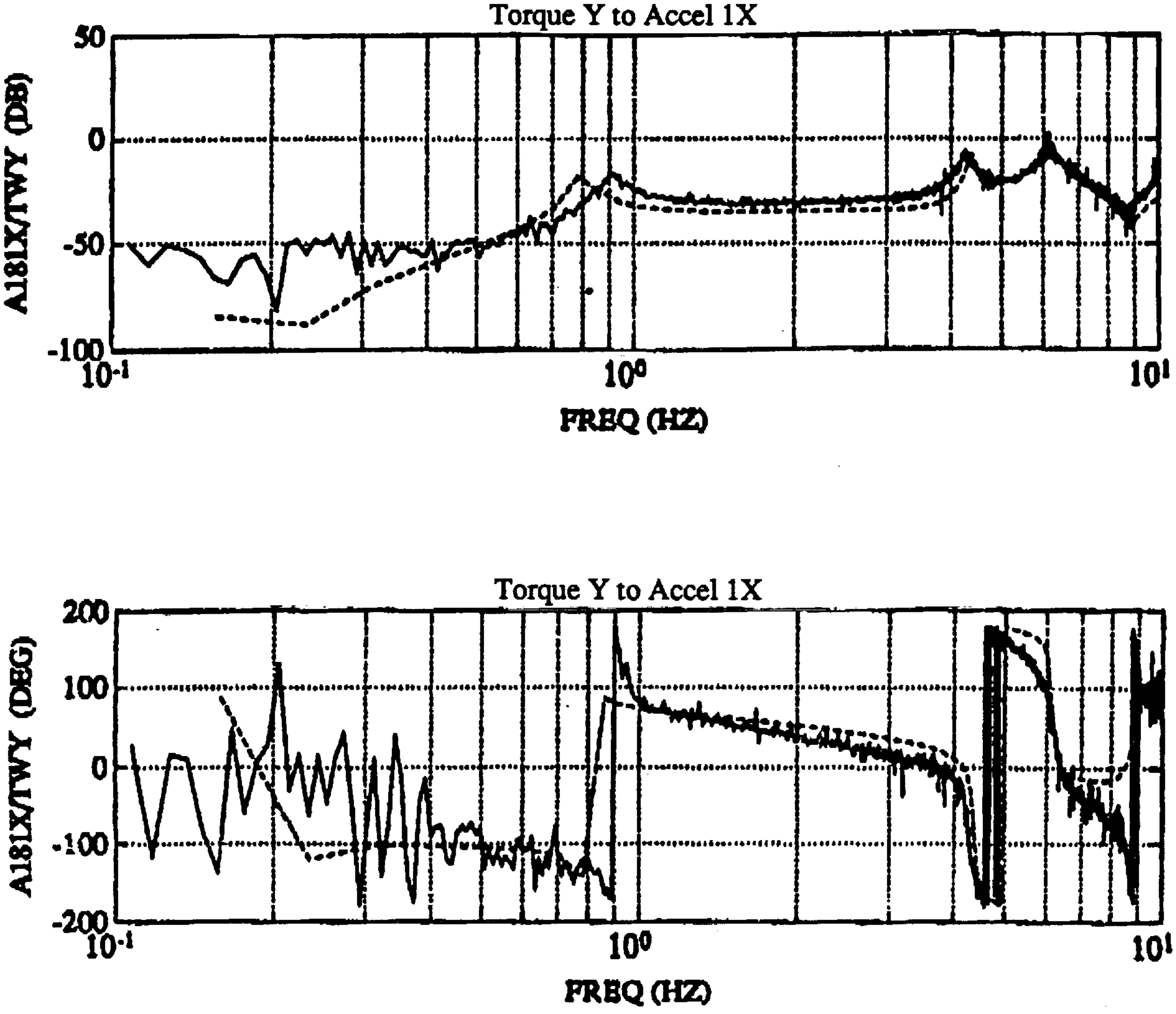

Figure 3.26 **Torque-Y to Acceleration-1X: Model 1 Bode Plots vs. Experimental Frequency Response Function (Experimental = Solid, Model 1 = Dashed)**

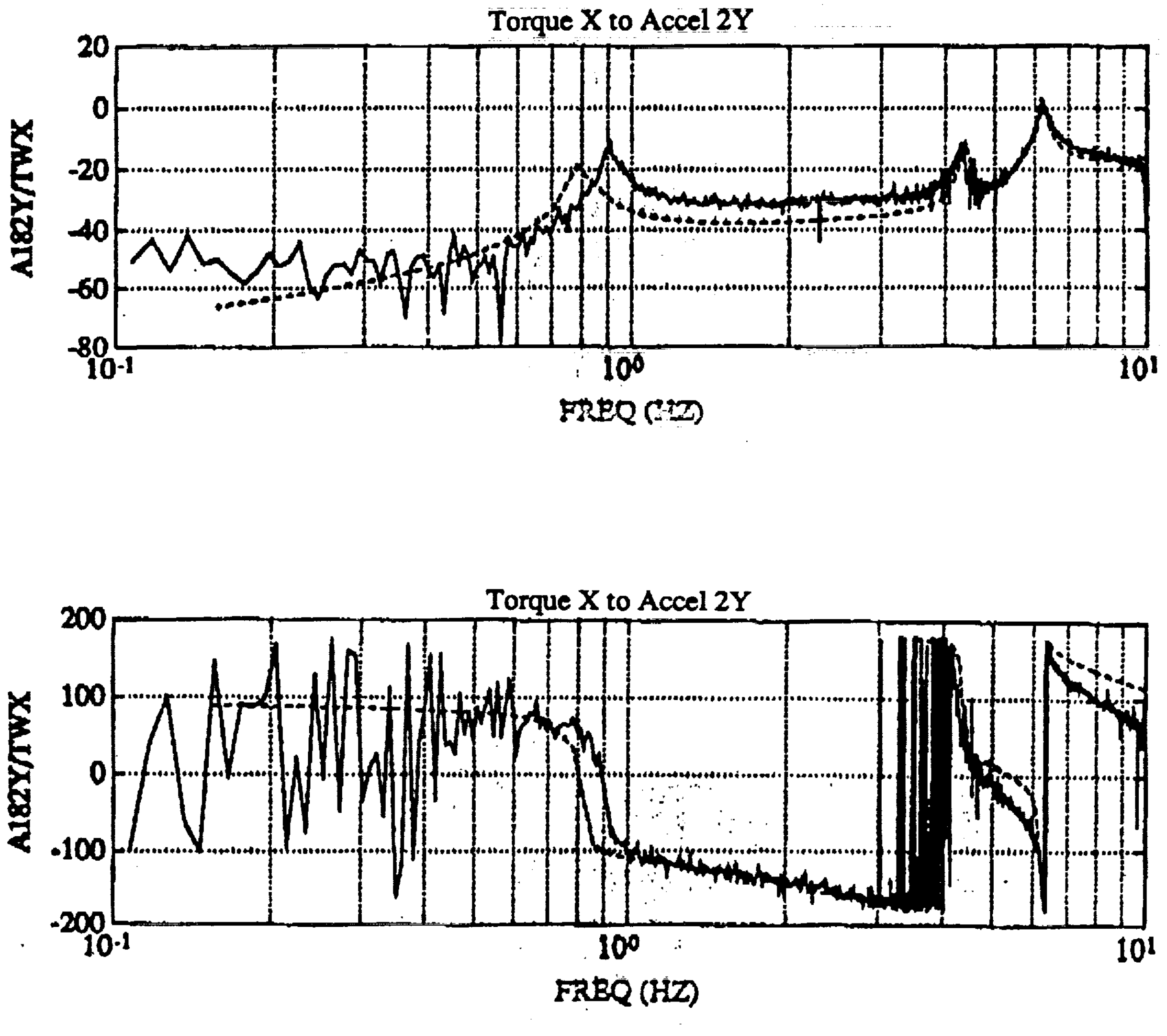

Figure 3.27 Torque-X to Acceleration-2Y: Model 2 Bode Plots vs. Experimental Frequency Response Function (Experimental = Solid, Model 2 = Dashed)

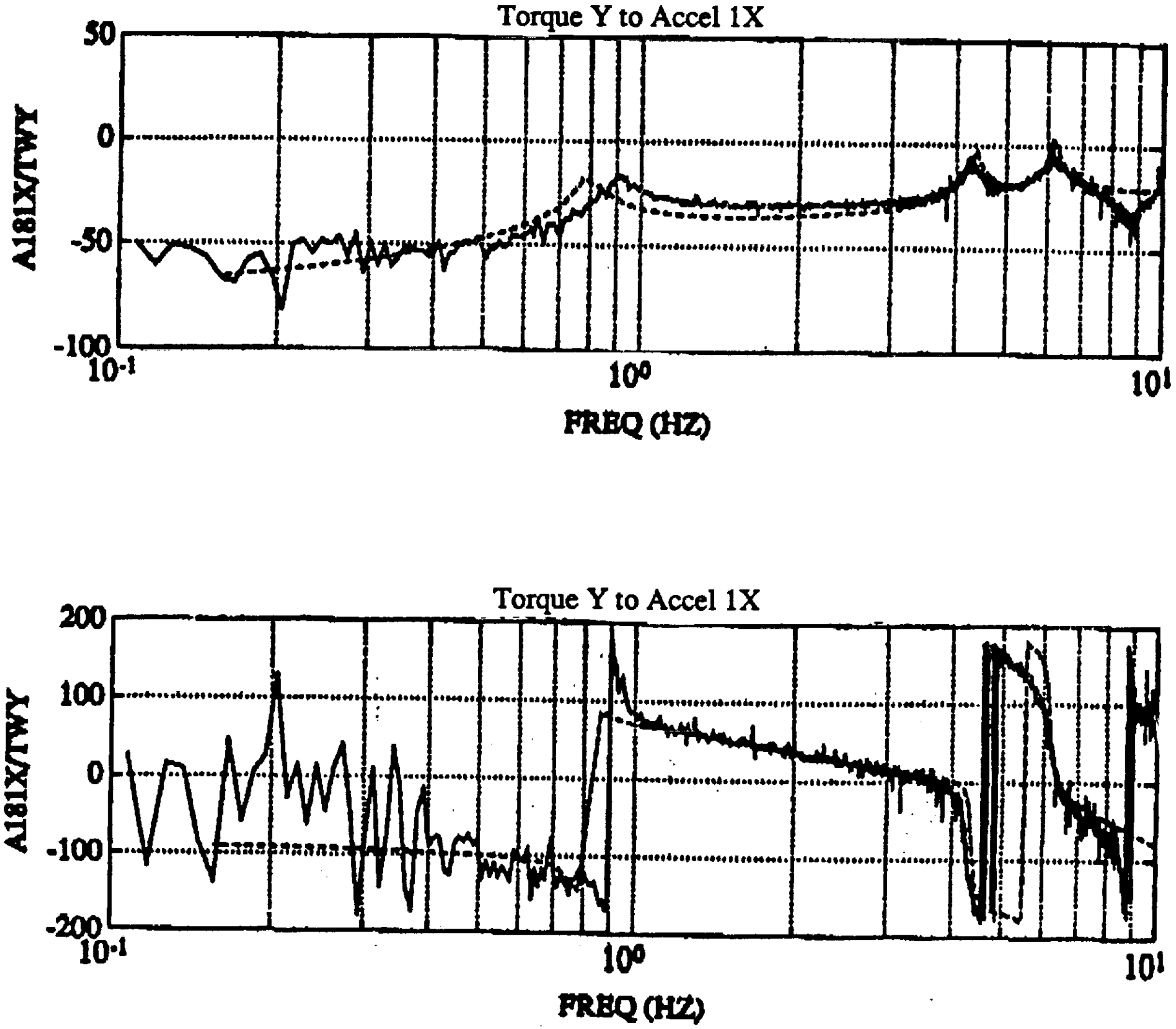

Figure 3.28 Torque-Y to Acceleration-1X: Model 2 Bode Plots vs. Experimental Frequency Response Function (Experimental = Solid, Model 2 = Dashed)

4.0 THE MAXIMUM ENTROPY/OPTIMAL PROJECTION APPROACH TO CONTROL DESIGN

Maximum Entropy/Optimal Projection design [3–7] assumes an uncertain plant of the form

$$\dot{x}(t) = (A + \Delta A)x(t) + (B + \Delta B)u(t) + w_1(t) \tag{4.1}$$

$$y(t) = (C + \Delta C)x(t) + w_2(t) \tag{4.2}$$

where $x \in \mathbb{R}^{n_x}$, $u \in \mathbb{R}^{n_u}$, $y \in \mathbb{R}^{n_y}$, $w_1 \in \mathbb{R}^{n_x}$ is white disturbance noise with nonnegative definite intensity V_1, $w_2 \in \mathbb{R}^{n_y}$ is white observation noise with positive definite intensity V_2, and w_1 and w_2 are uncorrelated. The state matrix A is assumed to be in real normal form such that A is block diagonal with scalar blocks corresponding to the real poles of the system and 2×2 blocks of the form $\begin{bmatrix} -\nu_1 & \omega_i \\ -\omega_i & -\nu_i \end{bmatrix}$ corresponding to the flexible modes. It is assumed that the uncertainty ΔA is of the form

$$\Delta A = \sum_{i=1}^{n_\alpha} \delta_i A_i, \quad |\delta_i| \le \alpha_i, \quad \alpha_i \ge 0 \tag{4.3}$$

where n_α denotes the number of uncertain modes and each A_i is of the form

$$A_i = \text{block-diag}\{0, \ldots, 0, \begin{bmatrix} 0 & 1 \\ -1 & 0 \end{bmatrix}, 0, \ldots, 0\} \tag{4.4}$$

corresponding to uncertainty in ω_i, the frequency of the i^{th} mode. In this experiment, it was assumed that $\Delta B = 0$ and $\Delta C = 0$.

Maximum Entropy/Optimal Projection design allows the synthesis of a fixed order dynamic compensator,

$$\dot{x}_c(t) = A_c x_c(t) + B_c y(t) \tag{4.5}$$

$$u(t) = -C_c x_c(t) \tag{4.6}$$

where $x_c \in \mathbb{R}^{n_c}$ and $n_c \le n_x$, that (in some sense) minimizes the steady-state performance criterion

$$J(A_c, B_c, C_c) \triangleq \lim_{t \to \infty} E[x^{\text{T}}(t) R_1 x(t) + u^{\text{T}} R_2 u(t)] \tag{4.7}$$

over the assumed uncertainty set. If we define

$$\Sigma \triangleq B R_2^{-1} B^{\text{T}} \quad \text{and} \quad \bar{\Sigma} \triangleq C^{\text{T}} V_2^{-1} C \tag{4.8}$$

then the controller gains are given by

$$A_c = \Gamma(A_s - \Sigma P - Q\bar{\Sigma})G^{\mathrm{T}} \tag{4.9}$$

$$B_c = \Gamma Q C^{\mathrm{T}} V_2^{-1} \tag{4.10}$$

$$C_c = R_2^{-1} B^{\mathrm{T}} P G^{\mathrm{T}} \tag{4.11}$$

where $Q, P, \hat{Q}$ and $\hat{P}$ are nonnegative definite solutions of the design equations

$$0 = A_s Q + Q A_s^{\mathrm{T}} + V_1 - Q\bar{\Sigma}Q + \sum_{i=1}^{n_\alpha} \alpha_i^2 A_i Q A_i^{\mathrm{T}} + \sum_{i=1}^{n_\alpha} \alpha_i^2 A_i \hat{Q} A_i^{\mathrm{T}} + \tau_\perp Q\bar{\Sigma}Q\tau_\perp^{\mathrm{T}} \tag{4.12}$$

$$0 = A_s^{\mathrm{T}} P + P A_s^{\mathrm{T}} + R_1 - P\Sigma P + \sum_{i=1}^{n_\alpha} \alpha_i^2 A_i^{\mathrm{T}} P A_i + \sum_{i=1}^{n_\alpha} \alpha_i^2 A_i^{\mathrm{T}} \hat{P} A_i + \tau_\perp^{\mathrm{T}} P\Sigma P Q \tau_\perp \tag{4.13}$$

$$0 = (A_s - \Sigma P)\hat{Q} + \hat{Q}(A_s - \Sigma P) + Q\bar{\Sigma}Q - \tau_\perp Q\bar{\Sigma}Q\tau_\perp^{\mathrm{T}} \tag{4.14}$$

$$0 = (A_s - Q\bar{\Sigma})^{\mathrm{T}}\hat{P} + \hat{P}(A_s - Q\bar{\Sigma}) + P\Sigma P - \tau_\perp^{\mathrm{T}} P\Sigma P\tau_\perp \tag{4.15}$$

$$\text{rank } \hat{Q} = \text{rank } \hat{P} = \text{rank } \hat{Q}\hat{P} = n_c \tag{4.16}$$

$$\tau = \hat{Q}\hat{P}(\hat{Q}\hat{P})^{\#}, \quad (\cdot)^{\#}\text{denotes the group generalized inverse} \tag{4.17}$$

and τ has the factorization

$$\tau = G^{\mathrm{T}}\Gamma, \quad G, \Gamma \in \mathrm{I\!R}^{n_c \times n_s}. \tag{4.18}$$

The Maximum Entropy design equations for full-order control law design are simply (4.12)–(4.15) with $\tau_\perp = 0$. In this case $\Gamma = G = I_{n_s}$ in (4.9)–(4.11). If we additionally assume perfect knowledge of the system (i.e., $A_i = 0$ for $i = 1, \ldots, n_\alpha$), then (4.12) and (4.13) become the standard LQG Riccati equations.

The design equations (4.12)-(4.17) can be solved by using a homotopy algorithm [8,9]. As illustrated in Figure 4.1, this homotopy algorithm allows the deformation of an LQG controller into a full order Maximum Entropy controller. The Maximum Entropy controller is then reduced to an appropriate order by using an indirect controller reduction method. It is important that this initial reduced-order controller approximately solves the Maximum Entropy/Optimal Projection design equations to within a small error, although it is not even required to be a stabilizing controller. This can be achieved by beginning with a low authority LQG design and/or incorporating a sufficiently high level of uncertainty in the Maximum Entropy design. In practice a slight modification of the balanced controller reduction algorithm of Youssuff and Skelton [13] is currently used as the indirect controller reduction method. Once this initial reduced-order controller is obtained, the algorithm is used to deform this controller into a Maximum Entropy/Optimal Projection controller. Then if a higher authority controller is desired, the final step of the algorithm is to increase the controller authority to a desirable level.

In this experiment it was found that the final two steps were actually unnecessary. That is, for each design the weights of the initial LQG controller could always be chosen such that the initial reduced-order controllers had performance that could not be significantly improved by better satisfying the Maximum Entropy/Optimal Projection equations and were also of sufficiently high authority. This desirable feature of the design process was a nice by-product of the precompensation methodology discussed in the next section.

Some key features of Maximum Entropy controllers are illustrated in Figures 4.2 thru 4.4 using controllers developed for the ACES structure. Each of these controllers used an approximately colocated angular rate sensor and torque actuator pair and were designed to attenuate all of the system modes less than 3 Hz.

Figure 4.2 shows that in the performance region (DC-3Hz) Maximum Entropy design yielded positive real controllers providing robust stability to frequency uncertainties in the plant. Figure 4.3 shows that, in the performance region, Maximum Entropy design smoothed out the compensator magnitudes, thus providing robust performance to shifts in the modal frequencies and indicating that the Maximum Entropy design reduced the order of the original LQG controller.

Figure 4.4 shows that, outside of the controller bandwidth, the Maximum Entropy design robustified the controller notches by increasing their width and depth. In the Mini-MAST experiment only this latter feature of Maximum Entropy design was needed since the LQG controllers were seen to be very robust within the controller bandwidth. This robustness was obtained primarily as a result of the wide separation between the first bending modes and the remaining structural modes and the precompensation methodology discussed in the next section.

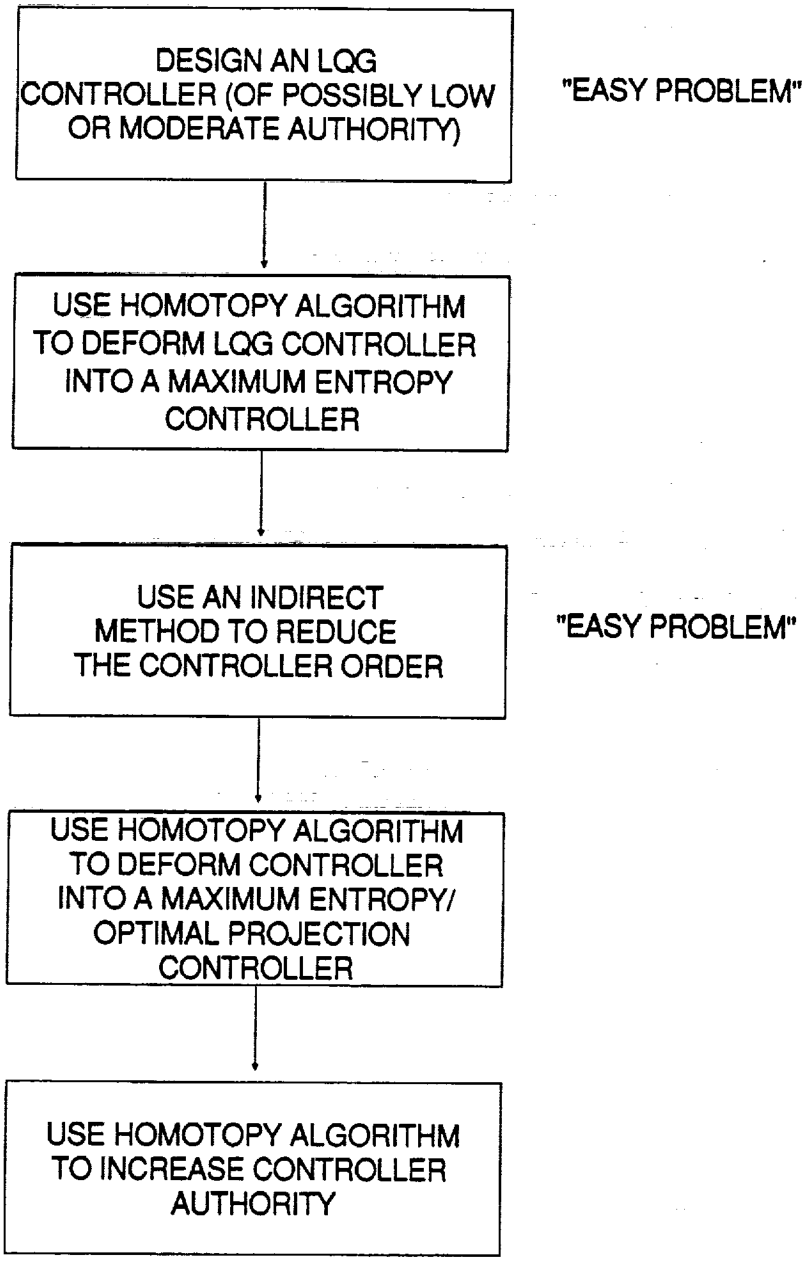

Figure 4.1 **The Practical Use of the Maximum Entropy/Optimal Projection Control Design Algorithm**

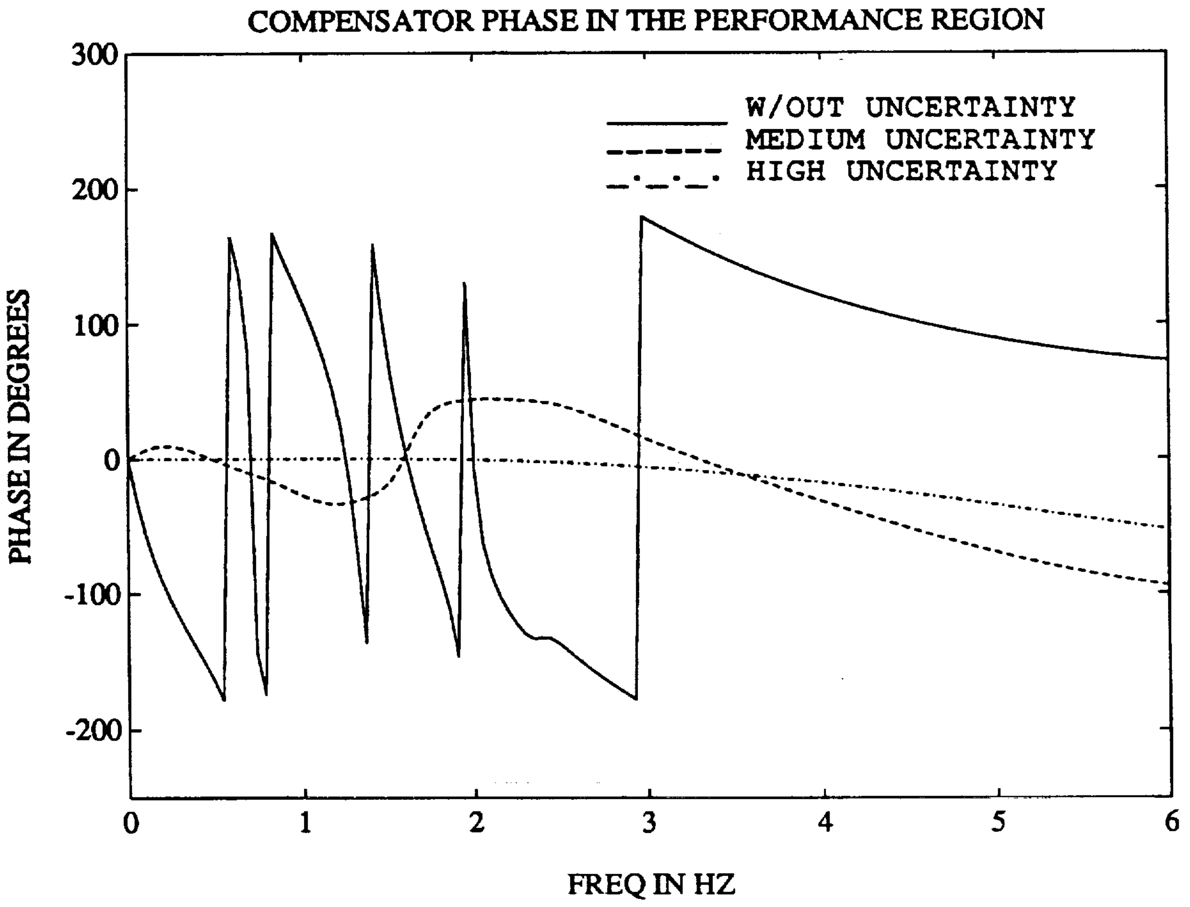

Figure 4.2 An Illustration of a Phase Stabilization Property of Maximum Entropy Controllers

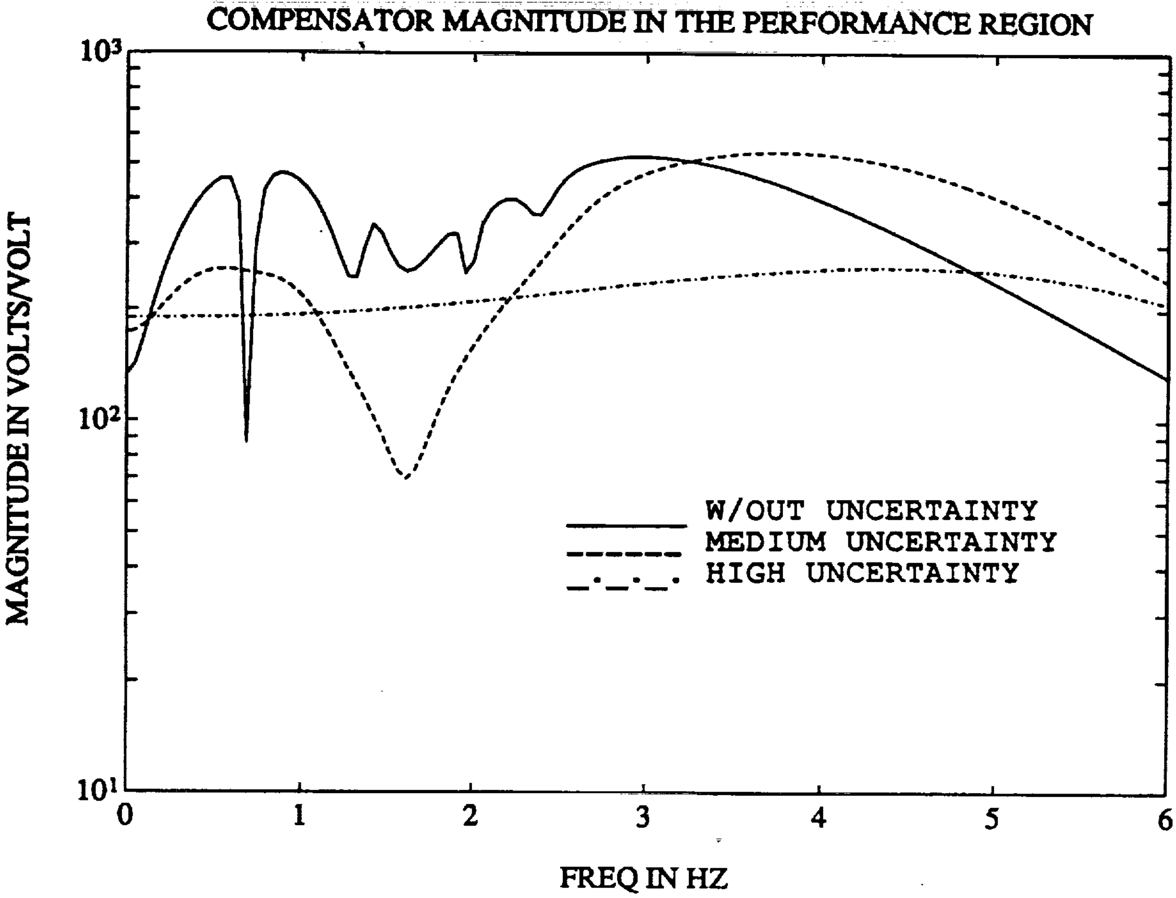

Figure 4.3 **An Illustration of Performance Robustness and an Order Reduction Property of Maximum Entropy Controllers**

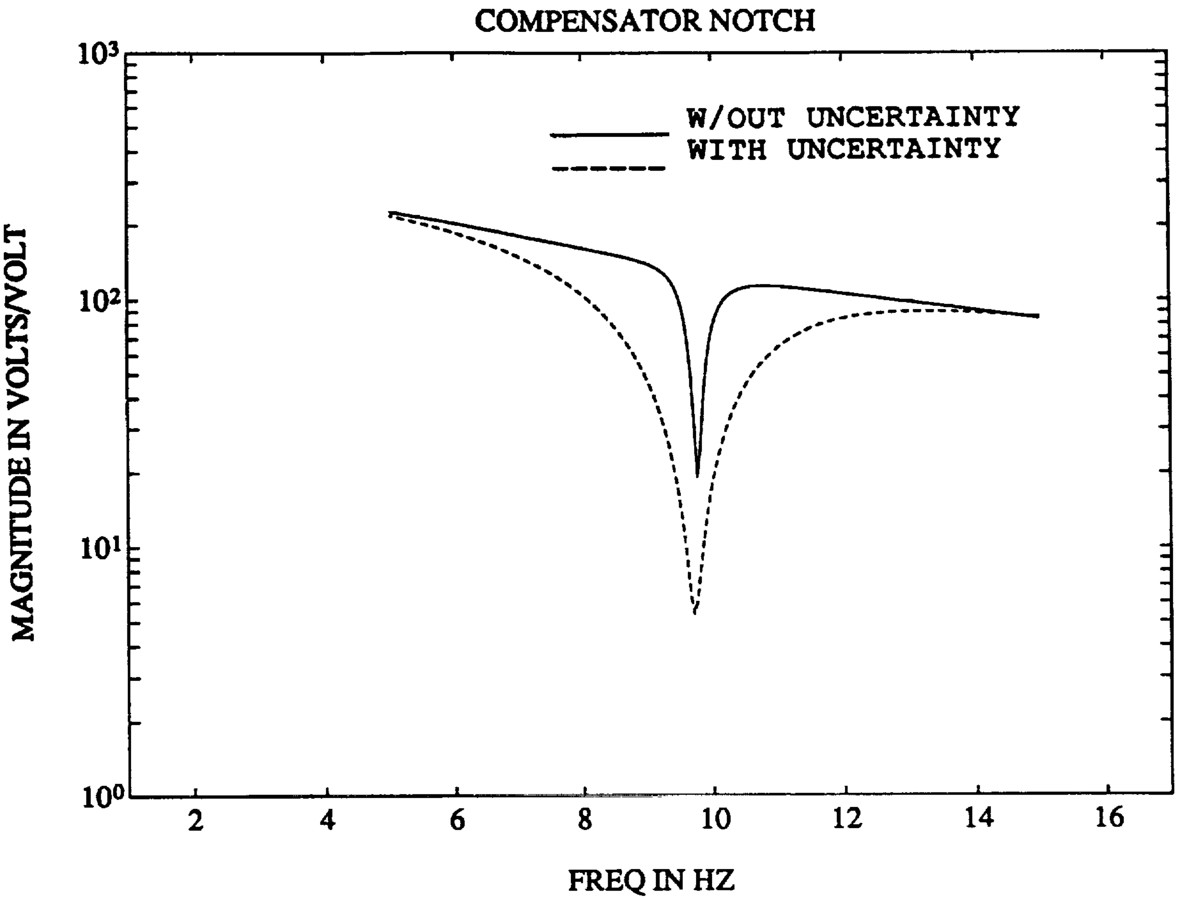

Figure 4.4 **An Illustration of Maximum Entropy Notch Robustification**

5.0 PROBLEM DEFINITION AND THE INTRODUCTION OF A PRECOMPENSATION METHODOLOGY FOR CONTROL DESIGN

As mentioned in the Introduction, the basic control objective is to minimize the displacements at the tip of the Mini-Mast. It is assumed that the Mini-Mast is subjected to a .1 sec pulse of 50 N amplitude from Shaker-A. It is evident from Figures 3.19 through 3.21 that if Shaker-A is used to excite the Mini-Mast with a pulse of infinitesimal duration, then in the open-loop the displacements at the tip are primarily due to the excitation of the first bending modes of the X and Y axes (at .8 Hz) with minor contributions from the first torsional mode (at 4.4 Hz) and the second bending modes of the X and Y axes (at 6.1 Hz and 6.2 Hz). Since the disturbance pulse is actually of finite duration, the contributions of the latter three modes is even further reduced. The dominance of the first bending modes in the open loop response is clearly seen in Figure 5.1 which shows the open-loop tip displacements to a .1 sec pulse from Shaker-A.

From the above discussion it is apparent that the performance objectives require the control of no more than 5 modes with the first two bending modes being the two most important modes to attenuate. The control design thus requires the control of these 5 modes without destabilizing the remaining higher frequency modes, all of which are above 15 Hz. Recognize that the experimental data discussed in Section 3.0 that was used to verify the accuracy of the two models is only valid below 10 Hz. Thus, we do not have confidence in our models above 10 Hz and wish to ensure stability of these modes by having the compensators roll-off these modes to achieve gain stabilization.

An additional motivation for using a roll-off strategy for achieving the desired high frequency stabilization is that we are actually going to use continuous-time models and design theory for the control designs. The controllers must then be discretized for implementation at 80 Hz. This discretization will tend to distort the higher frequency dynamics of the continuous-time compensators which can cause instability when the discretized controllers are implemented. The use of compensator roll-off for high frequency stabilization reduces the importance of high frequency compensator dynamics.

It is important to note that, for this problem, the desired roll-off is not achieved by a straight forward application of LQG design theory. This fact is illustrated by Figure 5.2 which shows an LQG compensator designed using a reduced-order model of the Torque-X to Accel-2Y transfer function. The reduced model included only one mode above 10 Hz, a 20.3 Hz mode. The LQG compensator was designed to attenuate the first bending mode at .8 Hz. The compensator shown in Figure

5.2 has sufficient gain at the first bending mode to achieve significant performance improvement but interacts with the 20 Hz mode by notching it and has enough gain above 20 Hz to potentially destabilize the unmodeled modes. This type of compensator is clearly undesirable.

The desired roll-off can be ensured by assuming norm-bounded uncertainty and using either H_∞ [13–18] or μ-synthesis [19,20] control design. Alternatively, one could use frequency weighted LQG [18,21,22] to attempt to achieve the desired roll-off. Here, however, we use a different strategy which, like frequency weighted LQG, is heuristically based. However, the "precompensation" methodology we used does have some attractive features. In particular, it avoids the great increase in dimensionality of the design model that is sometimes resultant from using H_∞, μ-synthesis or frequency weighted LQG methods. Also, this methodology is very easy to implement. As illustrated by the subsequent results, this method was very effective for achieving the control design objectives for the Mini-Mast structure.

The basic idea behind the precompensation methodology is very simple and is illustrated in Figure 5.3 and 5.4. As shown in Figure 5.3, we simply embed the precompensation filters (in this case roll-off filters), $C_u(s)$ and $C_y(s)$ in the plant a priori and design the Maximum Entropy/Optimal Projection controller $\hat{H}(s)$ for this modified design plant. Then, as illustrated in Figure 5.4, the precompensation dynamics are included in the implemented compensator $H(s)$. This methodology guarantees that the implemented controller will stabilize the nominal plant and also guarantees that the nominal performance will be that predicted in the design process since the closed loop eigenvalues of the feedback systems shown in Figure 5.3 and 5.4 are identical and for both figures

$$\frac{z}{w} = \frac{G_{11}(1+HG_{22}) - G_{12}HG_{21}}{1+HG_{22}} \tag{5.1}$$

where

$$H = C_u\hat{H}C_y. \tag{5.2}$$

However, it is necessary to check after the design process as to whether the compensator achieved the desired roll-off (or robustness to high frequency unstructured uncertainty).

The actual roll-off filters used are described in the next section.

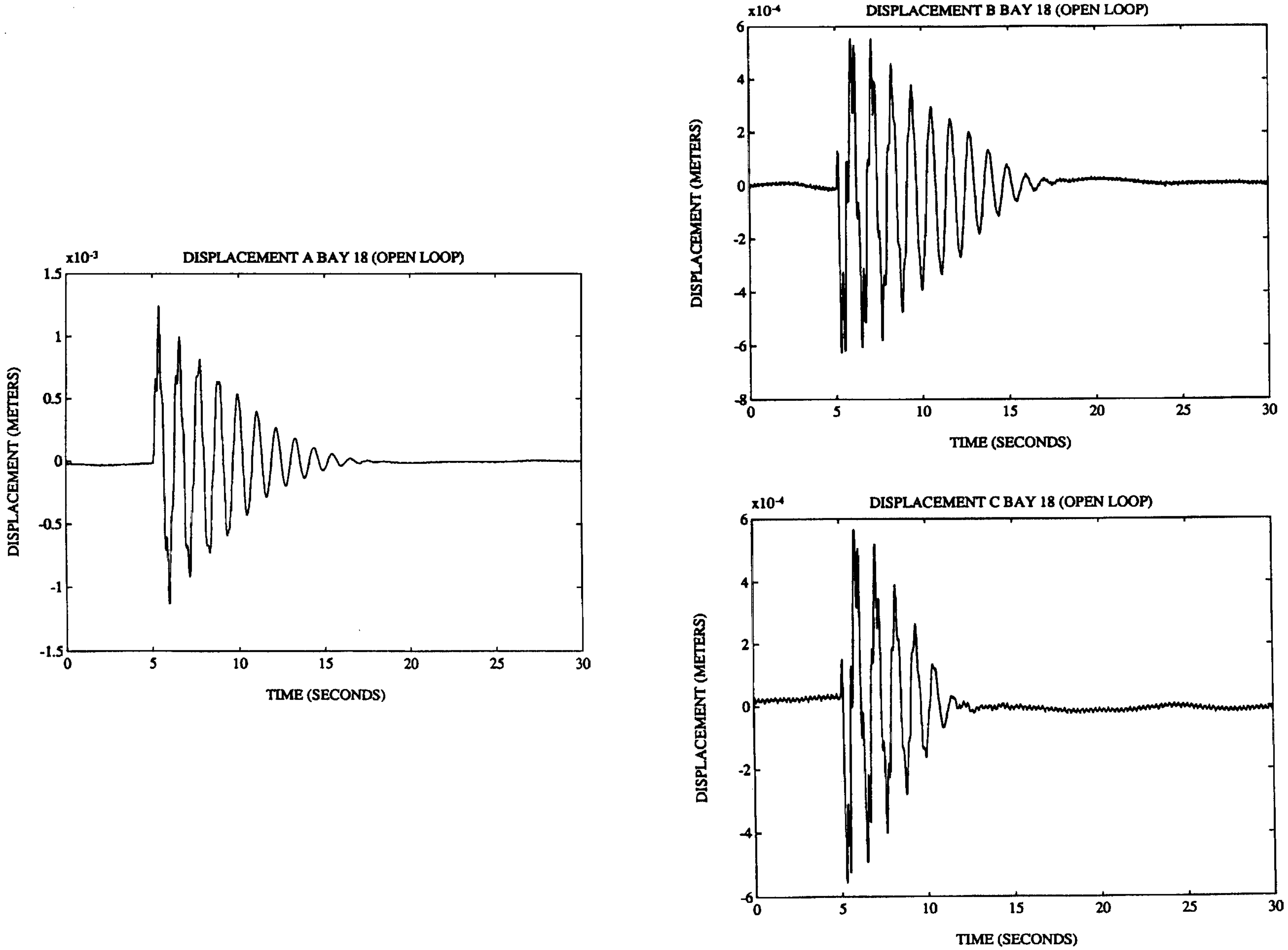

Figure 5.1 The Open Loop Tip Displacements to a .1 sec Shaker-A Pulse

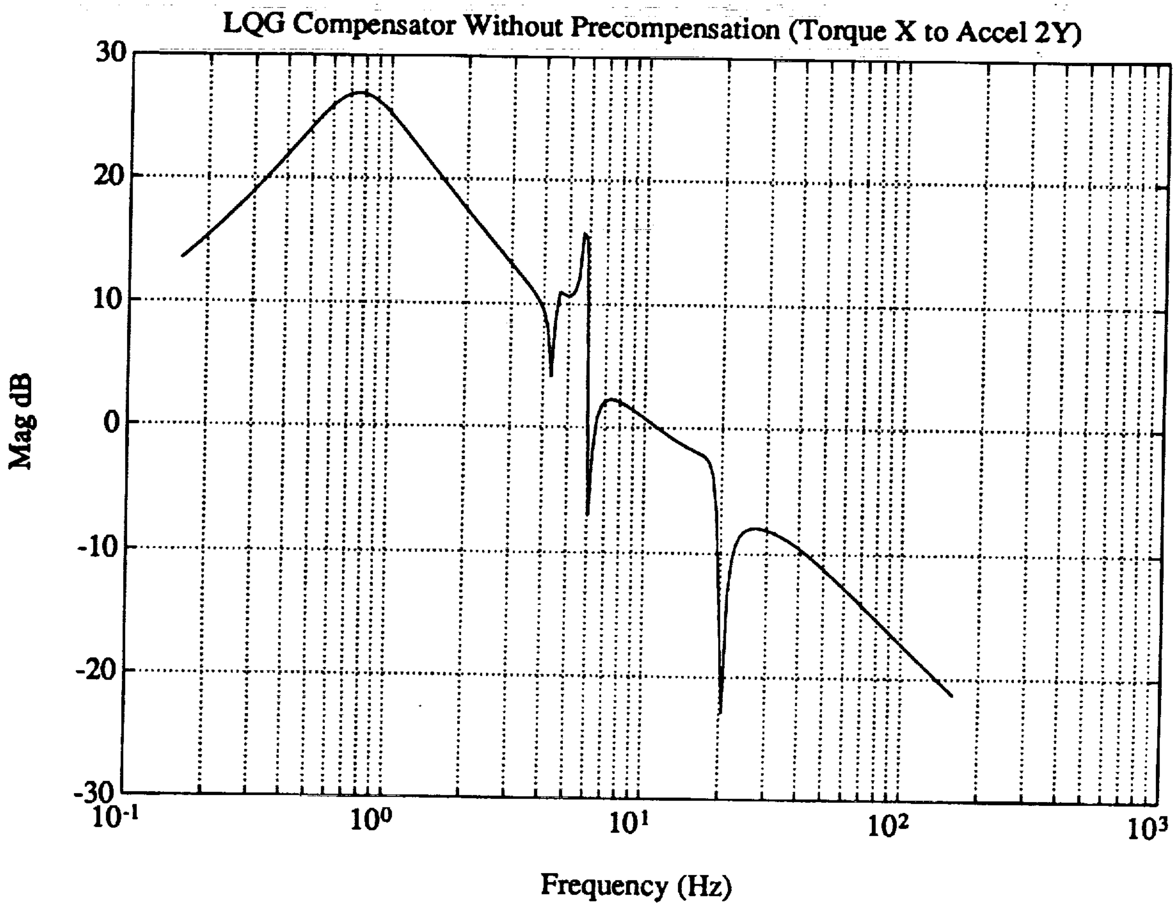

Figure 5.2 Frequency Response Magnitude of an LQG Compensator Designed Without Using Precompensation

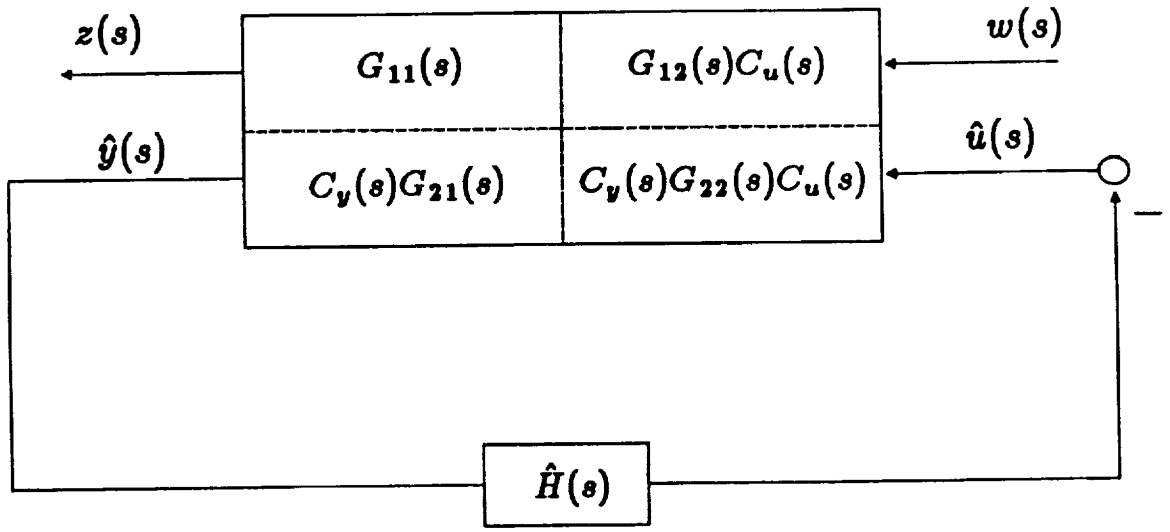

$$\hat{y}(s) = C_y(s)y(s) \qquad u(s) = C_u(s)\hat{u}(s)$$

Figure 5.3 **Design Configuration for the Precompensation Methodology**

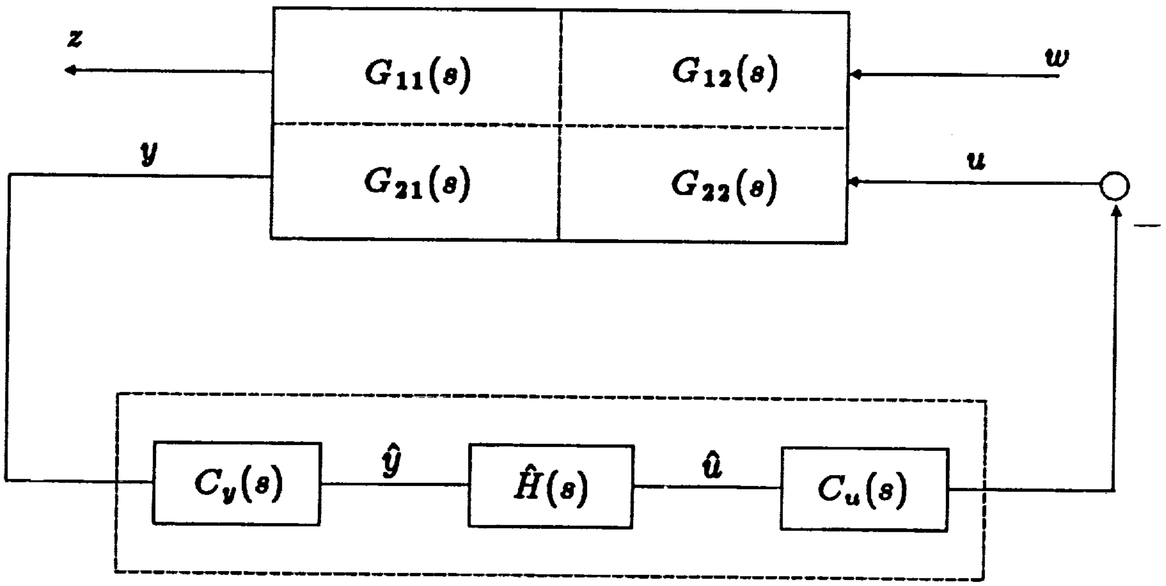

$$H(s) = C_u(s)\hat{H}(s)C_y(s)$$

Figure 5.4 Actual Implementation for the Precompensation Methodology

6.0 CONTROL DESIGN STRATEGY AND MODELS

A very practical control design and implementation strategy was used in this experiment. First, controllers with simple architectures (i.e., controllers which are decentralized, reduced order and use few sensors) were developed. Decentralized designs are more desirable for actual flight implementation because they ease the processor requirements, but can be more difficult to design because decentralization requires a careful analysis of the physics of the structure. Subsequently, centralized control laws were developed in an attempt to improve the performance. The centralized design with the best performance did significantly improve the performance of the "best" decentralized design.

From Figure 3.21 it was apparent that the transfer function from Torque-Z to Rate Gyro-Z was dominated by the first torsional mode at 4.4 Hz. Hence, it appeared feasible to use simple decentralized constant gain feedback from Rate Gyro-Z to Torque-Z to achieve high attenuation of the torsional mode. A full-order discrete-time model of the system was developed using Model 1 to represent the system at the 80 Hz sampling frequency. This model was used to perform a root locus and it was determined from this root locus that the "optimal" gain was K=10. *All* of the implemented controllers were designed assuming that this feedback loop was closed. These designs added feedback loops that use only the accelerometers and the X and Y torques. The use of the Rate Gyro-Z to Torque-Z feedback essentially eliminated the influence of the torsional mode on the remaining loops as illustrated by Figure 6.1. The resultant performance improvement in the torsional motion is shown in Figure 6.2.

Next, we considered attenuating the first bending modes in each axis by feeding back accelerometer outputs to the X and Y torque wheels. Since Acceleration-1X and Acceleration-2X provided essentially the same information about the acceleration of the Mini-MAST tip in the X-direction, we decided to use only one of these accelerometers and chose Acceleration-1X. Likewise we chose to use Acceleration-2Y instead of both Acceleration-2Y and Acceleration-1Y. The remaining accelerometers, Acceleration-X and Acceleration-Y, were located near the center of the Mini-MAST at Bay 10.

It was apparent from Figures 3.9, 3.10, 3.14 and 3.15 that the first bending modes were not very controllable and observable in the four transfer functions from Torque-X and Torque-Y to Acceleration-X and Acceleration-Y. However, Figures 3.7, 3.8, 3.12 and 3.13 revealed that the first bending modes were very controllable and observable in the four transfer functions from Torque-X and Torque-Y to Acceleration-1X and Acceleration-2Y. Hence, we initially chose to feed back only the latter two accelerometers to attenuate the first bending mode. Furthermore, it was evident from the latter four figures that the dominant transfer functions were from Torque-X to Acceleration-2Y and Torque-Y to Acceleration-1X. We thus chose to design feedback laws for the two loops corresponding to these transfer functions.

Reduced-order continuous-time models were developed for the transfer functions Torque-X to Acceleration-2Y and Torque-Y to Acceleration-1X. First order all-pass filters were included in each model to account for the phase lag due to computational delay. Precompensation dynamics were added to each reduced-order model to yield the models actually used to design the Maximum Entropy/Optimal Projection controllers. The Torque-X to Acceleration-2Y design model and the Torque-Y to Acceleration-1X design model each contained 20 states.

The precompensation for each of the two control problems was chosen so that the modified design plant appeared to have a rate measurement and a true torque input within the control bandwidth. The precompensation thus consisted of dynamics to integrate the accelerometer output and dynamics to cancel the effects of the actuator dynamics below 10 Hz. This choice of precompensation added the desired roll-off to the original design plant and also allowed us to develop a baseline rate-feedback design. Because the transfer functions for each of the two control problems were so similar, we decided to use the same precompensation for both. Referring to Figure 5.3, the precompensation used is given by

$$C_u(s) = \frac{s + 62.8}{s^2 + .628s + .3944} \quad , \quad C_y(s) = 1. \tag{6.1}$$

Due to the requirements of Maximum Entropy Design, each of the modified design models was placed in real normal form. Thus the A matrix of each of the modified design models was block-diagonal with one of the blocks of the form $\begin{bmatrix} -\nu_1 & \omega_1 \\ -\omega_1 & -\nu_1 \end{bmatrix}$ corresponding to the first bending mode. The disturbance weighting matrix, V_1, and the performance state weighting matrix, R_1, were each chosen to be block diagonal with the only nonzero block corresponding to the position of the first bending mode in the A matrix. The nonzero block of V_1 is given by $\begin{bmatrix} 0 & 0 \\ 0 & \alpha \end{bmatrix}$ and the nonzero block of R_1 is given by $\begin{bmatrix} \alpha & 0 \\ 0 & 0 \end{bmatrix}$ where α is a scalar parameter which was used to determine the controller authority. This choice of weighting matrices was equivalent to assuming that the system was disturbed by a force actuator and the performance output was a displacement sensor that sees only the first bending mode when an impulse is placed in the system by the force actuator. Also, we chose $R_2 = V_2 = 1$.

The centralized designs used a reduced-order continuous-time model which contained 12 structural modes. This model also included two first-order all-pass filters to account for the phase lag due to computational delay. Precompensation dynamics were added to the reduced order model which yielded a design model with 54 states.

The precompensation dynamics that we used for the centralized controllers differed from that used for the decentralized controllers. The reason for this change was primarily an attempt to eliminate some of the low frequency oscillation that appeared in the output of the displacement sensors and ultimately limited the achievable performance of the decentralized designs. We initially attributed this low frequency oscillation to the migration of the low frequency poles of the precompensation dynamics towards the right half plane, although subsequent control designs and analyses revealed that this was not actually the case. Referring again to Figure 5.3, the precompensation used is given by

$$C_u(s) = \operatorname{diag}\{C_{u,1}(s), C_{u,2}(s)\}, \quad C_y(s) = I \tag{6.2}$$

where

$$C_{u,1}(s) = C_{u,2}(s) = \frac{39.0625 \times 10^4}{(s^2 + 18.8755 + 62.5)(s^2 + 45.969 + 625)}. \tag{6.3}$$

$C_{u,1}(s)$ and $C_{u,2}(s)$ are 4 Hz Butterworth filters.

The weighting scheme used for the centralized controllers is very straight-forward. The modified design model as before was placed in real normal form. Let $u_d \in \mathbb{R}$ denote the input corresponding to Shaker-A, $z_a \in \mathbb{R}^3$ denote a performance vector whose elements correspond to Displacements A, B and C of Bay 18, $z_b \in \mathbb{R}^3$ denote the performance vector whose elements correspond to Displacements A, B, and C of Bay 10, and let x denote the state vector of the modified design model in real normal form. We computed the input matrix D corresponding to u_d and matrices P_a and P_b such that $z_a = P_a x$ and $z_b = P_b x$. The disturbance matrix, V_1, and the state weighting were then chosen as

$$V_1 = \alpha D D^{\mathrm{T}}, \quad R_1 = \alpha P_a^{\mathrm{T}} P_a + \beta P_b^{\mathrm{T}} P_b \tag{6.4}$$

where the scalar parameter α was used to determine the controller authority. The scalar parameter β was chosen to be zero for the initial designs but was given a finite value in latter designs in order to penalize the Bay 10 displacements. The use of the parameter β was motivated by the fact that the dominant behaviour at Bay 10 was due to the second bending mode pair. Thus, β was essentially used to reduce the influence of the second bending modes on the displacement responses at Bay 18.

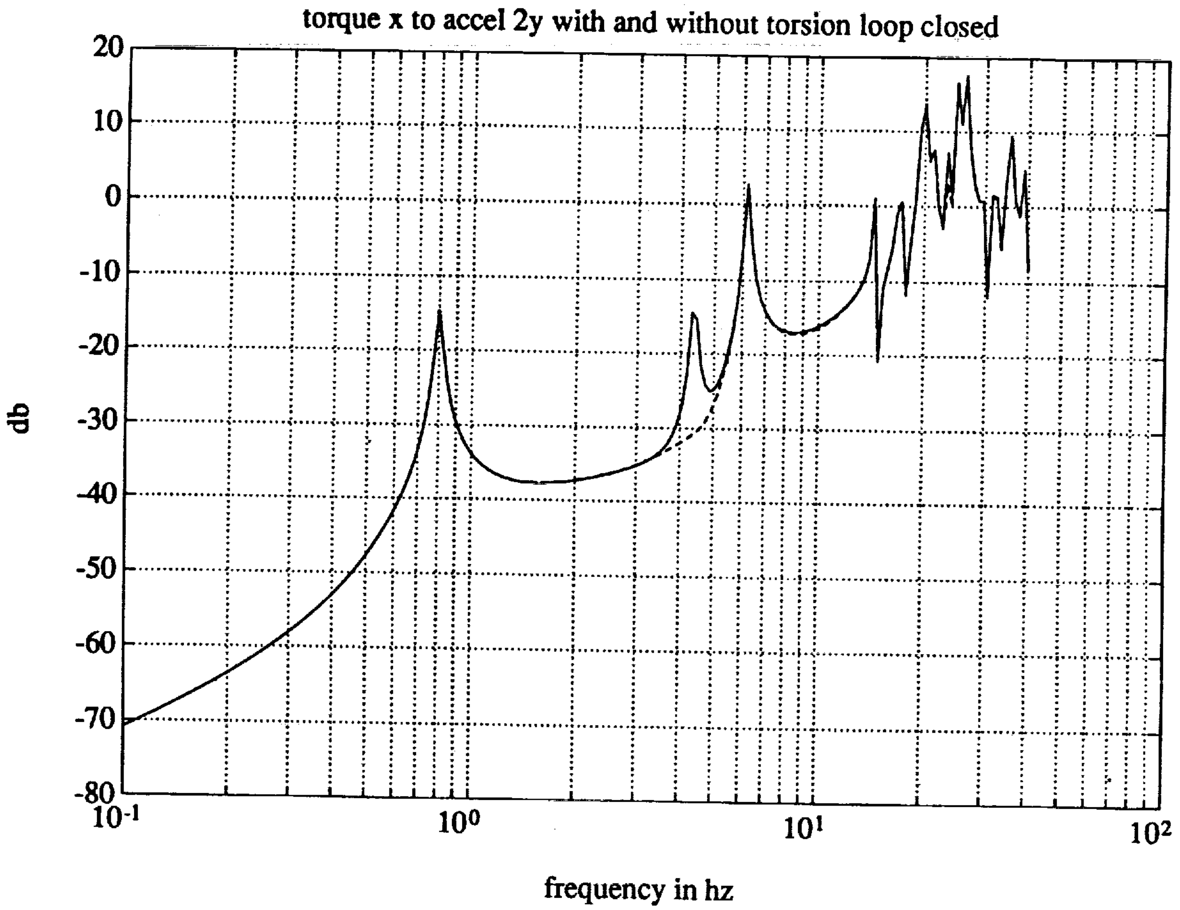

Figure 6.1 **The Effectiveness of Constant Gain Feedback in Eliminating the Influence of the Torsional Mode**

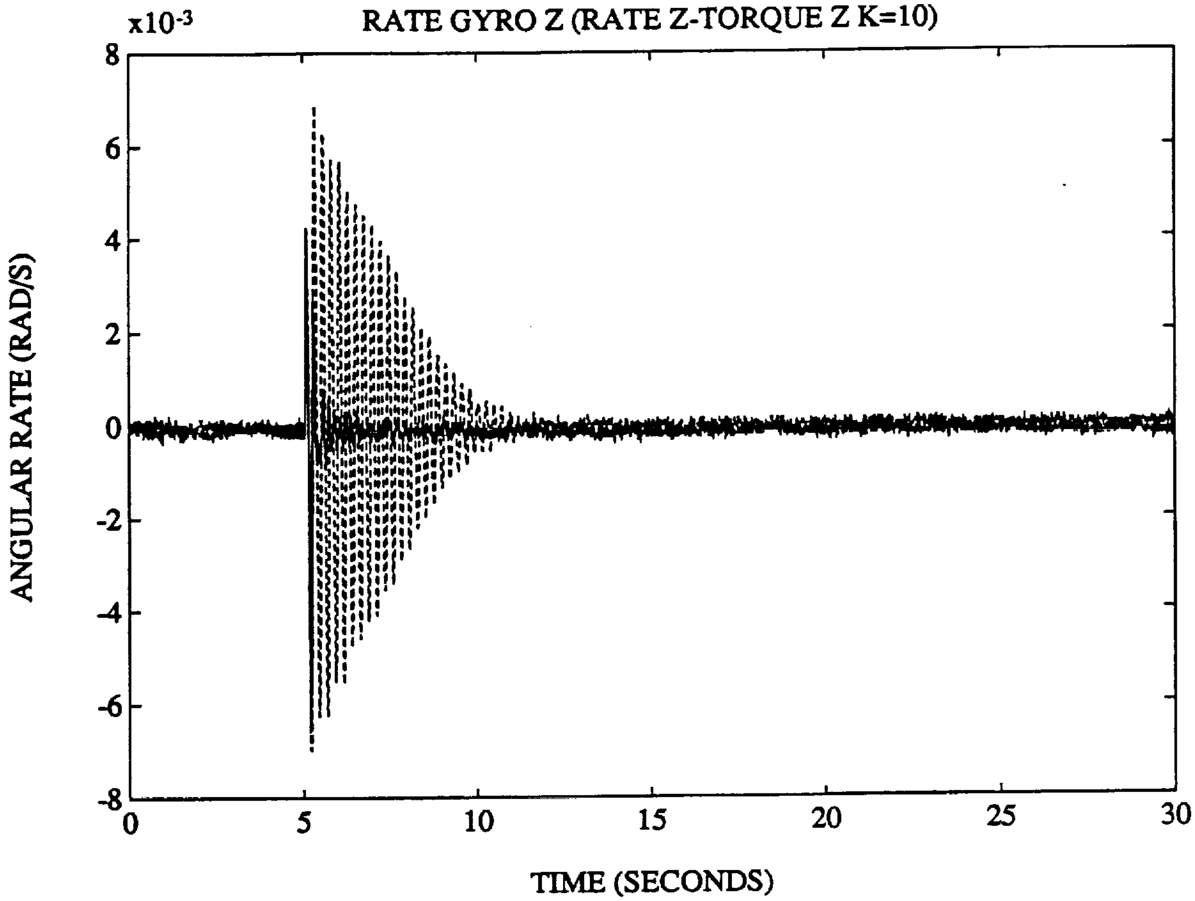

Figure 6.2 Open Loop vs. Closed Loop Rate Gyro-Z Response for Constant Gain Feedback from Rate Gyro-Z to Torque-Z (Closed Loop = Solid, Open Loop = Dashed)

7.0 DECENTRALIZED CONTROL DESIGNS

This section describes in more detail the decentralized controllers discussed in the previous section and presents the resultant performance improvement. Four controllers are described, each of which was designed using the precompensation methodology of Section 5.0. Each controller was also designed assuming that a decentralized constant gain feedback loop from Torque-Z to Rate Gyro-Z (with gain K=10) was closed. This feedback loop essentially eliminated the effects of the first torsional mode. Hence, although the controllers described used only Accelerometers-1X, 2Y, X and Y for sensing and Torques X and Y for actuation, it is important to keep in mind that they were implemented in conjunction with the constant gain feedback law from Torque-Z to Rate Gyro-Z.

Each of the four decentralized controllers include at least two subcontrollers, one feeds back Accelerometer-2Y to Torque-X while the other feeds back Accelerometer-1X to Torque-Y. These two subcontrollers were designed using the precompensation methodology of Section 6.0 with precompensation dynamics given by (6.1). Controller 1 consisted of two subcontrollers. Referring to Figure 5.3, these subcontrollers were designed by simply choosing $\hat{H}(s)$ equal to a constant. Since the precompensation was chosen to make the design plants $C_y(s)G(s)C_u(s)$ for each subcontroller appear to have a rate measurement and a true torque input within the control bandwidth, Controller 1 approximates a rate feedback controller and was used as a baseline design. Controller 2 also included only two subcontrollers and was designed without assuming uncertainty in any of the first five modes. Controller 3 was similar to Controller 2 except that it was designed assuming uncertainty in the second bending mode pair. Controller 4 consisted of Controller 3 plus two additional subcontrollers designed using classical control concepts. One of these subcontrollers feeds back Accelerometer-Y to Torque-X while the other subcontroller feeds back Accelerometer-X to Torque-Y.

7.1 Controller 1: A Pseudo Rate Feedback Controller

This controller consisted of two subcontrollers, one from Accelerometer-2Y to Torque-X and one from Accelerometer-1X to Torque-Y. This controller was our least complex and, as previously mentioned, was used as a baseline design. The open loop vs. closed loop Bay 18 displacement responses are shown in Figure 7.1. Although this controller did provide substantial increase in the performance, it will subsequently be seen that more complex controllers can achieve much better performance.

7.2 Controller 2: A Reduced Order LQG Controller Using Bay 18 Accelerometers

Like Controller 1, this controller consisted of two subcontrollers, one from Accelerometer-2Y to Torque-X and one from Accelerometer-1X to Torque-Y. However, the feedback laws in this case were designed using LQG. The decentralized feedback laws for each loop were each of order 9 (including the precompensation) so that the implemented controller was of order 18. The open loop vs. closed loop Bay 18 displacement responses are shown in Figure 7.2.

7.3 Controller 3: A Reduced Order Maximum Entropy Controller Using Bay 18 Accelerometers

This controller was a robustified version of Controller 2 and was of order 20. It was designed assuming uncertainty in the second bending mode pair and, as shown in Figure 7.3, the Maximum Entropy design robustified the corresponding notches for these two modes. This uncertainty description was originally motivated by an analysis of Controller 2 which indicated that the controllers were extremely sensitive to uncertainties in the second bending modes. However, due to the high fidelity of the models provided by NASA, subsequent analysis revealed that robustness was not really needed. Nevertheless, the Maximum Entropy design yielded useful gain margin at the frequency of the second bending modes and allowed us to scale the subcontrollers to further attenuate the influence of the second bending modes on the performance. The open loop vs. closed loop Bay 18 displacement responses are shown in Figure 7.4.

7.4 Controller 4: Controller 3 plus a Classical Controller Using Bay 10 Accelerometers

This controller consisted of Controller 3 plus two subcontrollers, $H_1(z)$ and $H_2(z)$ which were designed using classical control concepts. $H_1(z)$ was used in the feedback path from Accelerometer-Y to Torque-X while $H_2(z)$ was used in the feedback path from Accelerometer-X to Torque-Y. These two subcontrollers were designed to further attenuate the second bending modes and are given respectively by

$$H_1(z) = K_1 z/(z - .9245)$$

$$H_2(z) = K_2 z/z(z - .9245)^2$$

where K_1 and K_2 are constant gains. The implemented compensator was of order 24. The open loop vs. closed loop Bay 18 displacement responses are shown in Figure 7.5. The corresponding displacement responses at Bay 10 are shown in Figure 7.6 while the commands to the torque wheels are shown in Figure 7.7. The desired attenuation of the second bending modes was achieved as can be seen by comparing the performance of Controller 3, as shown in Figure 7.4, to the performance of Controller 4, shown in Figure 7.5.

Figure 7.8 shows the performance for each of the controllers as evidenced from Displacement-A of Bay 18. The results were very close to the predicted results shown in Figure 7.9. This close correlation was largely due to the fidelity of the models provided by NASA Langley and is also partially due to the robustness of the controllers. Tha gains of Controller 4 are given in the Appendix.

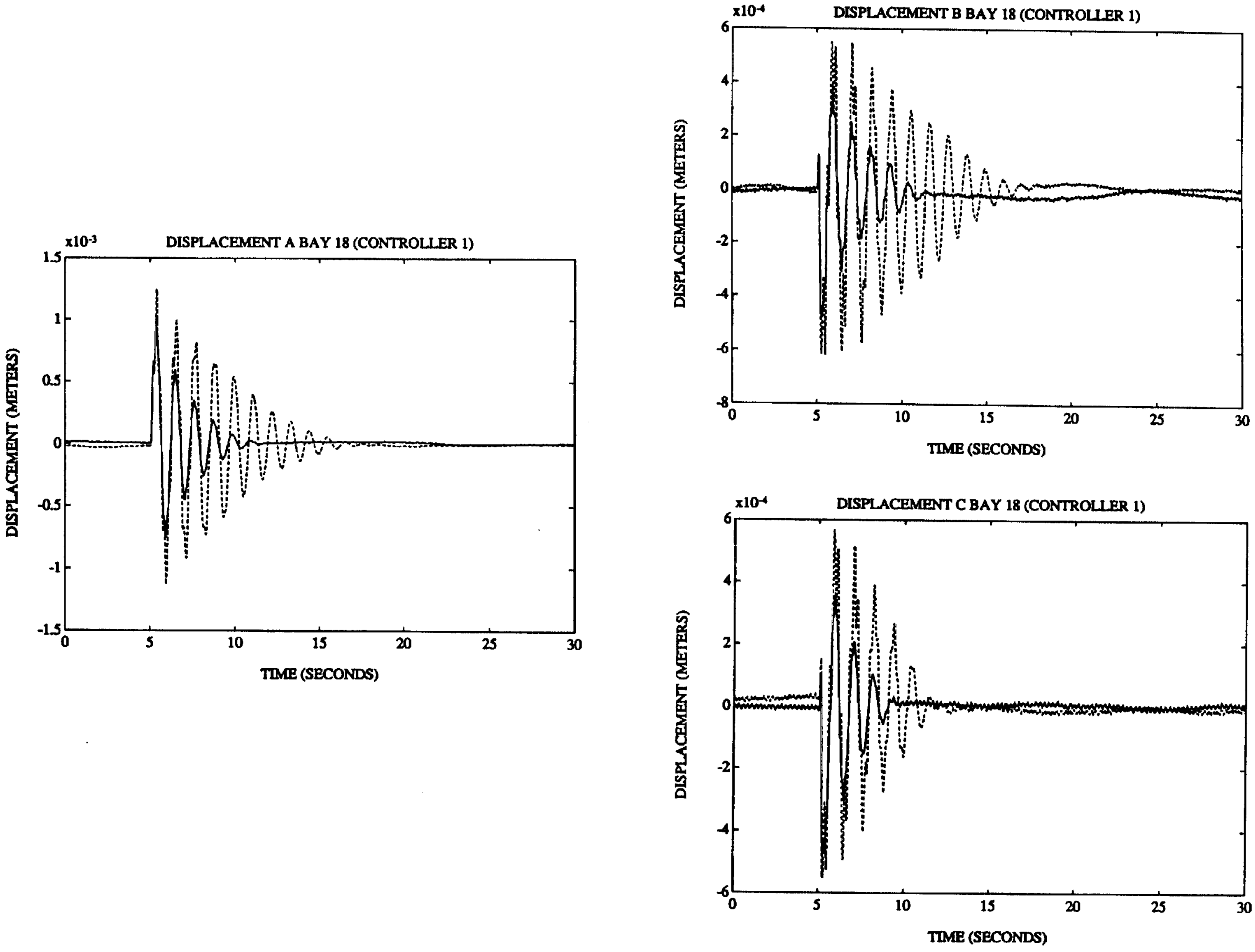

Figure 7.1 Open Loop vs. Closed Loop Bay 18 Displacement Responses for Controller 1 (Closed Loop = Solid, Open Loop = Dashed)

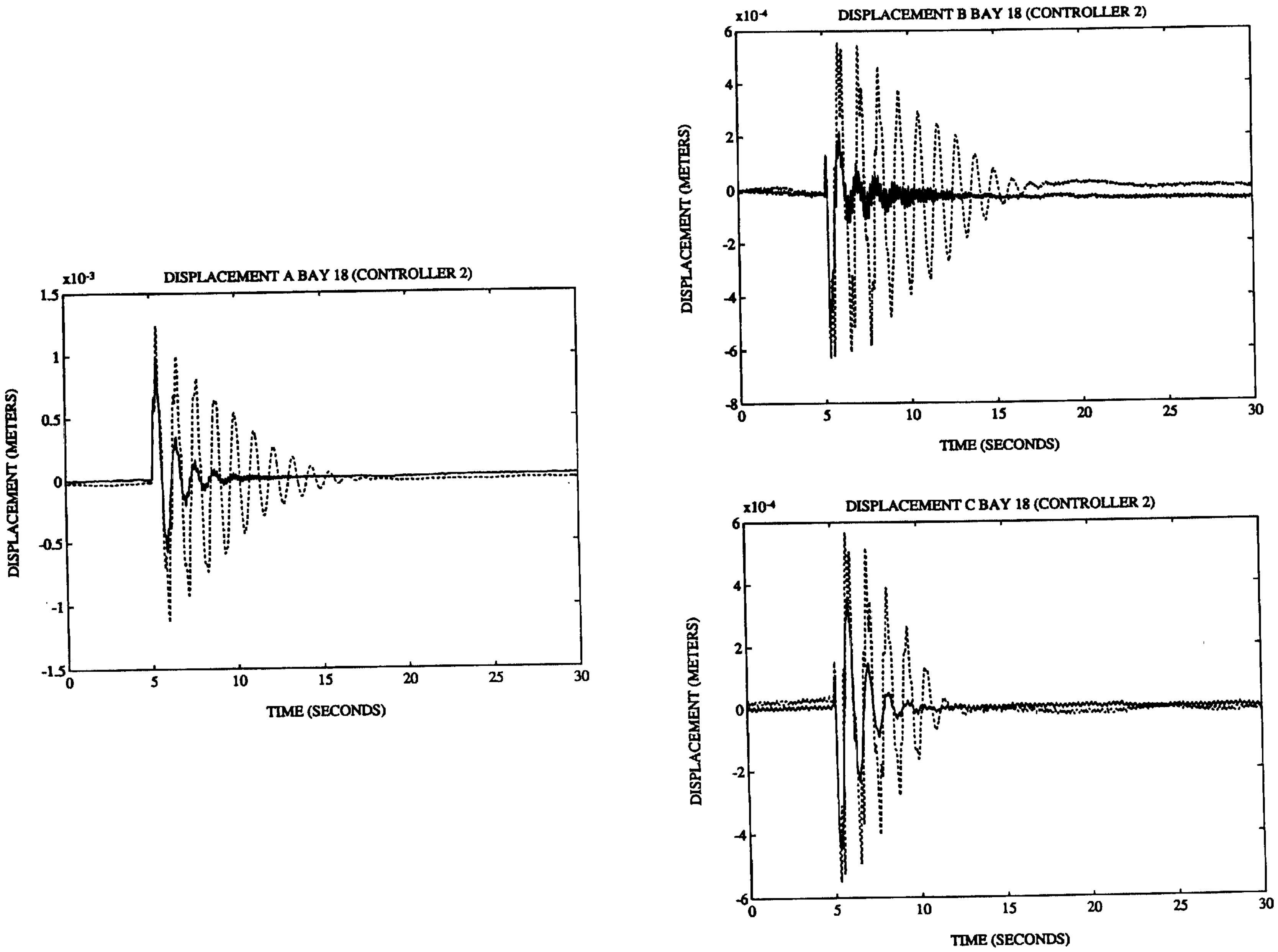

Figure 7.2 Open Loop vs. Closed Loop Bay 18 Displacement Responses for Controller 2 (Closed Loop = Solid, Open Loop = Dashed)

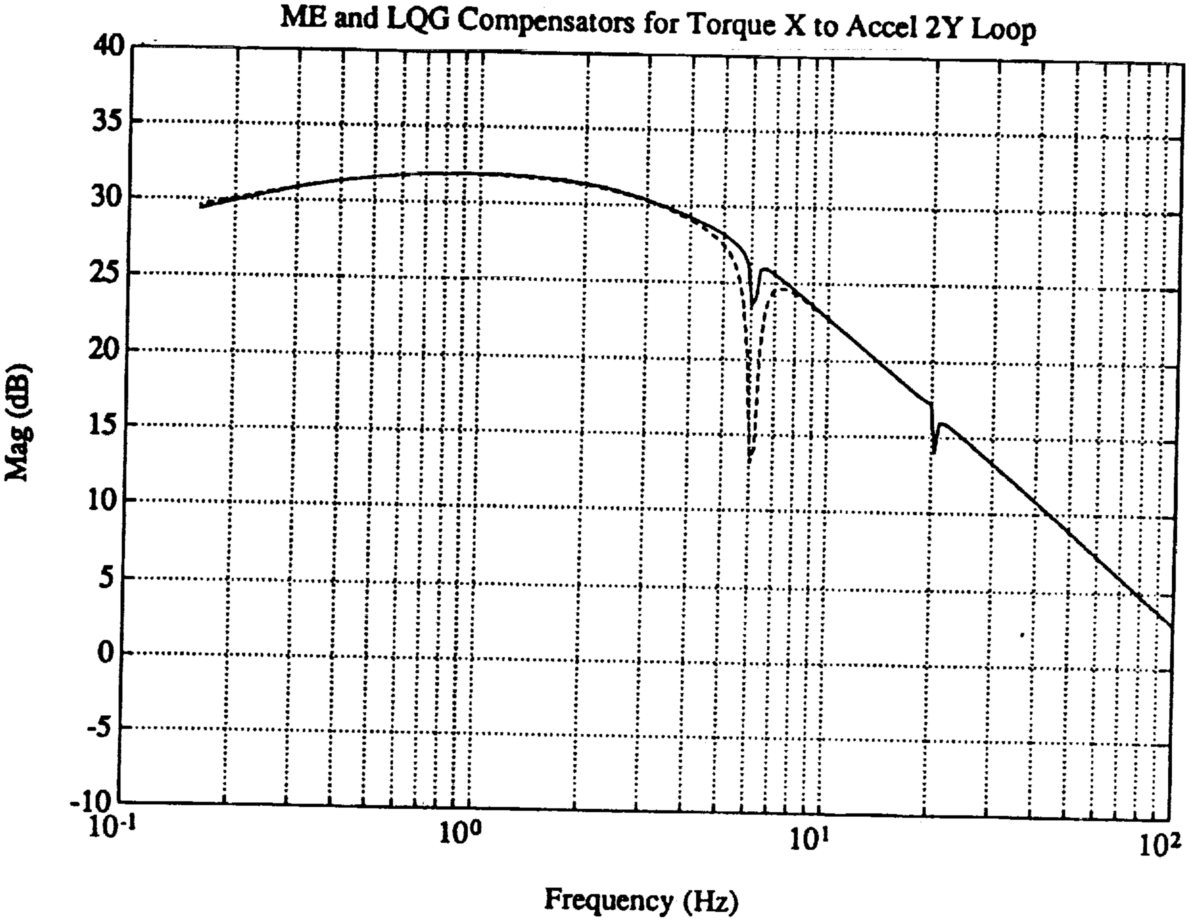

Figure 7.3 Comparison of the Magnitude Bode Plots for the Acceleration-2Y to Torque-X Subcontroller of Controllers 2 and 3 (Controller 2 = Solid, Controller 3 = Dashed)

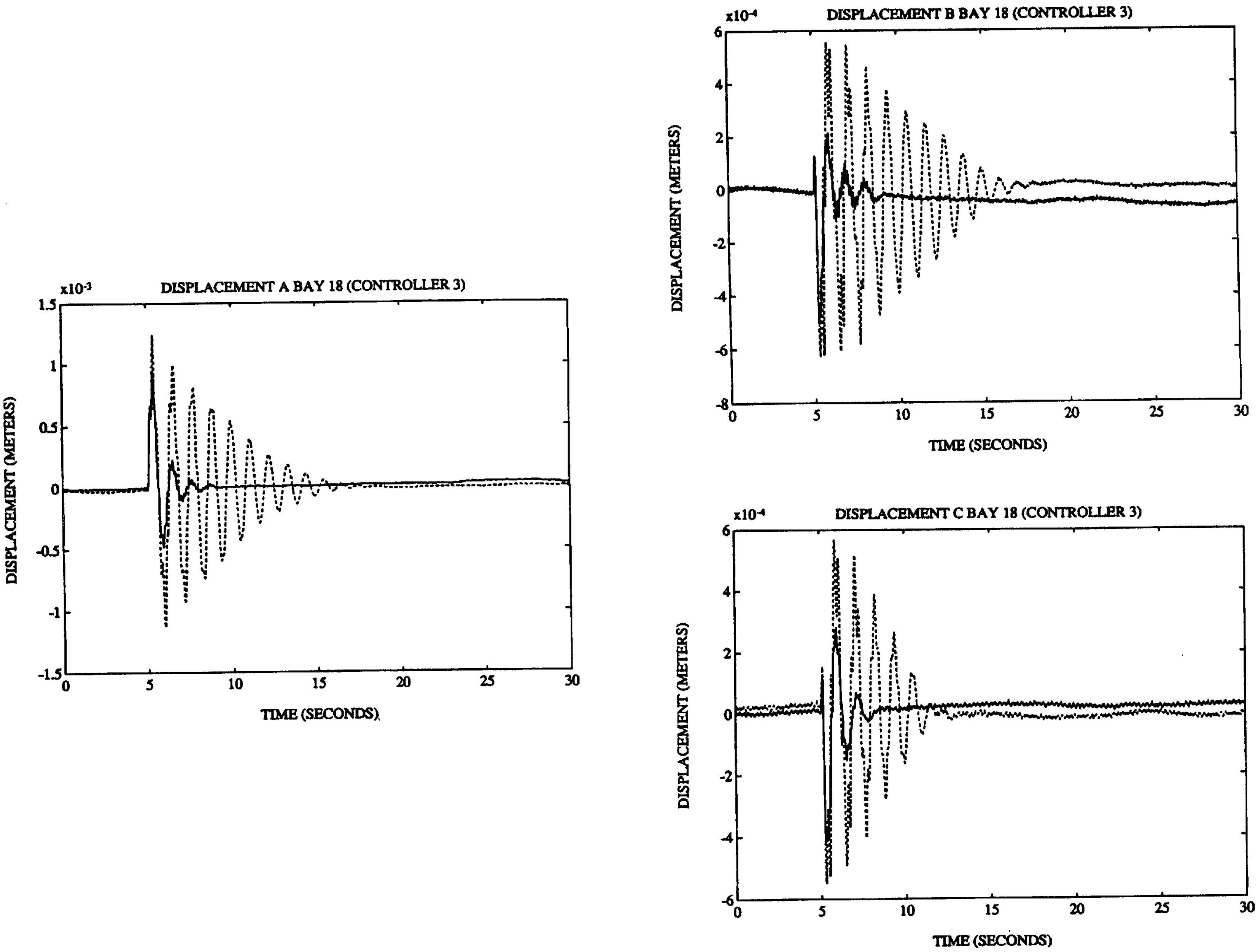

Figure 7.4 Open Loop vs. Closed Loop Bay 18 Displacement Responses for Controller 3 (Closed Loop = Solid, Open Loop = Dashed)

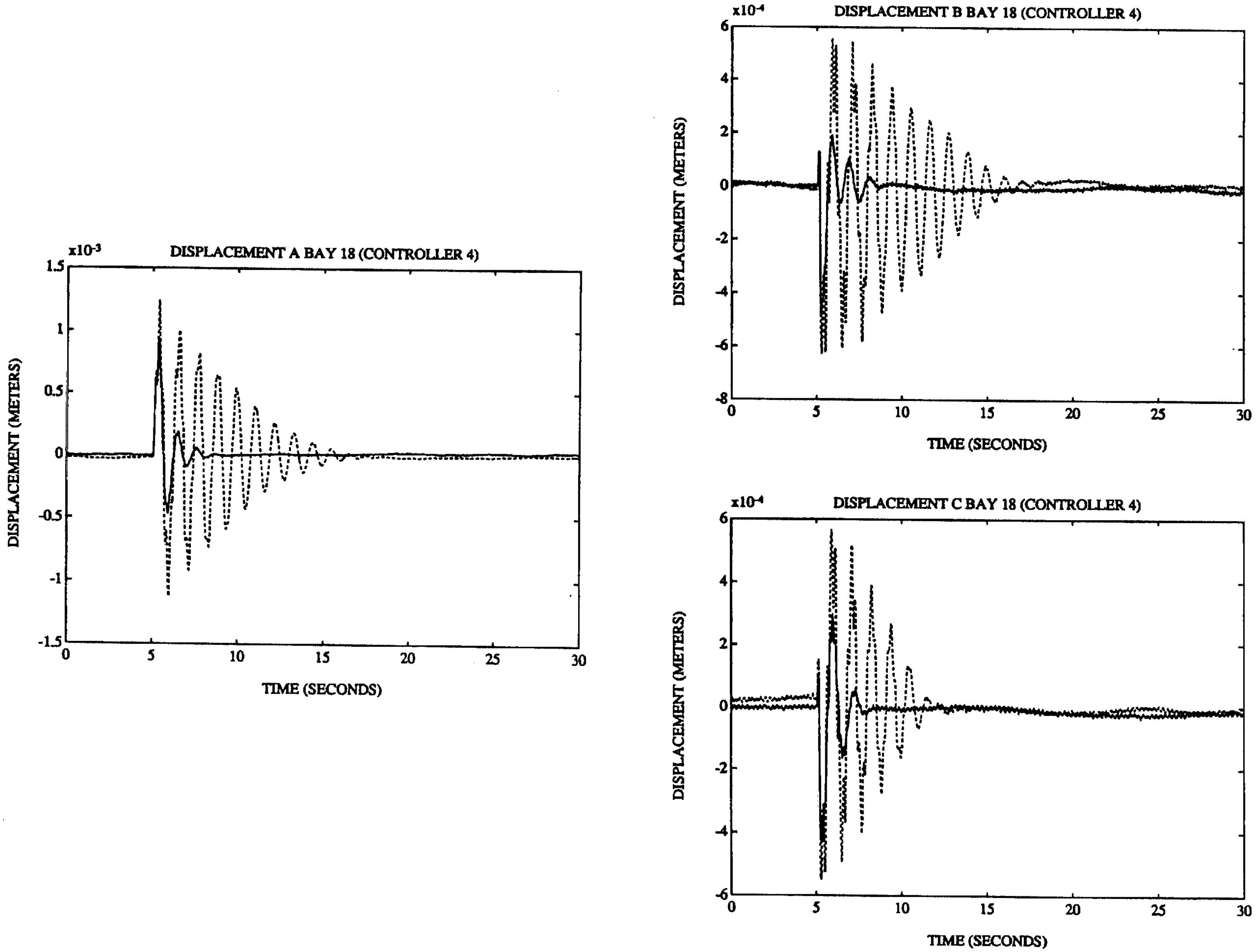

Figure 7.5 Open Loop vs. Closed Loop Bay 18 Displacement Responses for Controller 4 (Closed Loop = Solid, Open Loop = Dashed)

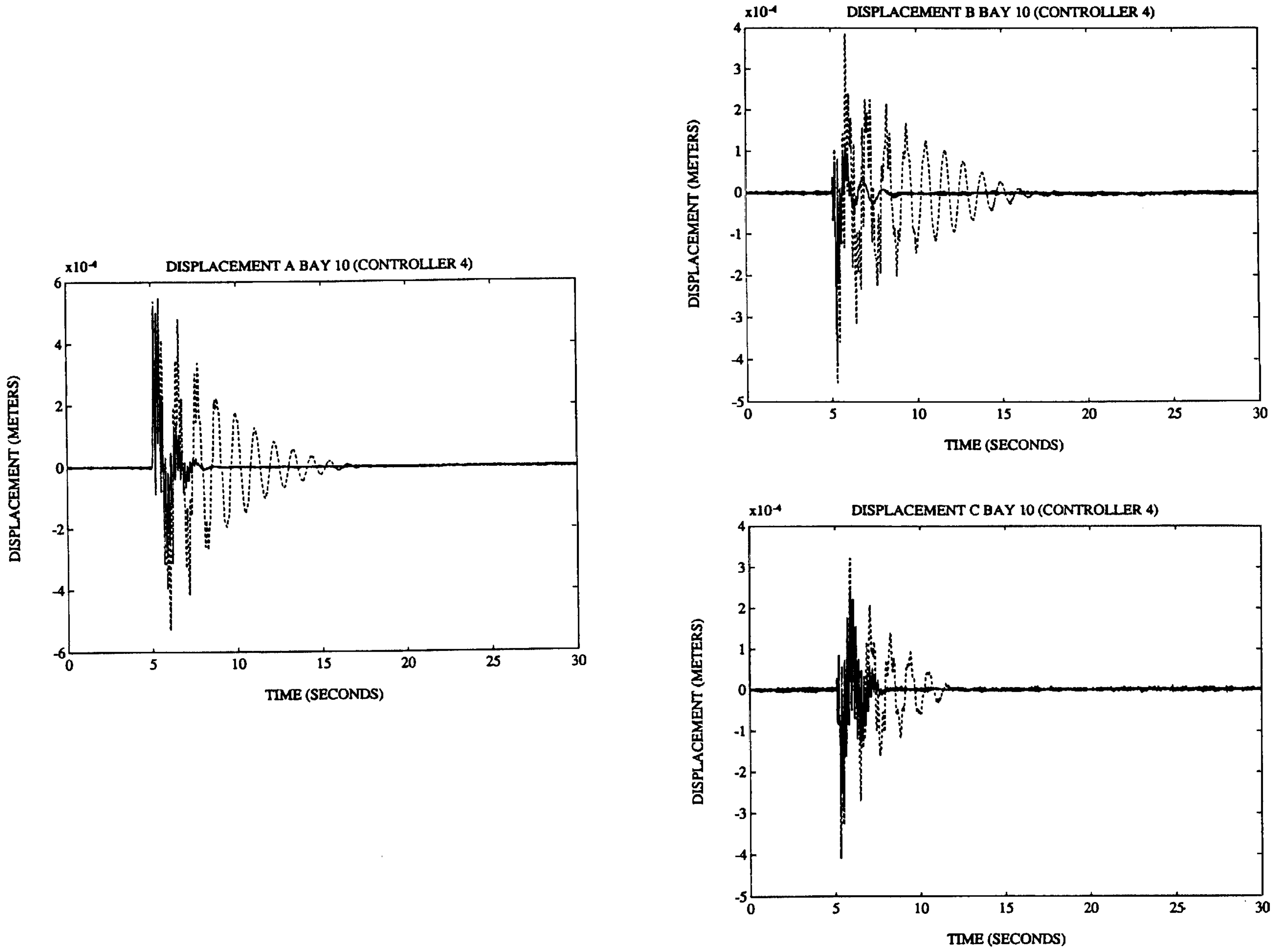

Figure 7.6 Open Loop vs. Closed Loop Bay 10 Displacement Responses for Controller 4 (Closed Loop = Solid, Open Loop = Dashed)

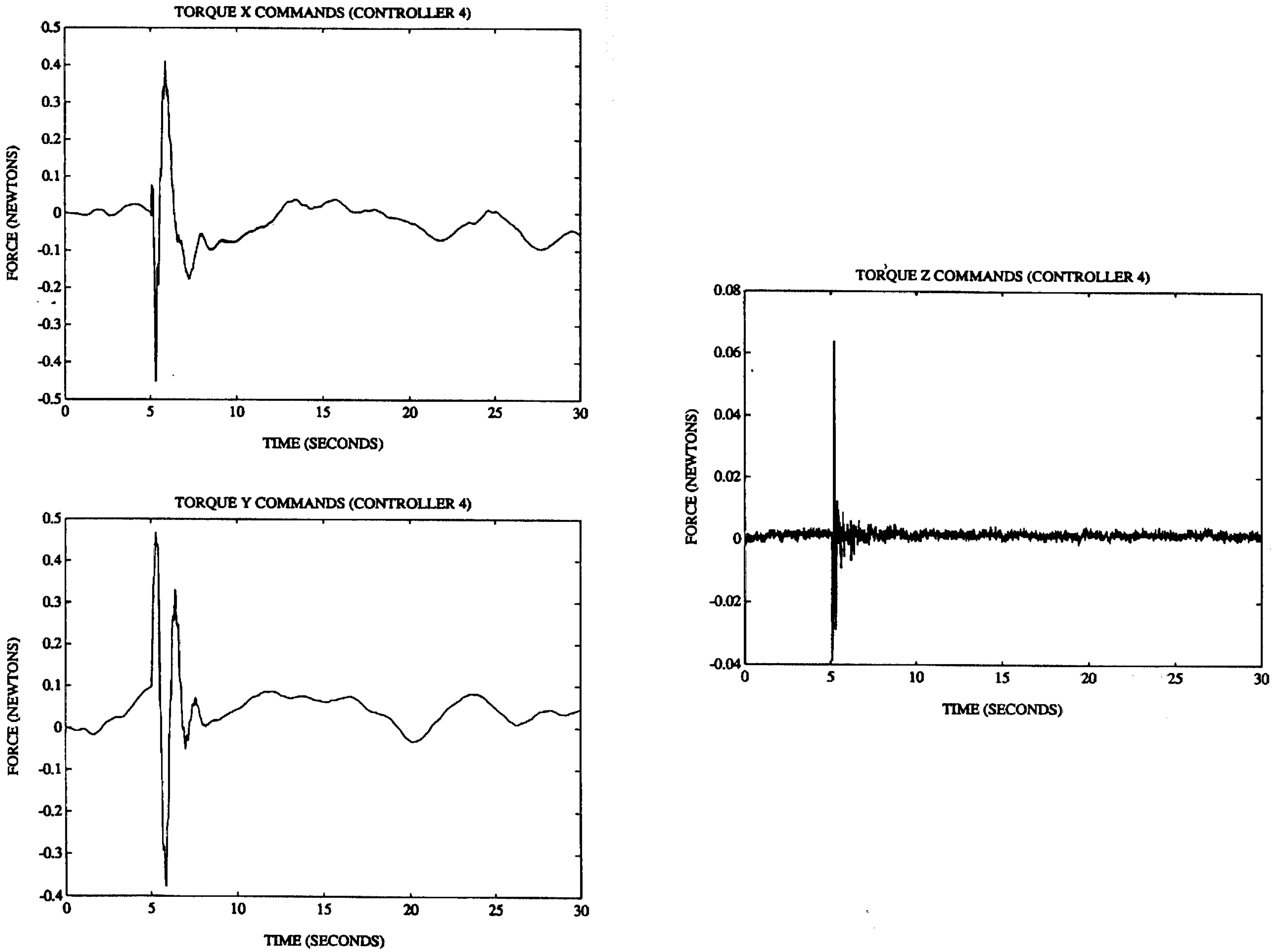
TORQUE X COMMANDS (CONTROLLER 4)

TORQUE Y COMMANDS (CONTROLLER 4)

TORQUE Z COMMANDS (CONTROLLER 4)

Figure 7.7 Closed Loop Commands to the Torque Wheels for Controller 4

The experimental and predicted open and closed loop responses of Displacement A of Bay 18 for Controllers 1, 2, 3 and 4 are shown in the next two figures.

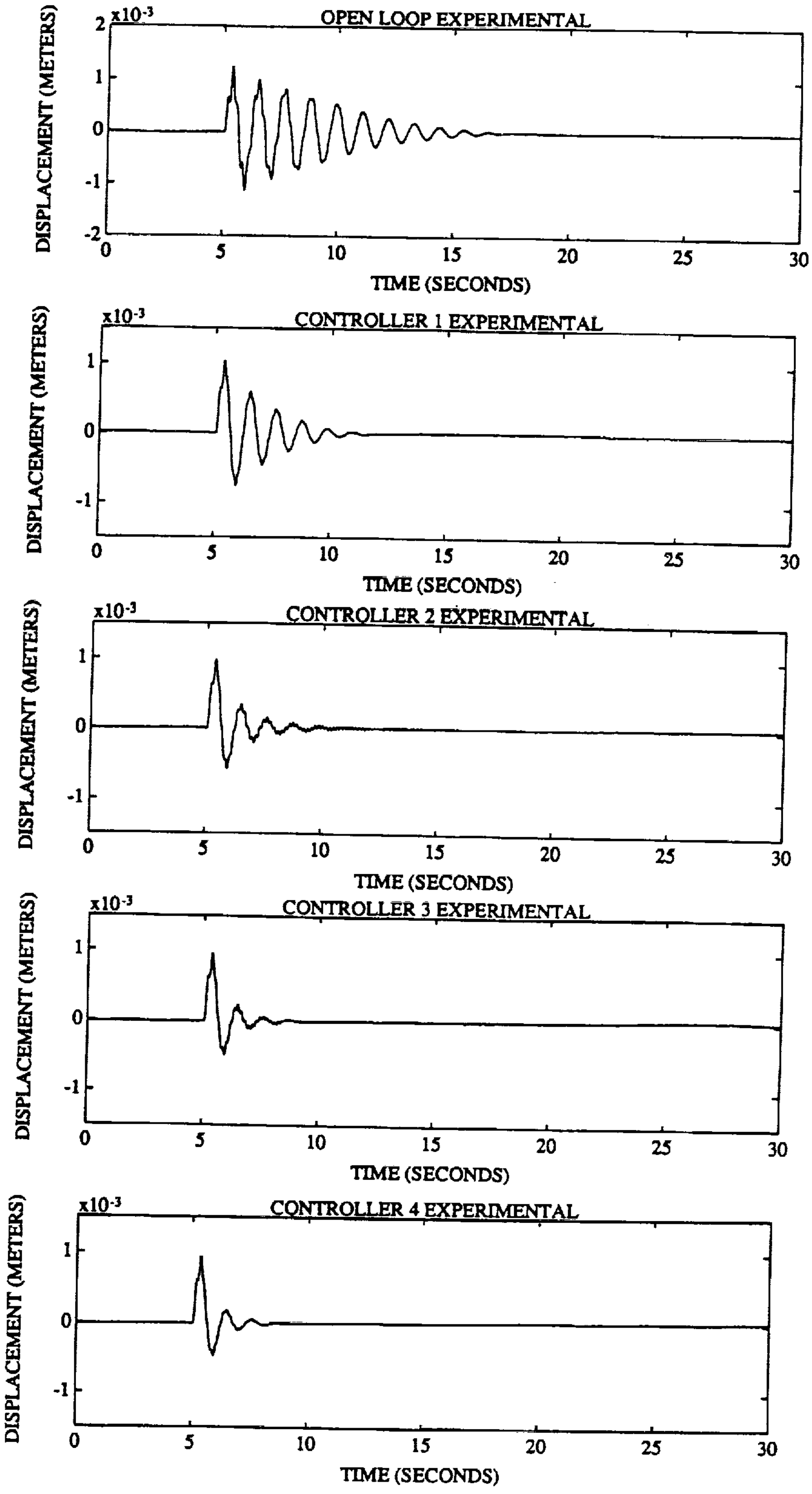

Figure 7.8 **Open and Closed Loop Responses of Displacement A of Bay 18 for Controllers 1 thru 4**

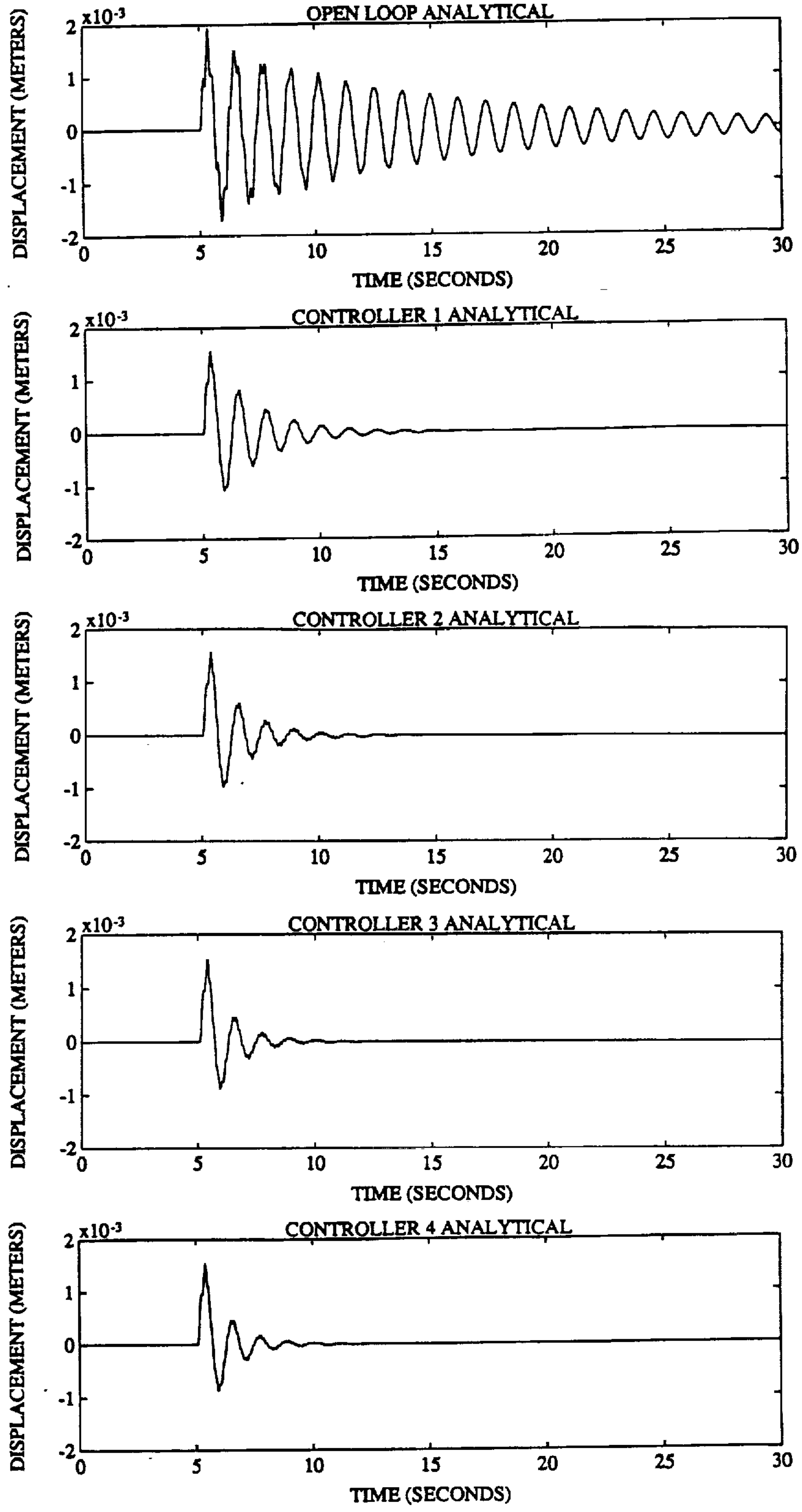

Figure 7.9 **Predicted Open and Closed Loop Responses of Displacement A of Bay 18 for Controllers 1 thru 4**

8.0 CENTRALIZED CONTROLLERS

This section further describes the centralized controllers discussed in Section 6 and presents the resultant performance improvement for each controller. Five controllers are described. As was the case for the decentralized controllers, Controllers 1 thru 4, each of these centralized controllers was designed assuming that a decentralized constant gain feedback loop from Torque-Z to Rate Gyro-Z (with gain K=10) was closed which effectively eliminated the effects of the first torsional mode.

Each of the five controllers was designed using the precompensation methodology of Section 6 with precompensation dynamics given by (6.2) and (6.3). The design weights are given by (6.4) with α and β being the design parameters. The first two centralized controllers, Controllers 5 and 6, feed back Accelerometers-2Y and 1X to Torques-X and Y. Controller 6 is essentially a robustified version of Controller 5. Controllers 7 thru 9 also feedback Accelerometers-Y and X to Torques-X and Y. Neither of these latter three controllers was designed assuming uncertainty in the first five modes. The difference in these controllers was due to the amount of performance penalty that was placed on the displacements at Bay 10.

It is of interest to note that although the centralized controllers were designed assuming 20 Hz Bessel filters to process the sensor outputs, each of the controllers was originally inadvertently implemented with 10 Hz Bessel filters which provided substantial phase delay in the controller bandwidth. Nevertheless each controller was able to stabilize the system and obtain substantial performance improvement after the controller gain was reduced by a factor of 2. In addition, two of the controller, Controllers 7 and 8 were stabilizing without reducing their gain.

8.1 Controller 5: A Reduced-Order LQG Controller Using Bay 18 Accelerometers

This controller was the least complex centralized controller that we implemented and was designed to feed back Accelerometers-2Y and 1X to Torques-X and Y. The displacements at Bay 10 were not penalized in the design process (i.e., beta=0 in (6.4)). No uncertainty was assumed in the first five modes. The controller is of order 26 and the open loop vs. closed loop Bay 18 displacement responses are shown in Figure 8.1. By comparing this figure with Figure 7.5, it is seen that the performance of this compensator, which uses two sensors, is comparable to the performance of Controller 4, a decentralized controller which uses 4 sensors and has better performance than the decentralized controllers using only the two sensors employed by Controller 5.

8.2 Controller 6: A Reduced-Order Maximum Entropy Controller Using Bay 18 Accelerometers

This controller is a robustified version of Controller 5 and is also of order 26. It was designed assuming uncertainty in the second bending mode pair. The open loop vs. closed loop Bay 18 displacement responses are shown in Figure 8.2. The performance was essentially the same as that of the performance of Controller 5, shown in Figure 8.1.

8.3 Controller 7: A Reduced-Order LQG Controller Using Bay 10 and Bay 18 Accelerometers

This controller was designed to feed back Accelerometers-2Y, 1X, X and Y to Torques-X and Y. The displacements at Bay 10 were not penalized in the design process (i.e., $\beta = 0$ in (6.4)) and no uncertainty was assumed in the first five modes. The controller was of order 25. The open loop vs. closed loop Bay 18 displacement responses are shown in Figure 8.3. By comparing this figure with Figure 7.5, which shows the performance of Controller 4, it is seen that this centralized controller yielded significantly better performance than the highest performance obtained by a decentralized controller.

8.4 Controller 8: Another Reduced-Order LQG Controller Using Bay 10 and Bay 18 Accelerometers

This controller used the same sensors and actuators as Controller 7 and also assumed no uncertainty in the first five modes. However, the controller did penalize the displacements at Bay 10. In particular, β and α in (6.4) were chosen such that $\beta/\alpha = 2$ in an attempt to further attenuate the second bending mode contribution to the displacement responses at Bay 18. The controller is of order 31 and the open loop vs. closed loop Bay 18 displacement responses are shown in Figure 8.4. By comparing this figure with Figure 8.3, it is seen that the closed-loop responses for Controller 8 were slightly better than those seen for Controller 7.

8.5 Controller 9: A Final Reduced-Order LQG Controller Using Bay 10 and Bay 18 Accelerometers

This controller used the same four sensors and two actuators as Controllers 7 and 8. The design process was essentially identical to that of Controller 8 except that α and β in (6.4) were chosen so that $\beta/\alpha = 5$. The controller is of order 33 and the open loop vs. closed loop Bay 18 displacement responses are shown in Figure 8.5. The corresponding displacement responses at Bay 10 are shown in Figure 8.6 while the commands to the torque wheels are shown in Figure 8.7. This controller yielded the best performance of any of the decentralized or centralized controllers that were implemented.

The increasing performance improvement of Controller 4 (the highest performance decentralized controller) and Controllers 5, 7 and 9 is shown in Figure 8.8 by viewing the response of Displacement-A of Bay 18. The predicted performance of these three controllers is shown in Figure 8.9. The close correspondence of these two figures is largely due to the high fidelity of the models provided by NASA Langley in the control bandwidth and is also partially due to the robustness of the implemented compensators. The gains of Controller 9 are given in the Appendix.

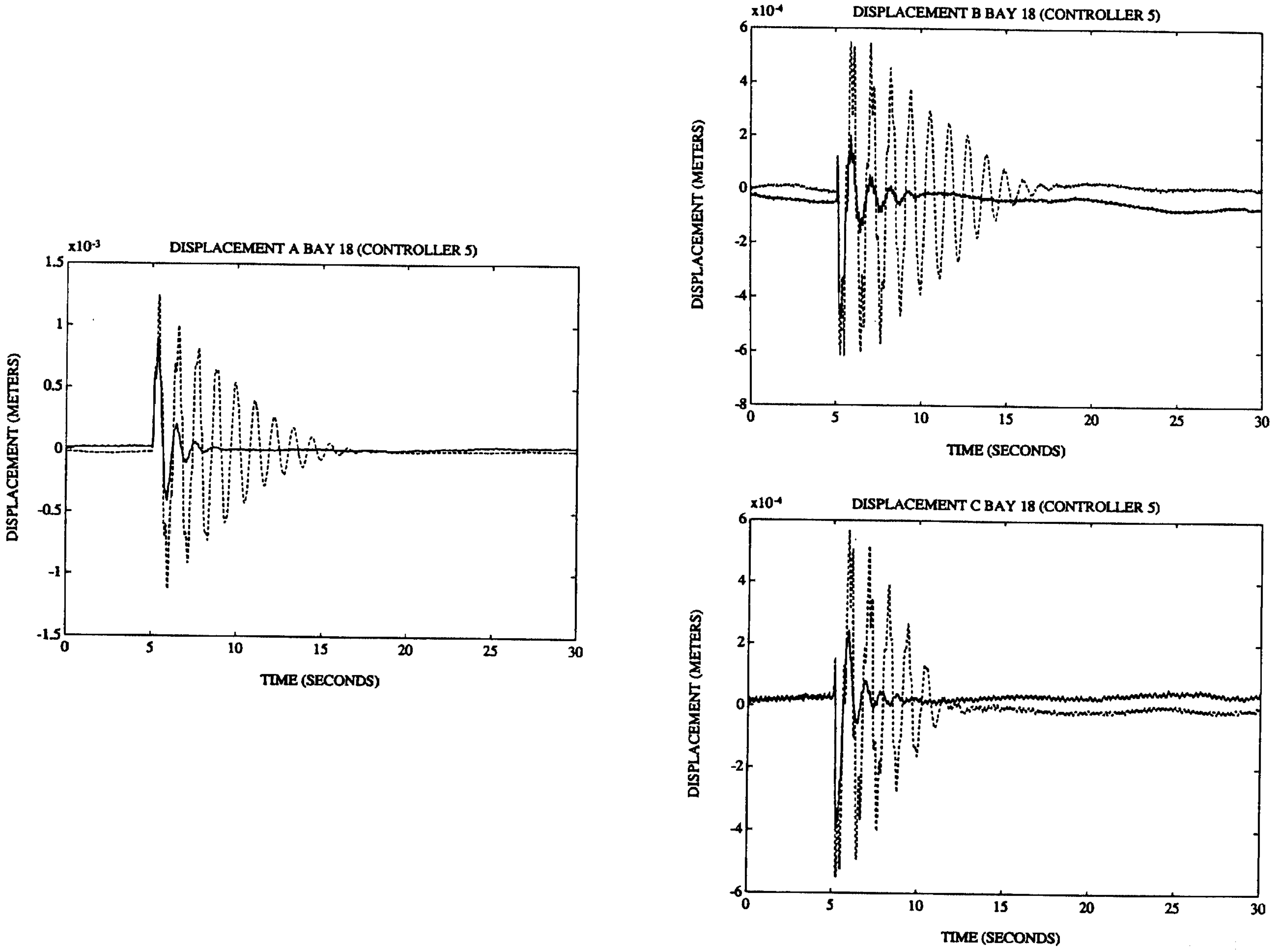

Figure 8.1 Open Loop vs. Closed Loop Bay 18 Displacement Responses for Controller 5 (Closed Loop = Solid, Open Loop = Dashed)

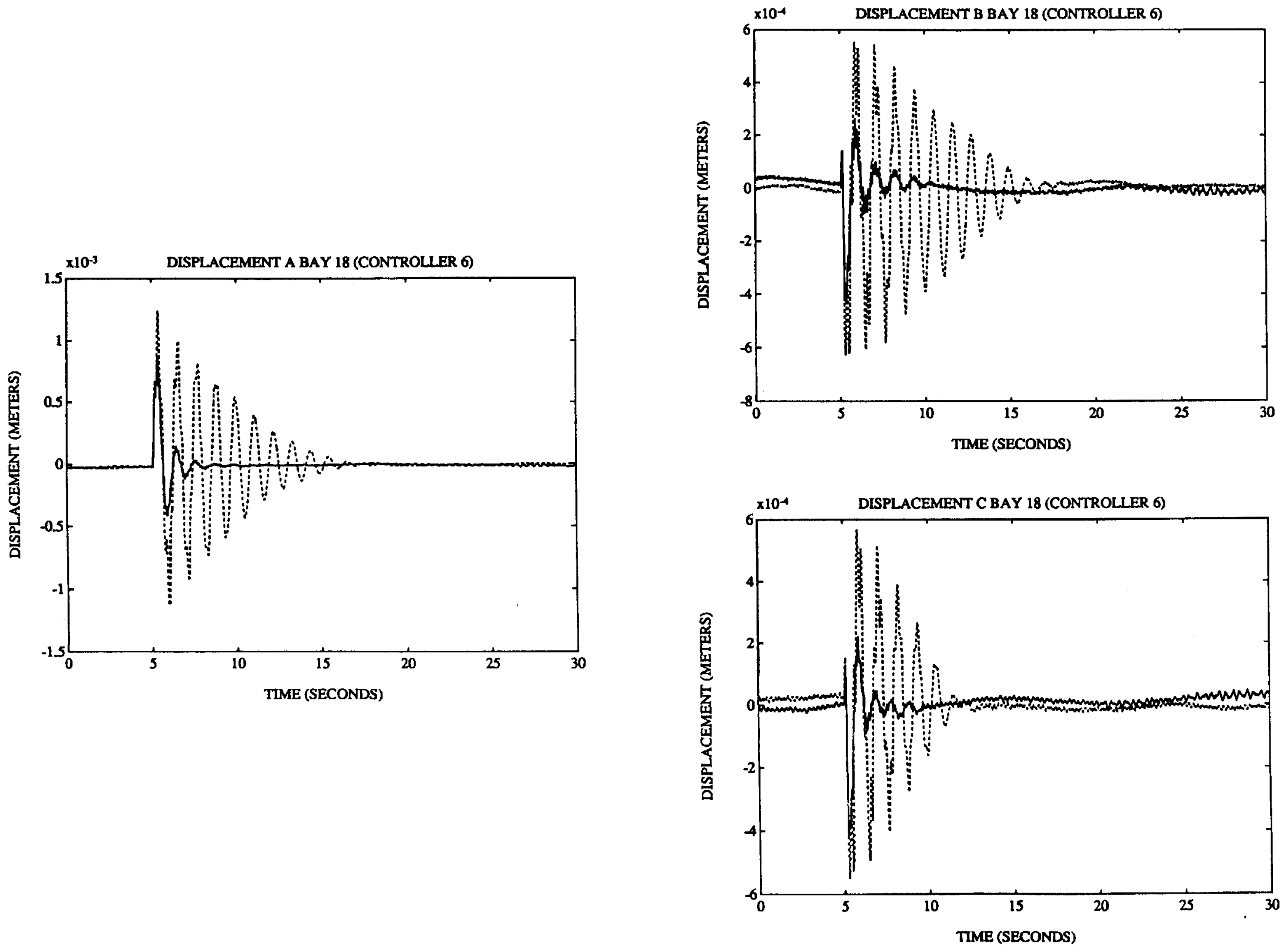

Figure 8.2 Open Loop vs. Closed Loop Bay 18 Displacement Responses for Controller 6 (Closed Loop = Solid, Open Loop = Dashed)

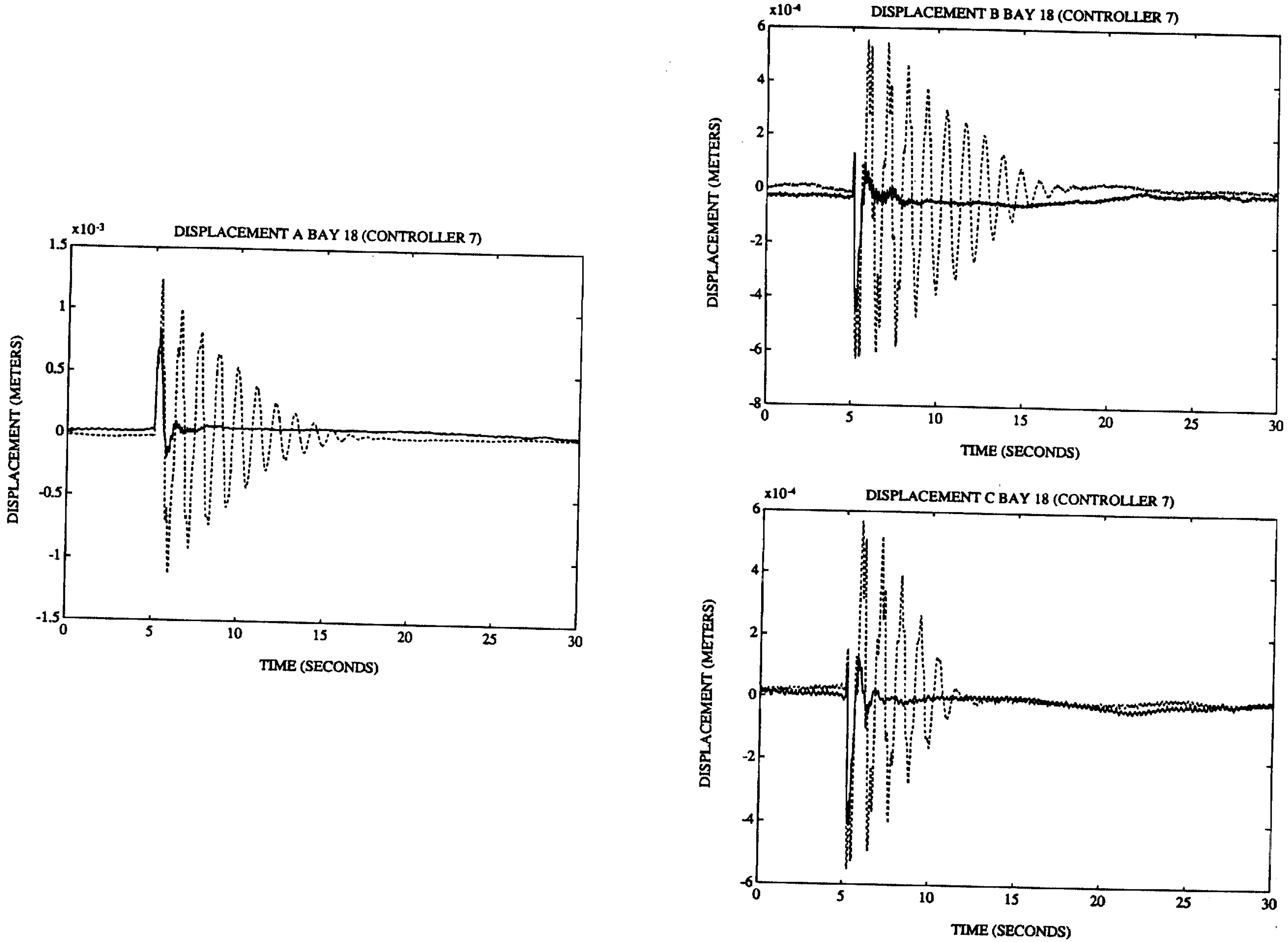

Figure 8.3 Open Loop vs. Closed Loop Bay 18 Displacement Responses for Controller 7 (Closed Loop = Solid, Open Loop = Dashed)

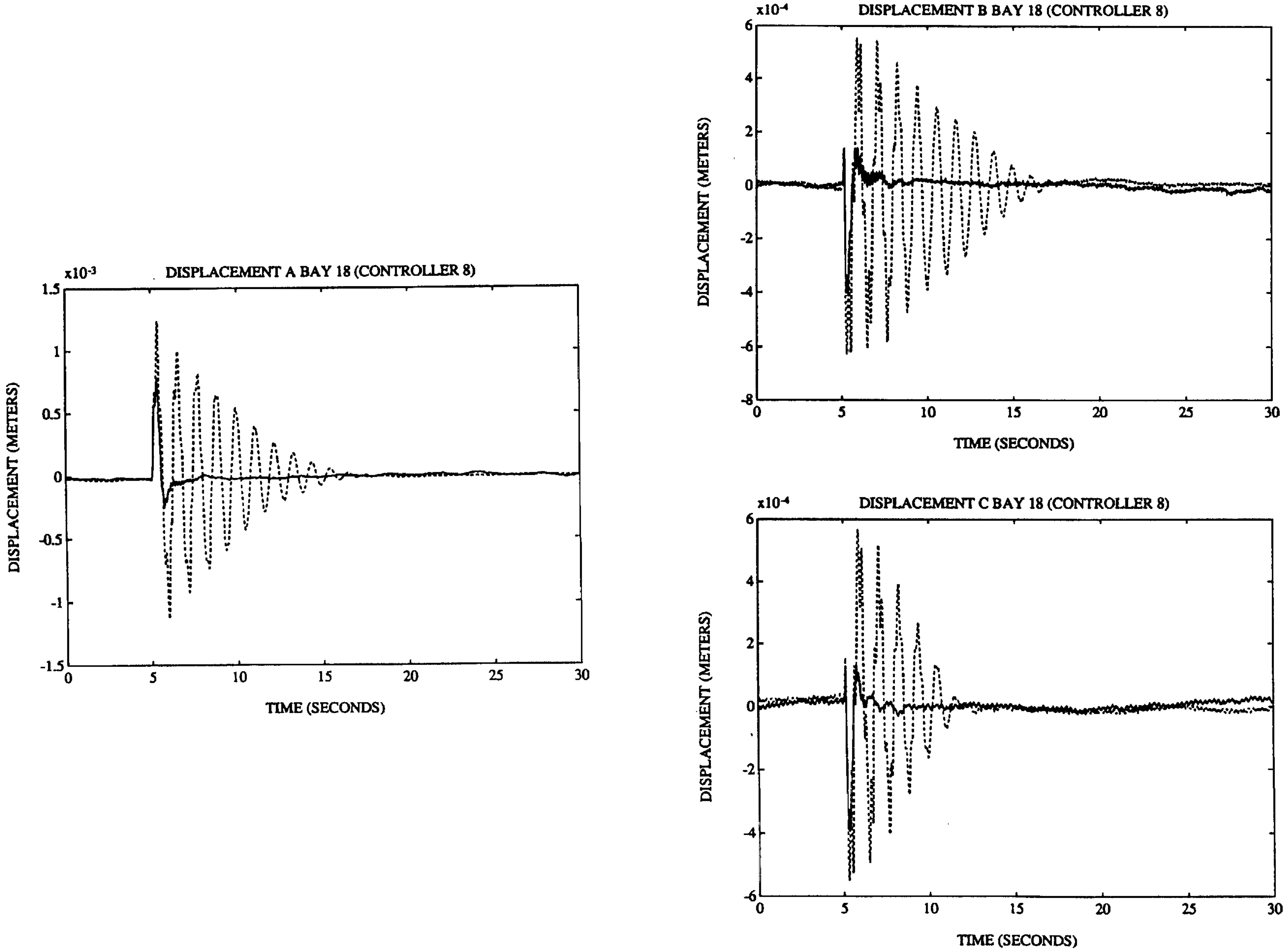

Figure 8.4 Open Loop vs. Closed Loop Bay 18 Displacement Responses for Controller 8 (Closed Loop = Solid, Open Loop = Dashed)

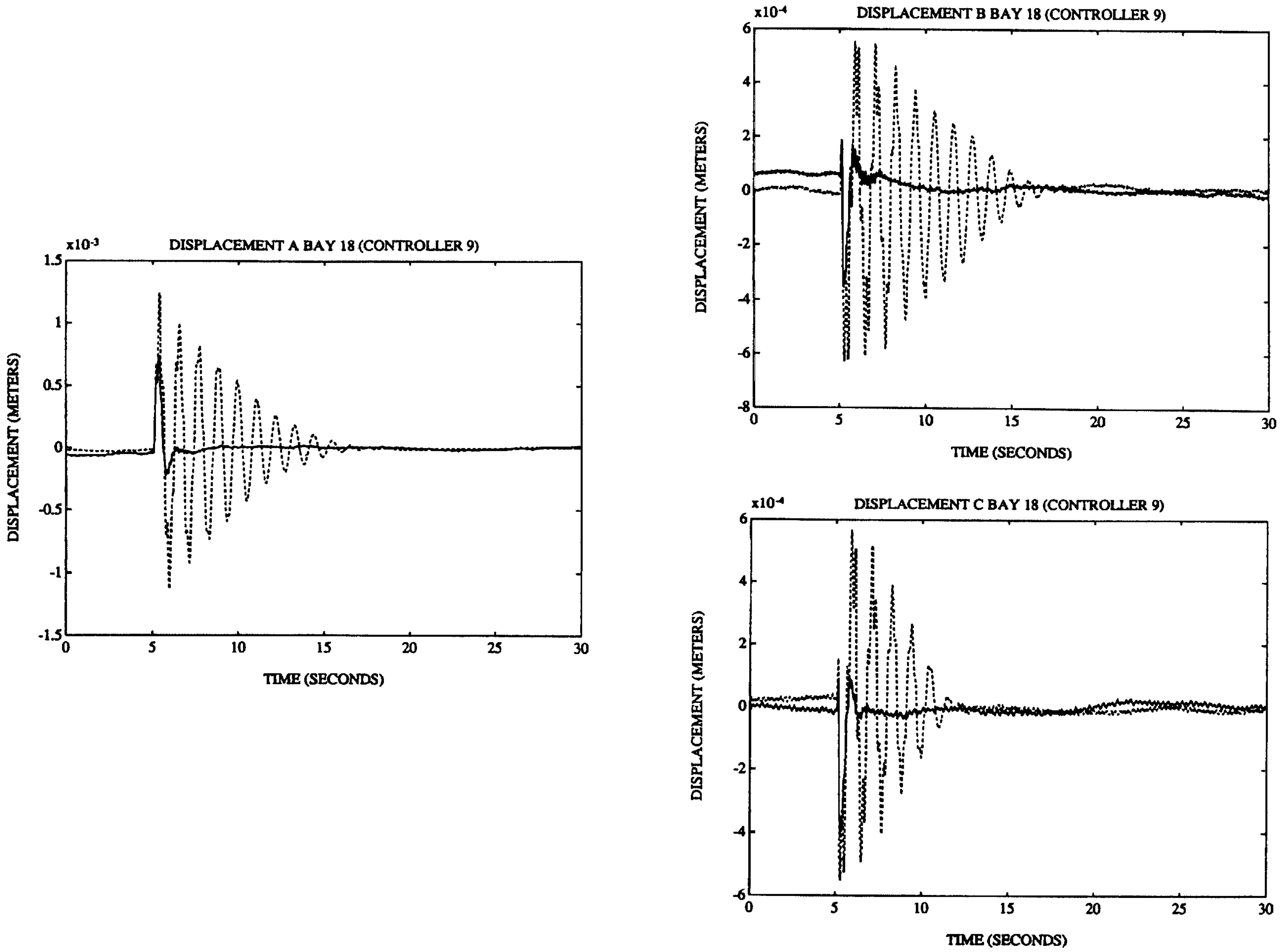

Figure 8.5 Open Loop vs. Closed Loop Bay 18 Displacement Responses for Controller 9 (Closed Loop = Solid, Open Loop = Dashed)

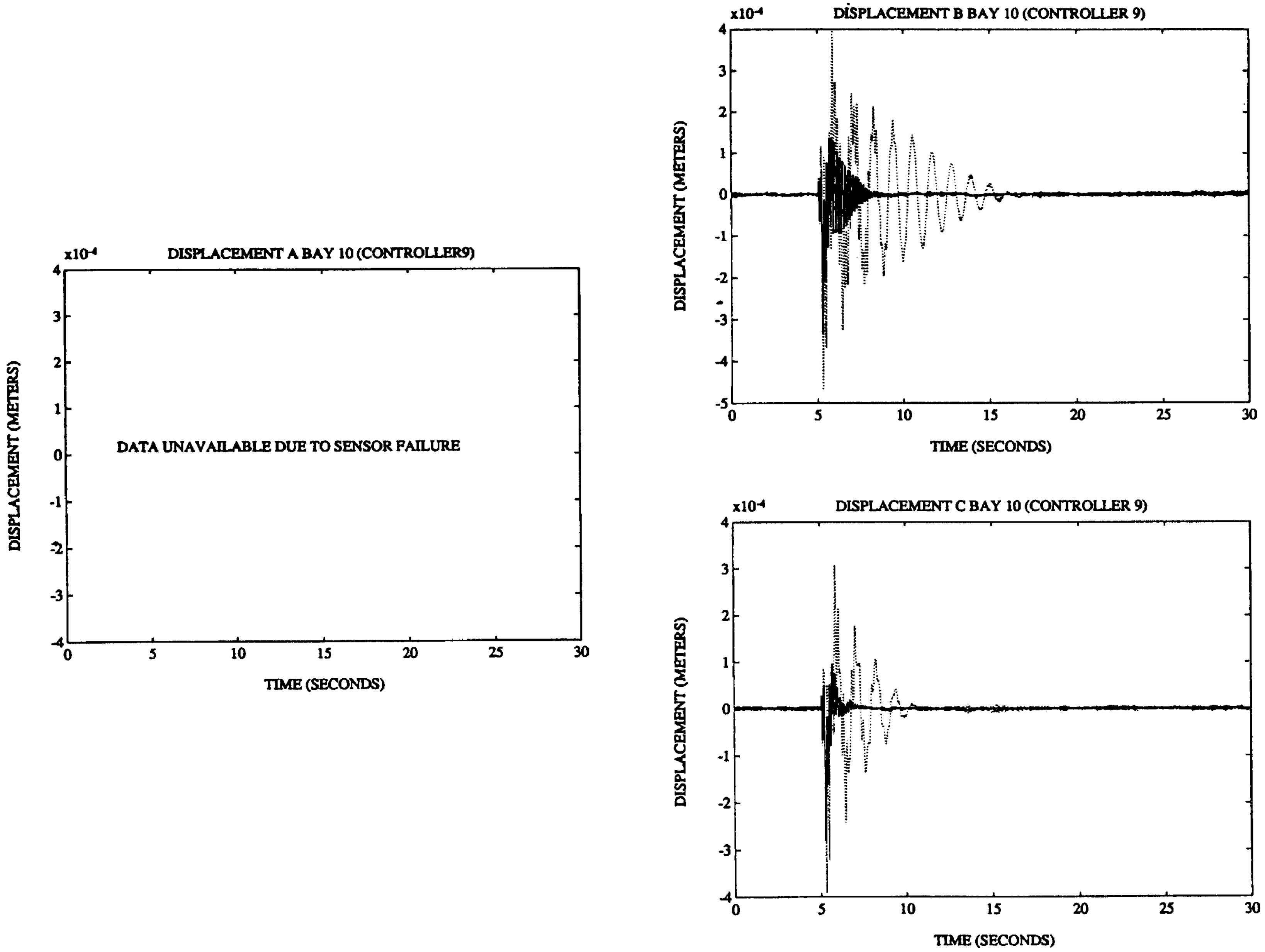

Figure 8.6 Open Loop vs. Closed Loop Bay 10 Displacement Responses for Controller 9 (Closed Loop = Solid, Open Loop = Dashed)

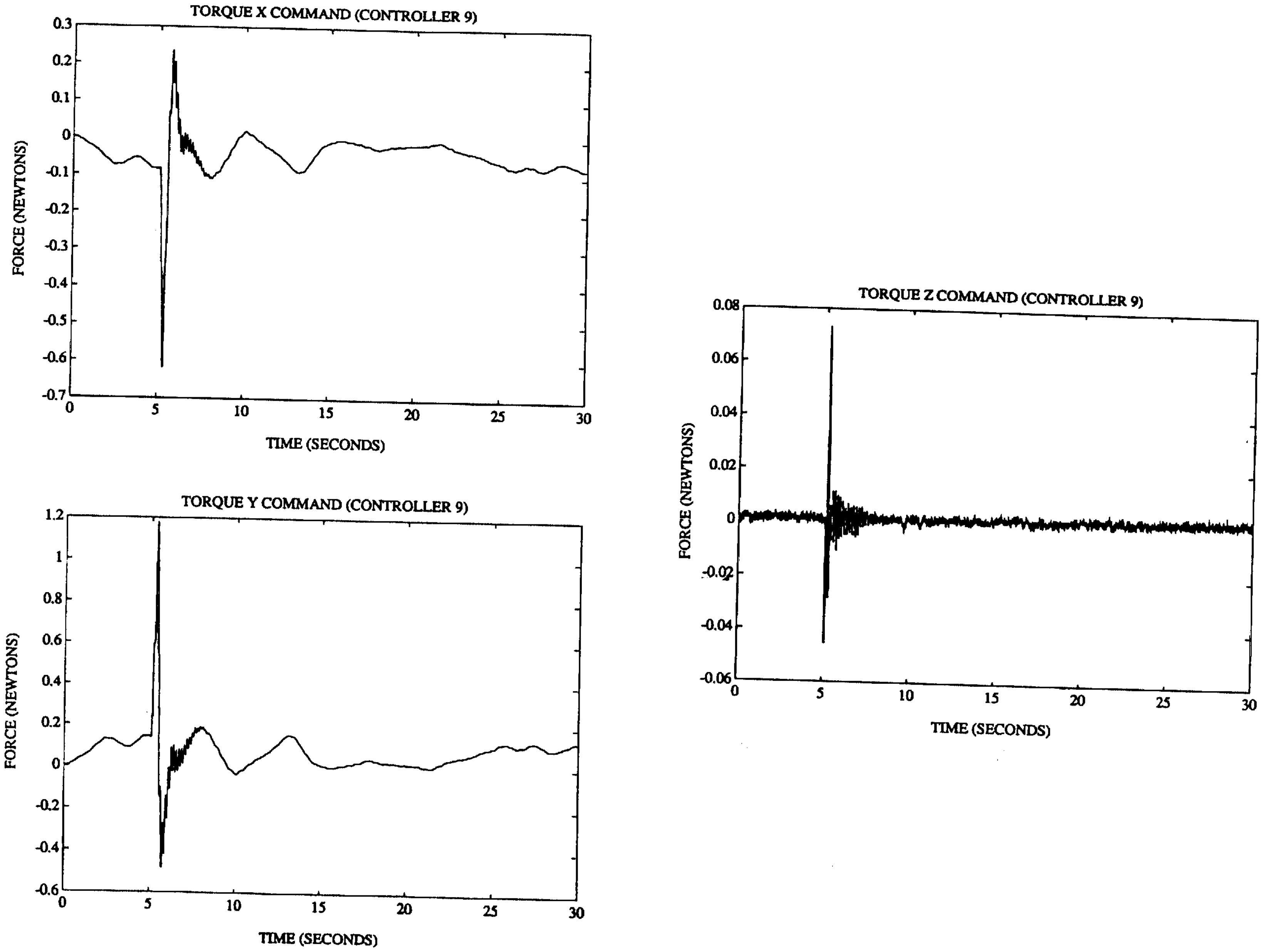

Figure 8.7 Closed Loop Commands to the Torque Wheels for Controller 9

The experimental and predicted open and closed loop responses of Displacement A of Bay 18 for Controllers 4, 5, 7 and 9 are shown in the next two figures.

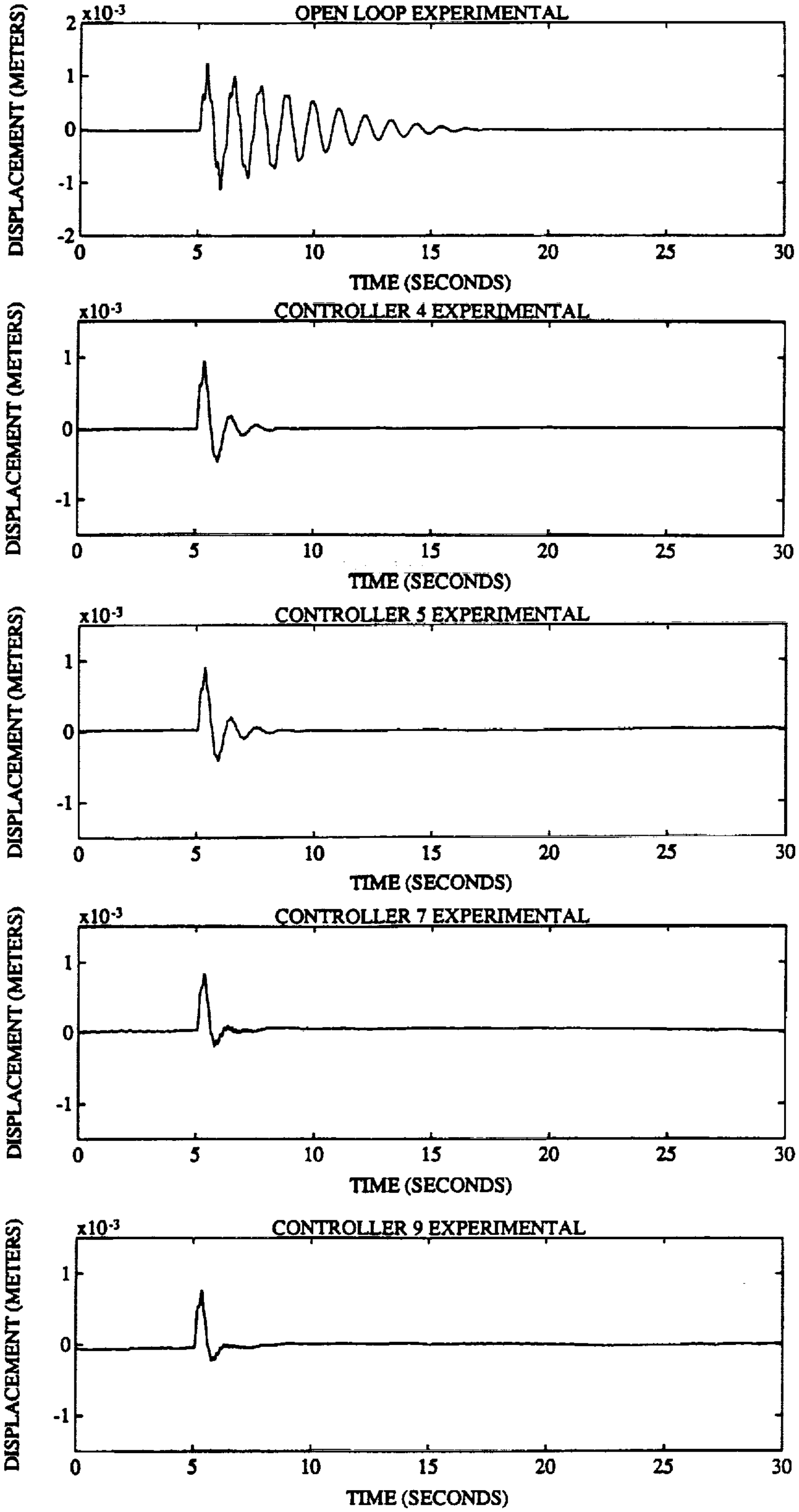

Figure 8.8 **Open and Closed Loop Responses of Displacement A of Bay 18 for Controllers 4, 5, 7, 9**

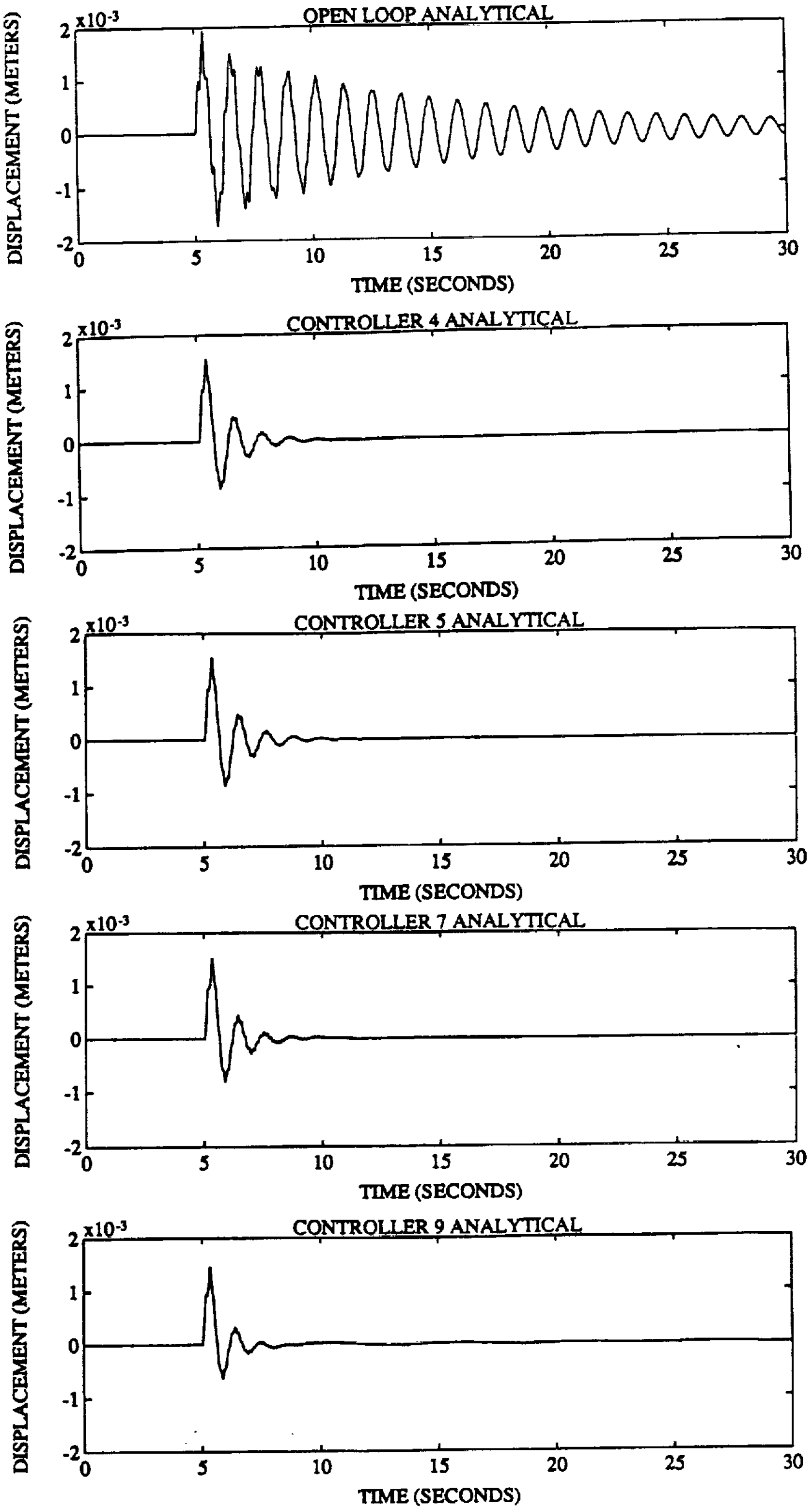

OPEN LOOP ANALYTICAL

CONTROLLER 4 ANALYTICAL

CONTROLLER 5 ANALYTICAL

CONTROLLER 7 ANALYTICAL

CONTROLLER 9 ANALYTICAL

Figure 8.9 **Predicted Open and Closed Loop Responses of Displacement A of Bay 18 for Controllers 4, 5, 7 and 9**

9.0 CLOSING REMARKS AND CONCLUSIONS

This experiment successfully demonstrated high performance control law design and implementation for the Mini-MAST testbed, a flexible structure which has features representative of future spacecraft. The controllers were designed using the Maximum Entropy/Optimal Projection approach to control design in conjunction with a precompensation methodology and thus provided validation of this strategy for control design for flexible structures.

The precompensation methodology used in this experiment allows the designer to use classical insights to precompensate the original plant model at the inputs and outputs to develop a "nice" design plant for modern control design. The precompensation is appended to the modern controller to obtain the controller that is to be implemented. In this experiment the precompensation was chosen to provide high frequency roll-off (i.e., robustness with respect to unstructured uncertainty) and was also used to make the design plant appear to have rate sensors and torque inputs. This precompensation methodology allows the designer to obtain controller configurations that are very difficult or impossible to obtain using straight-forward applications of modern control theory. We believe that this strategy will be found to have other practical uses in the future and appears to be an effective means of integrating classical control concepts with modern control.

The control design and implementation approach used was to start with simple controllers (i.e., reduced-order controllers, decentralized controllers and/or controllers using relatively few sensors and actuators) and increase controller complexity to increase performance. This strategy was effective. The first four controllers each had a decentralized structure. The first controller was our simplest and did achieve some performance improvement. As the complexity of the controllers was increased by first adding order and then using additional sensors and controller order, the performance progressively improved. The performance was further improved by allowing the controllers to have a centralized structure.

The results of this experiment and the Harris Guest Investigator experiment on the ACES structure [1,2] also illustrate that decentralized controllers and/or reduced-order controllers can provide very significant performance improvement for some flexible structure control problems. Controller simplicity is very important for the development of practical controllers due to substantial limits on throughput capability of even the most advanced space-qualified processors.

The controllers in this experiment were designed to control the first five modes of the Mini-

MAST structure. The models provided by NASA Langley were quite accurate for these five modes and thus robustness within the controller bandwidth was not a real issue in this experiment as it was in the ACES experiment [1,2]. However, as already mentioned, the precompensation methodology was effective in providing the needed robustness for the higher frequency modes.

The Harris team's experience in the NASA CSI Guest Investigator program and in implementing controllers on Harris testbeds [24] leads to the following recommendations for future flight experiments.

1. Design the structure to allow decentralized control design (even if centralized controllers can yield better performance).
2. Using the best model available without in-flight system identification, design highly robust decentralized controllers as the first controllers to be implemented.
3. Design the mission to allow in-flight system identification using a proven identification tool such as the Eigensystem Realization Algorithm [25,26].
4. Using the system identification model, design a sequence of controllers of increasing complexity and potential performance improvement.
5. Sequentially implement the sequence of controllers. If instability is sensed, then revert back to a controller that is known to be stabilizing.

These steps should only be viewed as a rough outline. Many variations of this scheme are of course possible.

Finally, one possible improvement is recommended in what is considered to be a very successful CSI Guest Investigator Program. It is recommended that future phases of this program be structured to allow controllers to be implemented without requiring a guest investigator to be on-site. This would save the program significant cost and could thus allow more time for actual control design and analysis which would ultimately benefit NASA.

Acknowledgements. We thank Dr. Keith Belvin, Anne Bruner, Sharon Tanner, Jeff Sulla and David Geyer for their cooperation during this project. Without them this project would not have been successful.

10.0 References

1. E. G. Collins, Jr., D. J. Phillips, and D. C. Hyland, "Design and Implementation of Robust Decentralized Control Laws for the ACES Structure at the Marshall Space Flight Center," *Proc. Amer. Contr. Conf.*, pp. 1449–1454, San Diego, CA, May 1990.(Also see the NASA Report of the same title. NASA Contractor Report 4310, Langley Research Center , July 1990.)
2. E. G. Collins, Jr., D. J. Phillips, and D. C. Hyland "Robust Decentralized Control Laws for the ACES Structure," *Contr. Sys. Mag.*, pp. 62-70, April, 1991.
3. D. C. Hyland, "Minimum Information Stochastic Modelling of Linear Systems with a Class of Parameter Uncertainties," *Proc. Amer. Contr. Conf.*, pp. 620–627, Arlington, VA, June 1982.
4. D. C. Hyland, "Maximum Entropy Stochastic Approach to Controller Design for Uncertain Structural Systems," *Proc. Amer. Contr. Conf.*, pp. 680–688, Arlington, VA, June 1982.
5. D. C. Hyland and D. S. Bernstein, "The Optimal Projection Equations for Fixed-Order Dynamic Compensation," *IEEE Trans. Autom. Contr.*, Vol. AC–29, pp. 1034–1037, 1984.
6. D. S. Bernstein and D. C. Hyland, "The Optimal Projection/Maximum Entropy Approach to Designing Low-Order, Robust Controllers for Flexible Structures," *Proc. IEEE Conf. Dec. Contr.*, pp. 745–752, Fort Lauderdale, FL. December 1985.
7. D. S. Bernstein and S. W. Greeley, "Robust Controller Synthesis Using the Maximum Entropy Design Equations," *IEEE Trans. Autom. Contr.*, Vol. AC–31, pp. 362–364, 1986.
8. S. Richter and E. G. Collins, Jr., "A Homotopy Algorithm for Reduced Order Compensator Design Using the Optimal Projection Equations," *Proc. 28th IEEE Conf. Decis. Contr.*, pp. 506–511, Tampa, FL, Dec. 1989.
9. E. G. Collins, Jr., and S. Richter, "A Homotopy Algorithm for Synthesizing Robust Controllers for Flexible Structures Via the Maximum Entropy Design Equations," *Third Air force/NASA Symposium on Recent Advances in Multidisciplinary Analysis and Optimization,* pp. 324–333, San Francisco, CA, September 1990.
10. D. S. Bernstein and D. C. Hyland, "Optimal Projection for Uncertain System (OPUS): A Unified Theory of Reduced-Order, Robust Control Design," in *Large Space Structures: Dynamics and Control,* S. N. Atluri and A. K. Amos, eds., Springer-Verlag, New York, 1988.
11. D. S. Bernstein and D. C. Hyland, "The Optimal Projection Approach to Robust, Fixed-Structure Control Design," *Mechanics and Control of Space Structures,* J. L. Junkins, Ed., AIAA Publication, 1990, pp. 237-293, 1990.
12. R. Pappa, et al., *Mini-MAST CSI Testbed User's Guide,* NASA Langley Research Center, March 1989.
13. A. Yousuff and R. E. Skelton, "A Note on Balanced Controller Reduction," *IEEE Trans. Autom. Contr.*, Vol. AC–29, pp. 254–256, 1984.
14. B. A. Francis, "A Course in H^∞ Control Theory," *Lecture Notes in Control and Information Sciences,* Vol. 88, Springer-Verlag, 1987.
15. B. A. Francis and J. C. Doyle, "Linear Control Theory with an H_∞ Optimality Criterion,"

SIAM J. Contr. Opt., Vol. 25, pp. 815–844, 1987.

16. J. C. Doyle, K. Glover, P. P. Khargonekar and B. A. Francis, "State-Space Solutions to Standard H_2 and H_∞ Control Problems," *IEEE Trans. Autom. Contr.*, Vol. AC–34, 1989.

17. D. S. Bernstein, "LQG Control with an H_∞ Performance Bound: A Riccati Equation Approach," *IEEE Trans. Autom. Contr.*, Vol. 34, pp. 293–305, 1989.

18. J. A. King and R. D. Irwin, "Issues in the Application of H_∞ Control to Large Space Structures," *Proc. Southeastern Symposium on System Theory,* Cookeville, TN, March 1990.

19. P. G. Clar, A. Carrier, and A. E. Bryson, Jr., "Comparison of Two Methods for Causing Roll-Off in Control System Design," *AIAA Guid. Nav. Contr. Conf.*, pp. 1734–1741, August 1990.

20. J. C. Doyle, "Structured Uncertainty in Control System Design," *Proc. IEEE Conf. Decis. Contr.* pp. 260–265, December 1985.

21. G. J. Balas, C.-C. Chu, and J. C. Doyle, "Vibration Damping and Robust Control of the JPL/AFAL Experiment Using μ-Synthesis," *Proc. IEEE Conf. Decis. Contr.*, pp. 2689–2694, December 1989.

22. N. K. Gupta, "Frequency-Shaped Cost Functionals: Extension of Linear-Quadratic-Gaussian Design Methods," *J. Guid. Contr.*, Vol. 3, 1980.

23. R. D. Hefner and D. L. Mingori, "Suboptimal Controller Design Using Frequency Domain Constraints," *Proc. AIAA Guid. Contr. Conf.*, August 1982.

24. D. J. Phillips, E. G. Collins, Jr., and D. C. Hyland, "Experimental Demonstrations of Active Vibration Control of Flexible Structures," *Proc. IEEE Conf. Dec. Contr.*, pp. 2024–2029, Honolulu, HI, December 1990.

25. J. N. Juang and R. S. Pappa, "An Eigensystem Realization Algorithm for Modal Parameter Identification and Model Reduction," *J. Guid. Contr. Dyn.*, Vol. 8, pp. 620–627, 1985.

26. J. N. Juang and R. S. Pappa, "Effects of Noise on Modal Parameters Identified by the Eigensystem Realization Algorithm," *J. Guid. Contr. Dyn.*, Vol. 9, pp. 294–303, 1986.

11.0 APPENDIX CONTROL GAINS FOR CONTROLLERS 4 AND 9

This Appendix presents the gains of Controllers 4 and 9. It is assumed that each control law is of the form

$$x_c(k+1) = A_c x_c(k) + B_c y(k)$$
$$u(k) = C_c x_c(k) + D_c y(k).$$

In addition the gains are presented in a basis in which the controller state matrix A_c is in real normal form, i.e.,

$$A_c = \text{block-diag}\{A_c, i\}_{i=1}^{m}$$

where

$$A_{c,i} = -\nu_i \text{ or } A_{c,i} = \begin{bmatrix} -\nu_i & \omega_i \\ -\omega_i & -\nu_i \end{bmatrix}$$

and $M \leq n_c$ denotes the number of blocks.

Controller 4 $(\mathbf{A_{c4}}, \mathbf{B_{c4}}, \mathbf{C_{c4}}, \mathbf{D_{c4}})$

Description of Blocks of A_{c4}

i	size of $A_{c,i}$	ν_i	ω_i
1.0000000e+00	1.0000000e+00	0.0000000e+00	0.0000000e+00
2.0000000e+00	2.0000000e+00	6.9363938e-01	7.1484760e-02
3.0000000e+00	1.0000000e+00	8.1194223e-01	0.0000000e+00
4.0000000e+00	1.0000000e+00	9.2446525e-01	0.0000000e+00
5.0000000e+00	1.0000000e+00	9.2446525e-01	0.0000000e+00
6.0000000e+00	1.0000000e+00	9.2446525e-01	0.0000000e+00
7.0000000e+00	1.0000000e+00	9.3841864e-01	0.0000000e+00
8.0000000e+00	2.0000000e+00	8.5729796e-01	4.4416701e-01
9.0000000e+00	1.0000000e+00	9.6673736e-01	0.0000000e+00
1.0000000e+01	1.0000000e+00	9.8068783e-01	0.0000000e+00
1.1000000e+01	2.0000000e+00	8.7268108e-01	4.5172409e-01
1.2000000e+01	2.0000000e+00	2.0521210e-01	9.7180085e-01
1.3000000e+01	2.0000000e+00	2.0078435e-01	9.7505991e-01
1.4000000e+01	1.0000000e+00	9.9605972e-01	6.7716165e-03
1.5000000e+01	1.0000000e+00	9.9605972e-01	0.0000000e+00
1.6000000e+01	1.0000000e+00	9.9605972e-01	6.7716165e-03
1.7000000e+01	2.0000000e+00	9.9605972e-01	0.0000000e+00
1.8000000e+01	1.0000000e+00	9.9993376e-01	0.0000000e+00

$$B_{c4} = \begin{bmatrix}
0.0000000e+00 & 0.0000000e+00 & 0.0000000e+00 & 0.0000000e+00 & 0.0000000e+00 \\
-4.7831567e+01 & 0.0000000e+00 & 0.0000000e+00 & 0.0000000e+00 & 0.0000000e+00 \\
-2.0131695e+02 & 0.0000000e+00 & 0.0000000e+00 & 0.0000000e+00 & 0.0000000e+00 \\
0.0000000e+00 & 2.1982125e+02 & 0.0000000e+00 & 0.0000000e+00 & 0.0000000e+00 \\
0.0000000e+00 & 0.0000000e+00 & 0.0000000e+00 & 2.0000000e-01 & 0.0000000e+00 \\
0.0000000e+00 & 0.0000000e+00 & 0.0000000e+00 & 0.0000000e+00 & 1.8637410e+15 \\
0.0000000e+00 & 0.0000000e+00 & 0.0000000e+00 & 0.0000000e+00 & 1.8637410e+15 \\
-2.4257444e+01 & 0.0000000e+00 & 0.0000000e+00 & 0.0000000e+00 & 0.0000000e+00 \\
-7.2516882e+00 & 0.0000000e+00 & 0.0000000e+00 & 0.0000000e+00 & 0.0000000e+00 \\
-4.3259987e+00 & 0.0000000e+00 & 0.0000000e+00 & 0.0000000e+00 & 0.0000000e+00 \\
0.0000000e+00 & 1.2230791e+03 & 0.0000000e+00 & 0.0000000e+00 & 0.0000000e+00 \\
-5.0002853e+03 & 0.0000000e+00 & 0.0000000e+00 & 0.0000000e+00 & 0.0000000e+00 \\
0.0000000e+00 & -3.5172568e+00 & 0.0000000e+00 & 0.0000000e+00 & 0.0000000e+00 \\
0.0000000e+00 & 2.8208469e+00 & 0.0000000e+00 & 0.0000000e+00 & 0.0000000e+00 \\
-1.8654961e+00 & 0.0000000e+00 & 0.0000000e+00 & 0.0000000e+00 & 0.0000000e+00 \\
2.4169305e+00 & 0.0000000e+00 & 0.0000000e+00 & 0.0000000e+00 & 0.0000000e+00 \\
0.0000000e+00 & 1.0533845e+00 & 0.0000000e+00 & 0.0000000e+00 & 0.0000000e+00 \\
0.0000000e+00 & 3.4778126e-01 & 0.0000000e+00 & 0.0000000e+00 & 0.0000000e+00 \\
0.0000000e+00 & -1.9768639e+04 & 0.0000000e+00 & 0.0000000e+00 & 0.0000000e+00 \\
-6.5121393e+05 & 0.0000000e+00 & 0.0000000e+00 & 0.0000000e+00 & 0.0000000e+00 \\
0.0000000e+00 & 2.6873032e+06 & 0.0000000e+00 & 0.0000000e+00 & 0.0000000e+00 \\
4.4661772e+06 & 0.0000000e+00 & 0.0000000e+00 & 0.0000000e+00 & 0.0000000e+00 \\
-2.0613049e+06 & 0.0000000e+00 & 0.0000000e+00 & 0.0000000e+00 & 0.0000000e+00 \\
0.0000000e+00 & -2.7080768e+06 & 0.0000000e+00 & 0.0000000e+00 & 0.0000000e+00
\end{bmatrix}$$

$$C_{c4}^{\mathrm{T}} = \begin{bmatrix}
0.0000000e+00 & 1.0000000e+00 & 0.0000000e+00 \\
9.2933761e-04 & 0.0000000e+00 & 0.0000000e+00 \\
2.1761338e-03 & 0.0000000e+00 & 0.0000000e+00 \\
0.0000000e+00 & 3.5716009e-03 & 0.0000000e+00 \\
9.2446525e-01 & 0.0000000e+00 & 0.0000000e+00 \\
0.0000000e+00 & 7.0710678e-01 & 0.0000000e+00 \\
0.0000000e+00 & -7.0710678e-01 & 0.0000000e+00 \\
-4.2322974e-03 & 0.0000000e+00 & 0.0000000e+00 \\
4.1564743e-03 & 0.0000000e+00 & 0.0000000e+00 \\
2.0288759e-03 & 0.0000000e+00 & 0.0000000e+00 \\
0.0000000e+00 & -4.9636080e-03 & 0.0000000e+00 \\
-4.5837550e-03 & 0.0000000e+00 & 0.0000000e+00 \\
0.0000000e+00 & -1.9571354e-03 & 0.0000000e+00 \\
0.0000000e+00 & 9.9648177e-04 & 0.0000000e+00 \\
2.3849235e-05 & 0.0000000e+00 & 0.0000000e+00 \\
6.2801479e-05 & 0.0000000e+00 & 0.0000000e+00 \\
0.0000000e+00 & 1.6183802e-04 & 0.0000000e+00 \\
0.0000000e+00 & 7.5593979e-05 & 0.0000000e+00 \\
0.0000000e+00 & 5.2698732e-03 & 0.0000000e+00 \\
4.7453070e-03 & 0.0000000e+00 & 0.0000000e+00 \\
0.0000000e+00 & -5.2730650e-03 & 0.0000000e+00 \\
-1.4052697e-03 & 0.0000000e+00 & 0.0000000e+00 \\
-4.5329294e-03 & 0.0000000e+00 & 0.0000000e+00 \\
0.0000000e+00 & -5.2730669e-03 & 0.0000000e+00
\end{bmatrix}$$

$$D_{c4} = \begin{bmatrix}
-4.0740356e-02 & 0.0000000e+00 & 0.0000000e+00 & 0.0000000e+00 & 0.0000000e+00 \\
0.0000000e+00 & 2.5800693e-02 & 0.0000000e+00 & 2.0000000e-01 & 0.0000000e+00 \\
0.0000000e+00 & 0.0000000e+00 & 1.0000000e+01 & 0.0000000e+00 & 0.0000000e+00
\end{bmatrix}$$

Controller 9 ($\mathbf{A}_{c9}, \mathbf{B}_{c9}, \mathbf{C}_{c9}, \mathbf{D}_{c9}$)

Description of Blocks of A_{c9}

i	size of $A_{c,i}$	ν_i	ω_i
1.0000000e+00	1.0000000e+00	7.7466103e-05	0.0000000e+00
2.0000000e+00	2.0000000e+00	4.8671387e-02	2.5217382e-02
3.0000000e+00	1.0000000e+00	5.9485596e-01	0.0000000e+00
4.0000000e+00	2.0000000e+00	7.3983711e-01	9.1992370e-02
5.0000000e+00	2.0000000e+00	7.3983711e-01	9.1992370e-02
6.0000000e+00	2.0000000e+00	7.2259275e-01	3.8290350e-01
7.0000000e+00	2.0000000e+00	8.4674417e-01	2.0752290e-01
8.0000000e+00	2.0000000e+00	8.5048217e-01	2.5530340e-01
9.0000000e+00	2.0000000e+00	8.5048217e-01	2.5530340e-01
1.0000000e+01	2.0000000e+00	1.8484144e-01	9.0885687e-01
1.1000000e+01	1.0000000e+00	9.4688867e-01	0.0000000e+00
1.2000000e+01	2.0000000e+00	9.4923771e-01	2.9539300e-02
1.3000000e+01	2.0000000e+00	-1.8939909e-02	9.5952692e-01
1.4000000e+01	2.0000000e+00	8.3618533e-01	4.7281130e-01
1.5000000e+01	2.0000000e+00	9.8927829e-01	1.0542525e-02
1.6000000e+01	2.0000000e+00	3.5073811e-01	9.2872790e-01
1.7000000e+01	2.0000000e+00	3.9195067e-01	9.1304180e-01
1.8000000e+01	2.0000000e+00	3.4395633e-01	9.3255771e-01

$$B_{c9} = \begin{bmatrix}
1.6929925e+00 & -2.0103410e+00 & 5.1178601e+00 & 1.8721082e+00 & 0.0000000e+00 \\
-1.4306601e+00 & 1.7241005e+00 & -4.3819037e+00 & -1.5737262e+00 & 0.0000000e+00 \\
1.5228125e+00 & -1.8122857e+00 & 4.6186803e+00 & 1.6816538e+00 & 0.0000000e+00 \\
3.2558851e+00 & 4.2949627e+00 & -1.5312233e+00 & -2.5444479e-01 & 0.0000000e+00 \\
-6.5938761e-01 & -1.2435841e+00 & 1.6067616e-01 & -3.3429720e-02 & 0.0000000e+00 \\
-8.4178501e-02 & 3.2605372e-01 & -6.7521800e-01 & -2.9275919e-01 & 0.0000000e+00 \\
-2.1059136e+00 & -4.3389398e+00 & 7.2453062e-01 & -6.6724330e-03 & 0.0000000e+00 \\
-1.8674027e+00 & -1.8262086e+00 & 2.3695455e+00 & 8.9832898e-01 & 0.0000000e+00 \\
-3.8143185e-01 & 6.8622161e-02 & -1.7308814e-01 & -3.8448218e-02 & 0.0000000e+00 \\
-9.1698940e-01 & -2.2933171e-01 & -8.3640838e-01 & -4.8571862e-01 & 0.0000000e+00 \\
7.2161990e-01 & -4.7232950e-01 & -6.3477770e-02 & -7.5475487e-02 & 0.0000000e+00 \\
-1.6008374e+00 & -1.6817193e+00 & 2.5709641e-01 & 1.1746963e-02 & 0.0000000e+00 \\
6.0472042e-01 & -6.4151590e-02 & 6.3625128e-01 & 2.9907798e-01 & 0.0000000e+00 \\
3.2426651e-01 & 3.1732640e-01 & -1.5857499e-01 & -1.7825532e-02 & 0.0000000e+00 \\
-6.1423325e-01 & -3.7494903e-01 & -8.2448787e-02 & -6.6580595e-02 & 0.0000000e+00 \\
9.3971680e-02 & 1.9826487e-01 & 4.6584403e-02 & 2.7597750e-02 & 0.0000000e+00 \\
1.0151369e-03 & -7.2209392e-03 & 4.5263330e-02 & 3.8275800e-03 & 0.0000000e+00 \\
-1.9182462e-02 & 1.3134404e-02 & 4.7779286e-03 & -3.6470285e-02 & 0.0000000e+00 \\
8.1359307e-01 & 8.2563810e-01 & -4.7934137e-03 & 8.5677213e-02 & 0.0000000e+00 \\
1.9861650e-01 & 7.4630388e-02 & 2.1634108e-01 & 1.0149117e-01 & 0.0000000e+00 \\
1.3696630e+00 & 9.8356352e-01 & 3.4955041e-01 & 2.6125651e-01 & 0.0000000e+00 \\
3.0859232e-03 & -4.3036453e-03 & -1.5291797e-02 & -4.8800172e-04 & 0.0000000e+00 \\
-8.5751458e-03 & 1.1573107e-02 & -8.6872432e-03 & -1.3142055e-03 & 0.0000000e+00 \\
7.1495246e-03 & 6.3036582e-03 & -3.2458647e-03 & 3.2784725e-03 & 0.0000000e+00 \\
-3.2761380e-02 & -2.3846850e-02 & -1.7365637e-02 & -9.1143221e-03 & 0.0000000e+00 \\
-3.2500788e+01 & -1.5582181e+01 & -1.4862555e+01 & -8.1783550e+00 & 0.0000000e+00 \\
8.1864104e+00 & 4.0813536e+00 & 3.6784143e+00 & 2.0426318e+00 & 0.0000000e+00 \\
-1.6166330e-03 & 6.8210711e-04 & -1.2873980e-03 & -1.3865530e-03 & 0.0000000e+00 \\
-3.1116682e-04 & 2.0345945e-05 & -2.7581244e-04 & -6.0194953e-04 & 0.0000000e+00 \\
-1.1474412e-03 & 7.2881722e-04 & -1.4152296e-03 & -1.0133458e-03 & 0.0000000e+00 \\
7.4805302e-04 & -9.1434180e-04 & 1.4826116e-03 & 1.3658231e-03 & 0.0000000e+00 \\
-1.3042720e-03 & -4.5175594e-04 & -1.4129768e-03 & -1.8912562e-03 & 0.0000000e+00 \\
3.7599438e-03 & -3.1484094e-03 & 3.8681799e-03 & 4.4521421e-03 & 0.0000000e+00
\end{bmatrix}$$

$$C_{c9}^{\mathrm{T}} = \begin{bmatrix}
-3.9819691e-04 & 7.6538360e-04 & 0.0000000e+00 \\
-1.3305939e-04 & 2.5232495e-04 & 0.0000000e+00 \\
7.1141230e-04 & -1.3707407e-03 & 0.0000000e+00 \\
-6.1211103e-02 & 9.9652722e-02 & 0.0000000e+00 \\
-2.1564002e-01 & 8.6661862e-02 & 0.0000000e+00 \\
-1.3862033e-01 & 1.1890356e-01 & 0.0000000e+00 \\
1.0146534e-03 & 4.4754772e-02 & 0.0000000e+00 \\
-1.0861539e-01 & 2.7122542e-01 & 0.0000000e+00 \\
2.1053627e-02 & -5.0777343e-02 & 0.0000000e+00 \\
6.4661322e-02 & -1.3429982e-01 & 0.0000000e+00 \\
-5.1204792e-02 & 4.0510279e-01 & 0.0000000e+00 \\
1.2549187e-01 & -2.0558499e-01 & 0.0000000e+00 \\
1.2904372e-01 & -4.0787590e-01 & 0.0000000e+00 \\
-4.0723158e-03 & 1.8724286e-01 & 0.0000000e+00 \\
1.8605297e-01 & 1.1964064e-01 & 0.0000000e+00 \\
3.9190346e-01 & 1.2479422e-01 & 0.0000000e+00 \\
-1.8392476e-04 & 2.4048609e-04 & 0.0000000e+00 \\
-1.3626570e-03 & 2.4513056e-03 & 0.0000000e+00 \\
1.4655299e-01 & 4.8161877e-01 & 0.0000000e+00 \\
-3.0648064e-01 & -8.7035634e-02 & 0.0000000e+00 \\
-1.7219636e-01 & -3.4724411e-01 & 0.0000000e+00 \\
1.3263930e-04 & -2.8459485e-04 & 0.0000000e+00 \\
2.7019679e-04 & -4.9746779e-04 & 0.0000000e+00 \\
2.8411443e-02 & -5.6222505e-03 & 0.0000000e+00 \\
-1.3150730e-01 & -6.5623631e-02 & 0.0000000e+00 \\
-7.1696825e-02 & 1.0791667e-01 & 0.0000000e+00 \\
-2.4518656e-01 & 4.1955854e-01 & 0.0000000e+00 \\
-9.1739310e-04 & 1.8977501e-03 & 0.0000000e+00 \\
-2.1733308e-03 & 3.8465769e-03 & 0.0000000e+00 \\
-3.1489142e-03 & 5.4767621e-03 & 0.0000000e+00 \\
-9.3769586e-04 & 1.2032575e-03 & 0.0000000e+00 \\
-9.8166771e-04 & 1.7904166e-03 & 0.0000000e+00 \\
-2.4374991e-03 & 4.6524478e-03 & 0.0000000e+00
\end{bmatrix}$$

$$D_{c9} = \begin{bmatrix}
0.0000000e+00 & 0.0000000e+00 & 0.0000000e+00 & 0.0000000e+00 & 0.0000000e+00 \\
0.0000000e+00 & 0.0000000e+00 & 0.0000000e+00 & 0.0000000e+00 & 0.0000000e+00 \\
0.0000000e+00 & 0.0000000e+00 & 0.0000000e+00 & 0.0000000e+00 & 1.0000000e+01
\end{bmatrix}$$

NASA
National Aeronautics and Space Administration

Report Documentation Page

1. Report No.
NASA CR-4377

2. Government Accession No.

3. Recipient's Catalog No.

4. Title and Subtitle
High Performance, Accelerometer-Based Control of the Mini-MAST Structure at Langley Research Center

5. Report Date
May 1991

6. Performing Organization Code

7. Author(s)
Emmanuel G. Collins, Jr., James A. King, Douglas J. Phillips,and
David C. Hyland

8. Performing Organization Report No.

9. Performing Organization Name and Address
Harris Corporation
Government Aerospace Systems Divison
Mail Stop 22/4847
Melbourne, FL 32902

10. Work Unit No.
585-01-91-01

11. Contract or Grant No.
NAS1-18872

12. Sponsoring Agency Name and Address
National Aeronautics and Space Administration
Langley Research Center
Hampton, VA 23665-5225

13. Type of Report and Period Covered
Contractor Report - Final

14. Sponsoring Agency Code

15. Supplementary Notes

Technical Monitor - Rudeen Smith-Taylor, Langley Research Center

16. Abstract

Many large space system concepts will require active vibration control to satisfy critical performance requirements such as line-of-sight pointing accuracy and constraints on rms surface roughness. In order for these concepts to become operational, it is imperative that the benefits of active vibration control be practically demonstrated in ground-based experiments. This report describes the second experiment conducted by Harris as part of the NASA Controls-Structure Interaction (CSI) Guest Investigator Program. The results of this experiment demonstrate the successful application of the Maximum Entorpy/Optimal Projection control design methodology to active vibration control for a flexible structure. The testbed is the Mini-Mast structure at NASA Langley Research Center and has features dynamically traceable to future space systems. To maximize traceability to real flight systems the controllers were designed and implemented using sensors (four accelerometers and one rate gyro) that are actually mounted to the structure. Ground-mounted displacement sensors that could greatly ease the control design task were available but were used only for performance evaluation. The use of the accelerometers increased the potential of destabilizing the system due to spillover effects and motivated the use of a precompensation strategy to achieve sufficient compensator roll-off.

17. Key Words (Suggested by Author(s))
Controls-Structures Interaction
Flexible Structures
Active Control
Robustness
Ground-based Experiment

18. Distribution Statement
unclassified - unlimited
subject category - 18

19. Security Classif. (of this report)	20. Security Classif. (of this page)	21. No. of pages	22. Price
unclassified	unclassified	106	A06

For sale by the National Technical Information Service, Springfield, VA 22161-2171

NASA-Langley, 1991

C-2